Quasi-Static Tensile and Fatigue Behavior of Extrusion Additive Manufactured ULTEM 9085

Khang D. Pham

Thesis submitted to the faculty of the Virginia Polytechnic Institute and State University in partial fulfillment of the requirements for the degree of

Master of Science

In

Mechanical Engineering

Walter F. O'Brien

Scott W. Case

Christopher B. Williams

December 13, 2017

Blacksburg, Virginia

Keywords: Additive Manufacturing, Fused Deposition Modeling, 3D Printing, ULTEM 9085

Quasi-Static Tensile and Fatigue Behavior of Extrusion Additive Manufactured ULTEM 9085

Khang D. Pham

ABSTRACT

Extrusion additive manufacturing technologies may be utilized to fabricate complex geometry devices. However, the success of these additive manufactured devices depends upon their ability to withstand the static and dynamic mechanical loads experienced in service. In this study, quasi-static tensile and cyclic fatigue tests were performed on ULTEM 9085 samples fabricated by fused deposition modeling (FDM). First, tensile tests were conducted following ASTM D638 on three different build orientations with default build parameters to determine the mechanical strength of FDM ULTEM 9085 with those supplied by the vendor. Next, different build parameters (e.g. contour thickness, number of contours, contour depth, raster thickness, and raster angle) were varied to study the effects of those parameters on mechanical strength.

Fatigue properties were investigated utilizing the procedure outlined in ASTM D7791. S-N curves were generated using data collected at stress levels of 80%, 60%, 30% and 20% of the ultimate tensile stress with an R-ratio of 0.1 for the build orientation XZY. The contour thickness and raster thickness were increased to 0.030 in. to determine the effect of those two build parameters on tension-tension fatigue life. Next, the modified Goodman approach was used to estimate the fully reversed (R=-1) fatigue life. The initial data suggested that the modified Goodman approach was very conservative. Therefore, four different stress levels of 25%, 20%, 15% and 10% of ultimate tensile stress were used to characterize the fully reversed fatigue properties. Because of the extreme conservatism of the modified Goodman model for this material, a simple phenomenological model was developed to estimate the fatigue life of ULTEM 9085 subjected to fatigue at different R-ratios.

Quasi-Static Tensile and Fatigue Behavior of Extrusion Additive Manufactured ULTEM 9085

Khang D. Pham

GENERAL AUDIENCE ABSTRACT

Additive manufacturing (AM) is a revolutionary technology that is dramatically expanding the current manufacturing capabilities. The additive process allows the designers to create virtually any geometry by constructing the parts in layers. The layer-to-layer build technique eliminates many of the limitations imposed by traditional manufacturing methods. For example, machining is a common manufacturing technique that is used to create highly complex parts by removing material from a billet. The process of removing material to create a part is called subtractive manufacturing. Subtractive manufacturing requires sufficient clearance for tool access, in addition to complicated mounting fixtures to secure the part. These constraints often force engineers to design less optimized geometries to account for the manufacturing limitations. However, additive manufacturing allows the user greater design freedoms without a significant increase in resources. This innovative construction technique will push the boundaries of cutting-edge designs by removing many restrictions associated with traditional manufacturing technologies.

Additive manufacturing is a relatively recent technology that evolved from rapid prototyping techniques that were developed in the 1960s. Rapid prototyping is used to create rapid iterations of physical models. However, additive manufacturing aims at creating functional end-use products. The layer-to-layer build process still poses many research challenges before it will be accepted as a reliable manufacturing technique. One of the current limitations with AM technologies is the availability of material properties associated with AM materials. The layer-to-layer build process and the toolpath creates different material properties that are dependent on the orientation of the applied load. Thus, further research is recommended to provide designers with a greater understanding of the mechanical characteristics of additive manufactured materials such as ULTEM 9085.

This objective of this research is to characterize the static strength and fatigue characteristics of ULTEM 9085. The first part of the thesis focused on investigating the effects of the following build parameters on the strength of the component: build orientation, contour thickness, number of contours, contour depth, raster thickness, and raster angle. The second portion of this investigation determined the effects of fluctuating loads on the fatigue life of ULTEM 9085. Overall, the results of this investigation can be used to design more effective components using extrusion additive manufacturing technologies.

Acknowledgements

I would like to acknowledge Dr. Scott Case, Dr. Walter O'Brien, and Dr. Christopher Williams for mentoring me throughout my graduate curriculum at Virginia Tech. Their leadership and passion inspired me to continually advance my skills as a researcher and an engineer. I would like to give special thanks to Dr. Case for promoting my ability to ask effective questions to drive solutions for my project. I would like to thank Dr. O'Brien for sharing his vision and providing me with the opportunity to work on exciting research. Lastly, I would like to thank Dr. Williams for opening up his lab and connecting me with his graduate students. They have played a monumental role in the success of my research project.

I would like to thank the United States Air Force Laboratory for providing me with the guidance and support through my thesis work. The bi-weekly meetings had helped me better understand the intricacies of the research environment outside of academia.

I also want to acknowledge the Center for the Enhancement of Engineering Education for supporting me the past seven years at Virginia Tech. I would like to thank Dr. Bevlee Watford and Susan Arnold-Christian for the opportunity to mentor students within the College of Engineering. My teaching experiences were one of the most rewarding experiences at Virginia Tech and it had greatly increased my competency as an engineer.

Lastly, thank you to all of the friends, peers, and mentors that I have met at Virginia Tech. They had made my academic journey a meaningful experience.

Table of Contents

List of Figures

List of Tables

Chapter 1 Introduction

Additive manufacturing (AM) is a revolutionary technology that is dramatically expanding the current manufacturing capabilities. The additive process allows the designers to create virtually any geometry by constructing the parts in layers. The layer-to-layer build technique eliminates many of the limitations imposed by traditional manufacturing methods. For example, machining is a common manufacturing technique that is used to create highly complex parts by removing material from a billet. The process of removing material to create a part is called subtractive manufacturing. Subtractive manufacturing requires sufficient clearance for tool access, in addition to complicated mounting fixtures to secure the part. These constraints often force engineers to design less optimized geometries to account for the manufacturing limitations. However, additive manufacturing allows the user greater design freedoms without a significant increase in resources. This innovative construction technique will push the boundaries of cutting-edge designs by removing many restrictions associated with traditional manufacturing technologies.

Additive manufacturing is a relatively recent technology that evolved from rapid prototyping techniques that were developed in the 1960s. Rapid prototyping is used to create rapid iterations of physical models. However, additive manufacturing aims at creating functional end-use products. The layer-to-layer build process still poses many research challenges before it will be accepted as a reliable manufacturing technique. One of the current limitations with AM technologies is the availability of material properties associated with AM materials. The layer-to-layer build process and the toolpath create anisotropic properties.[1] Anisotropic materials exhibit varying mechanical properties that are dependent on the orientation of the applied load. Thus,

further research is recommended to provide designers with a greater understanding of the mechanical characteristics of additive manufactured materials such as ULTEM 9085.

Additive manufacturing fuses material together in multiple layers to create a geometry. The additive method allows the designers to create extremely complicated parts by eliminating common limitations associated with subtractive manufacturing such as: toolpath interference, complex mounting solutions, and a large diverse toolset. Currently, there are seven different additive manufacturing technologies on the market. These technologies range from using high-powered lasers to sinter metal powders together to utilizing ultraviolet light to cure polymeric resins. Gao et al. discuss in greater detail the current state of each of the seven additive manufacturing technologies.[2] This investigation will focus on extrusion-based additive manufacturing technologies.

There are many steps involve in creating a component using additive manufacturing. The process begins by converting an idea to a solid model utilizing a CAD package. The CAD software converts the file format into an STL file. The STL file uses polygonal meshes to describe the surface geometry of the component. Next, the STL file is imported into a slicing software that discretizes the layers and generates the toolpath instructions for the AM machine to build the physical part. The AM printer constructs each layer until the product is complete. Depending on the application, the part is ready for use after the last layer is constructed or further post-processing is necessary. Figure 1 below shows the additive manufacturing process.

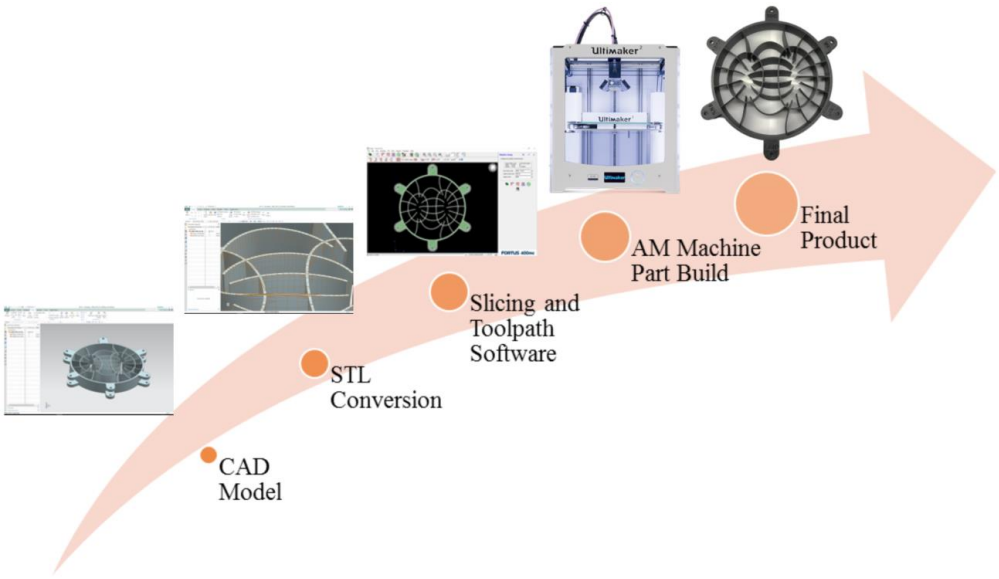

Figure 1. Additive Manufacturing Flow Process. The 6-in Offset Swirl StreamVane was used in the graphic above. The model was generated in CAD and converted to an STL file. Next, the slicing software sliced the part into layers and generated the commands for the toolpath. The AM machine constructed the geometry by extrusion.

The slicing software is capable of modifying many different build parameters within a single layer of the additive manufactured part. Preliminary research demonstrated that the build parameters could affect the mechanical properties of the component. Figure 2 below shows the different build parameters that the user can vary to optimize the mechanical properties of the component. The definitions of the build parameters are provided after the figure.

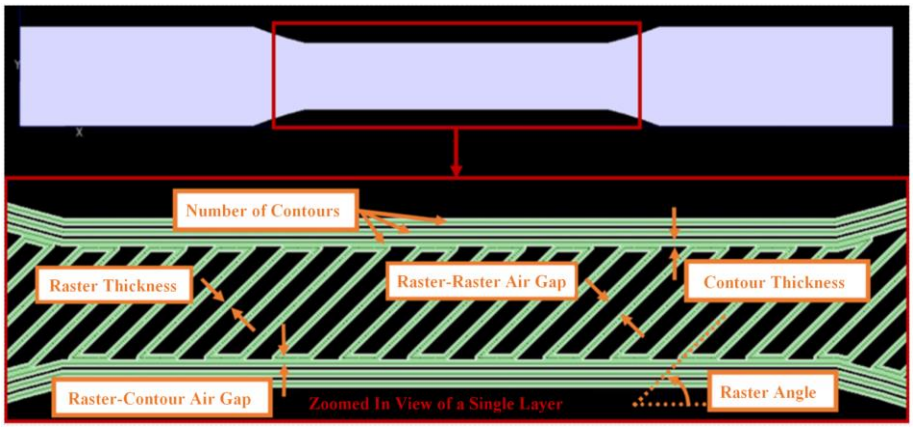

Figure 2. Components of a Single Extrusion Additive Manufactured Layer. The image above was generated using Stratasys Insight Revision Software. Each of the parameters shown can be manipulated by Insight Revision.

1. **Contour Thickness** – the width of the bead of material deposited on the outermost shell of the geometry
2. **Raster Thickness** – the width of the bead of material deposited to fill the interior of the geometry
3. **Raster Angle** – the angle from the x-axis of the machine to the direction of the raster fill. Typically, the raster angle rotates by $\pm 90^{o}$ between each layer
4. **Number of Contours** – the number of outermost shells deposited before filling in the interior of the part (raster fill)
5. **Raster to Raster Air Gap** – the distance between each bead of raster fill
6. **Raster to Contour Air Gap** – the distance between the raster fill and the innermost contour

The extrusion additive manufacturing process is further defined in Figure 3. Material extrusion machines construct a part by extruding a semisolid material through a nozzle. The nozzle deposit material in a specified toolpath along the XY-plane to create a single layer of the cross-sectional area of the part. After a layer is completed, the build platform moves along the z-axis direction to construct the next layer. The layers fuse together from the residual heat of the material bead, and the force of the extrusion. Additionally, a high performance extrusion machine will have a heated build chamber. The heated build chamber operates slightly above the glass transition temperature of the material. (The glass transition temperature for thermoplastics is the temperature at which the polymer transitions from a rigid material to a semi-solid state.) The heated build chamber can greatly enhance the layer-to-layer adhesion to improve product quality.

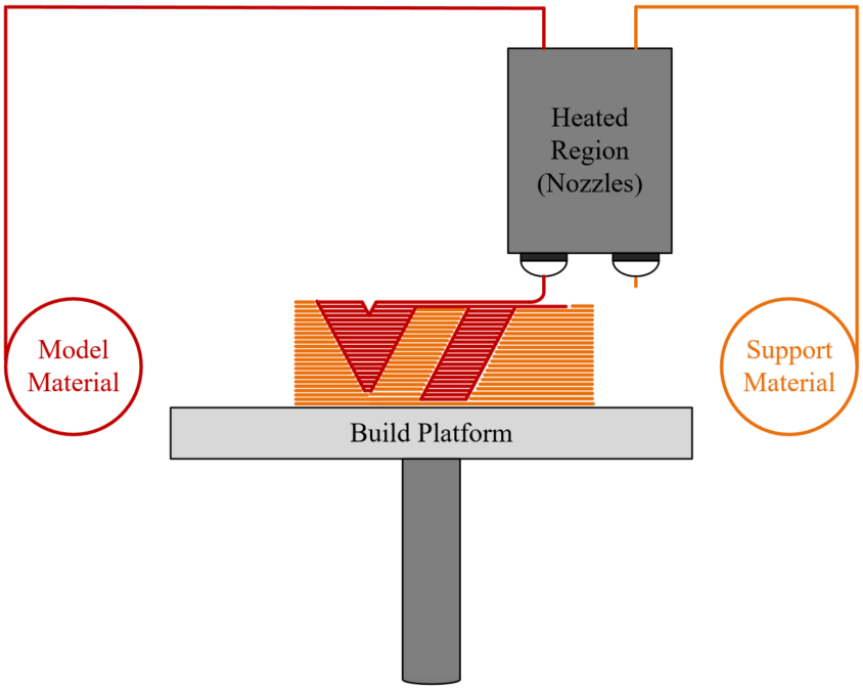

Figure 3. Extrusion Additive Manufacturing Schematic. This schematic is the front view of extrusion-based AM machine. The yellow build platform represents the XY-plane where the components are manufactured. The green support material is used to provide structural support if the printed geometry has a large overhang. The support material can be removed physically or chemically.

The manufacturing parameters play a significant role in the performance of the resulting part. For example, Hossain et al. performed a series of experiments to minimize the voids in extrusion additive manufactured parts through varying build parameters.[3] The raster angles were varied from 0º/90º, 30º/-60º, and 45º/45º. In addition, for each raster angle, the contour thickness, raster thickness, and raster-to-raster air gap were altered. The build parameters were adjusted to eliminate the voids based on observations for the simulated model in the slicing software (Insight Revision) and a physical inspection of the extruded part. The authors were able to demonstrate that the ultimate tensile strength can be optimized by 19% by reducing the voids.

1.1 Literature Review

Ahn et al. investigated the effect of different build parameters on the strength of the parts produced by fused deposition modeling (FDM). [1] The air gaps, raster orientation, bead width,

model temperature and filament colors were varied. The data suggested that only the air gap and the raster orientation had a significant effect on tensile strength of ABS. The tensile strengths for the various build parameters were compared to an injected molded part which was expected to have isotropic material properties. The FDM parts exhibited a tensile strength of 35%-28% less than the tensile strength of the injection molded part.

Bagsik et al. conducted tension and compression tests on ULTEM 9085 FDM parts with 3 different build orientations.[4] The X-direction, Y-direction, and Z-direction build orientation exhibited a mechanical strength of 8900 psi, 6620 psi, and 5900 psi respectively. Additionally, compression tests were conducted on FDM ULTEM 9085 with build directions of XYZ and ZXY. The XYZ-direction exhibited a compressive strength of 12000 psi. The ZXY-direction exhibited a compressive strength of 14000 psi. The different build directions had a significant impact on the mechanical properties of additive manufactured ULTEM 9085.

Bagsik et al. investigated the effects of different filament thicknesses, raster angles, and raster-to-raster air gap, and the perimeter to raster air gap on the mechanical properties of extruded ULTEM 9085 components.[5] The geometries built with a negative air gap demonstrated a higher mechanical strength. Similarly, the geometries with a thicker filament exhibited higher ultimate tensile strengths. The authors provided a mechanical properties map to correlate the relationship between the different build parameters and the ultimate tensile strength.

Lee et al. investigated the fatigue characteristics of ABS (P400) and ABSplus (P430).[6] A Stratasys Dimension was used to fabricate the coupons in accordance with UNI EN ISO 527-1 (1997). One sample was tested per stress levels of 80%, 60% and 40% of the ultimate tensile stress for ABS and ABSplus respectively. This goal of this investigation was to understand the

failure mechanism of ABS/ABSplus components manufactured by fused deposition modeling, and not to fully characterize the material properties of the two materials. The strain energies were compared between different stress levels and materials. The net strain energy is the sum of the area under the stress and strain curve during the loading and unloading cycles. The strain energy should be zero for a perfectly elastic material. This investigation concluded that the strain energy for the FDM ABS part ranged from 3.4% to 19.7% of the bulk ABS material, and the strain energy for ABSplus FDM part ranged from 1.8% to 7.4%. The reduction in strain energy implied that the material became less ductile as the material was processed by fused deposition modeling.

Spikowski et al. compared the mechanical performance of FDM ULTEM 9085 to the mechanical performance of injection molded ULTEM 9085.[7] The FDM test coupons were printed in orientation ZXY and orientation XYZ with varying raster air gaps, raster widths, and contour widths. The injection molded test coupons were fabricated with a single and a double gate setup. The single gate injection molded coupon exhibited a mechanical strength of 13000 psi. The FDM coupons manufactured using the standard build parameters only exhibited 63% of the ultimate tensile stress of the injection molded coupons. Next, fatigue tests were conducted to compare the fatigue life of injection molding to FDM for ULTEM 9085. They concluded that the single gate injection molded components demonstrate a significantly higher fatigue life than FDM parts due to the homogenous material. The quick failure in the FDM parts was attributed to the stress concentrations created by the voids and the deformation of internal filament strands.

Ning et al. investigated the mechanical properties of carbon fiber reinforced thermoplastic composites used in extrusion additive manufacturing. The carbon fiber reinforced thermoplastic filament was produced by combining ABS pellets and carbon fiber powders. Two different carbon fiber lengths of 100 μm and 150 μm were used. Various amounts of carbon were mixed

with the ABS pellets. The carbon fiber powders were added in terms of percent weight of the entire mixture (3% wt., 5% wt., 7.5% wt., 10% wt., and 15% wt.). The carbon fiber reinforced filament was used to manufactured ASTM D638-10 specimen for tensile testing. The ultimate tensile strength increased with respect to the increase in fiber content until 7.5% wt. The ultimate tensile stress significantly dropped when the filament had a 10% wt. and a 15% wt. fiber content. The maximum ultimate tensile strength of 42 MPa was observed with coupons manufactured with the 7.5% wt. fiber content. The carbon fiber reinforced filament may increase the mechanical strength by 20% when the optimal ratios of carbon fiber to ABS were used.

Fischner et al. characterized the fatigue behavior of FDM ULTEM 9085. Three different orientations with the default build parameters were manufactured using a Fortus 400MC. A selected number of samples were vapor smooth with chloroform gas for two hours. Vapor smoothing is the act of using chemical vapors to smooth rough edges of FDM plastics. Eliminating the stress concentrations can improve the mechanical properties of FDM parts. The two hours treatment reduced the surface roughness from 135 μm to 34 μm. The tensile strength for the X and Y build direction did not increase significantly with the chloroform treatment. However, the tensile strength for the Z build direction increased by 16% with the vapor smooth treatment. Next, both of the treated and non-treated population were subjected to tension-tension fatigue tests. Stress levels ranged from 10% - 90% of the ultimate tensile strength were used to conduct the fatigue tests. The S-N curves for the X and Y build direction were very similar. As the stress levels decreased, the S-N curves for those two build directions converged. The Z build direction S-N curve lied toward the left indicating that the fatigue life was not as high in comparison to the other two build direction. The chemical treatment did not improve the fatigue characteristics of the FDM ULTEM 9085 components.

1.2 Research Objective

The present research is motivated by the need to have more accurate static and dynamic strength estimates for ULTEM 9085 to support the design of new flow control devices called StreamVanes.[8] However, the material results reported are applicable to the manufacture and structural performance analysis of extrusion-formed additive manufacturing components made from ULTEM 9085. Thus, a secondary objective is to provide designers with a deeper understanding of the mechanical properties of ULTEM 9085 to push the boundaries of innovative product design.

This report is broken into five different sections to summarize the work that was performed to characterize the static and mechanical properties of ULTEM 9085. Section 1 consists of a preliminary literature review and an overview of the mechanics of extrusion-based additive manufacturing technologies. Section 2 is split into four major subsections to discuss the manufacturing process, the preconditioning process, and the experimental setup for the static tests and fatigue tests. The static tests investigated the effect of various build parameters on the ultimate tensile strength of ULTEM 9085. Multiple fatigue tests were initiated to explore the standard tension-tension fatigue characteristics, tension-compression fatigue characteristics, build parameter effects on fatigue life, and low stress fatigue properties. Section 3 presents the data and an in-depth analysis of the results of each experiment. Section 4 summarizes the key learnings from the investigations to develop a best practice for producing additive manufactured components. Lastly, Section 5 concludes the entire report with proposed future research topics to advance the capabilities of extrusion-based additive manufacturing technologies.

Chapter 2 Methodology and Experimental Setup

2.1 Manufacturing

The samples used in this investigation were manufactured using a Stratasys Fortus 400 MC. This machine is optimized for producing high quality ULTEM 9085 parts due to the temperature capability of the heated build chamber. The Fortus systems are capable of extruding ULTEM 9085 into a heated environment of 383^{o}F (195^{o}C), which is slightly above the ULTEM 9085 glass transition temperature of 366^{o}F (186^{o}C). The process of extruding plastic in a heated chamber maximizes the layer-to-layer adhesion and reduces the internal stresses on the final product. The Stratasys Fortus 400MC was chosen to manufacture test coupons for this investigation because it is can reliably produce high quality ULTEM parts. Additionally, a Fortus 900MC, a larger version of the Fortus 400MC, is currently utilized to manufacture the StreamVanes. (Figure 4 below compares the two different machines from Stratasys.) The software, control systems, and some components between the two machines are interchangeable. The major difference is that the build volume for the Fortus 400MC is 16 in. x 14 in. x 16 in. and the build volume for the Fortus 900MC is 36 in. x 24 in. x 36 in. The cost and iteration time between the tests were substantially reduced by utilizing the Fortus 400MC machine that is available at Virginia Tech rather than relying on an outside vendor.

Figure 4. Comparison between Fortus 400MC and Fortus 900MC. Both the Fortus 400MC and the Fortus 900MC are very similar except for the build volumes. The Fortus 400MC has a build envelope of 16 in. x 14 in. x 16 in. and the Fortus 900MC has a build envelope of 36 in. x 24 in. x 36 in. The image above was obtained from Metalworking World Magazine. [3, 9]

The geometry of the test coupons was determined using the specifications outlined in ASTM D638.[10] The ASTM D638 Type I geometry has been used in multiple works by others involving mechanical testing of additive manufactured thermoplastics.[1, 11, 12] Please see Figure 5 below for the dimensions of the test coupons used in this investigation.

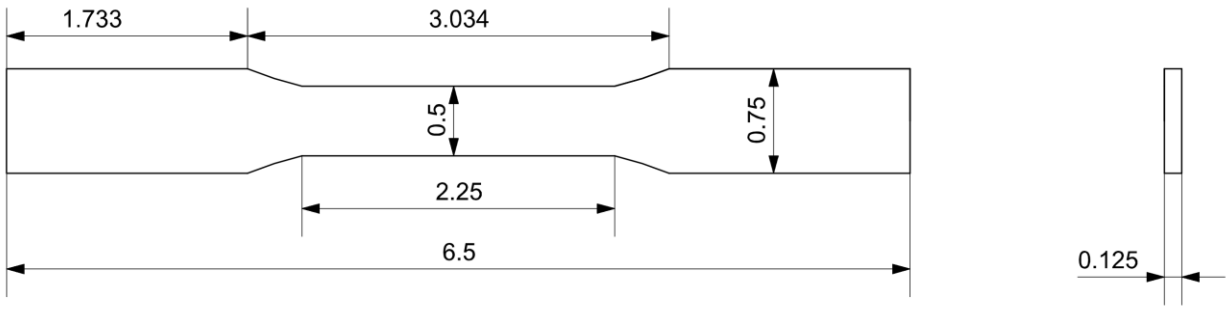

Figure 5. Fully dimensioned drawing of ASTM D638 Type I geometry. The test geometry was develop in accordance to the ASTM D638-14.

2.2 Pretesting Conditioning

The test coupons were labeled, weighed, and measured immediately after manufacturing to fulfill the requirements outlined in ASTM D638. Each test coupon was labeled with a test code and a number that corresponded to a particular sample in the sample population. The test code can be related back to the various build parameters shown in Table A-1 shown in Chapter 6Appendix A. A Mitutoyo Series 500 caliper with a resolution 0.0005 in. was used to measure the thickness and the width of the gage section of the specimen. An AWS-100 scale with a resolution of 0.01 g was used to record the mass of each of the sample. The two measurement tools can be seen in Figure 6. The measured data were used to determine the void density of extrusion additive manufactured test coupons. Please refer to Chapter 6Appendix B for the recorded data for the physical properties of the coupons.

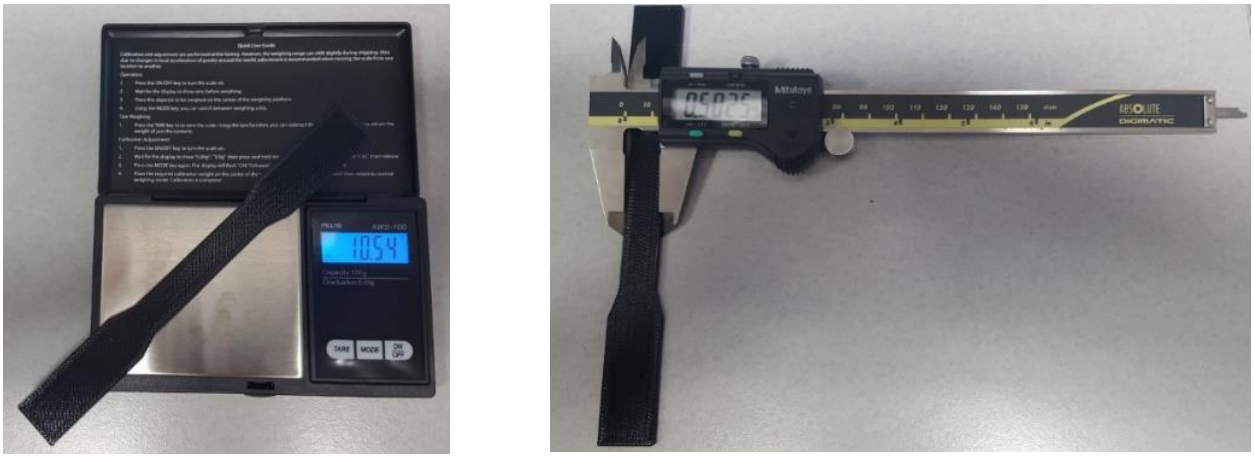

Figure 6. Tools for Mass and Dimensional Measurements. The mass of the coupon was determined using the AWS-100 on the left. The width and thickness were measured for each specimen using the Mitutoyo Series 500 caliper on the right.

Relative humidity and temperature can affect the mechanical properties of thermoplastics. [13] ASTM D618 specifies that the plastic samples must be preconditioned at 23ºC and 50% relative humidity 40 hours to standardize the atmospheric conditions that the materials are exposed to

before mechanical testing. The coupons were placed on a wired rack to allow air circulation on all surfaces. An Acurite digital and humidity monitor was used to record the ambient conditions during the pre-conditioning stage and the actual test. Please refer to Chapter 6Appendix C and Chapter 6Appendix D for the environmental data during the preconditioning and testing phase. Figure 7 below depicts the apparatuses used for preconditioning the test coupons.

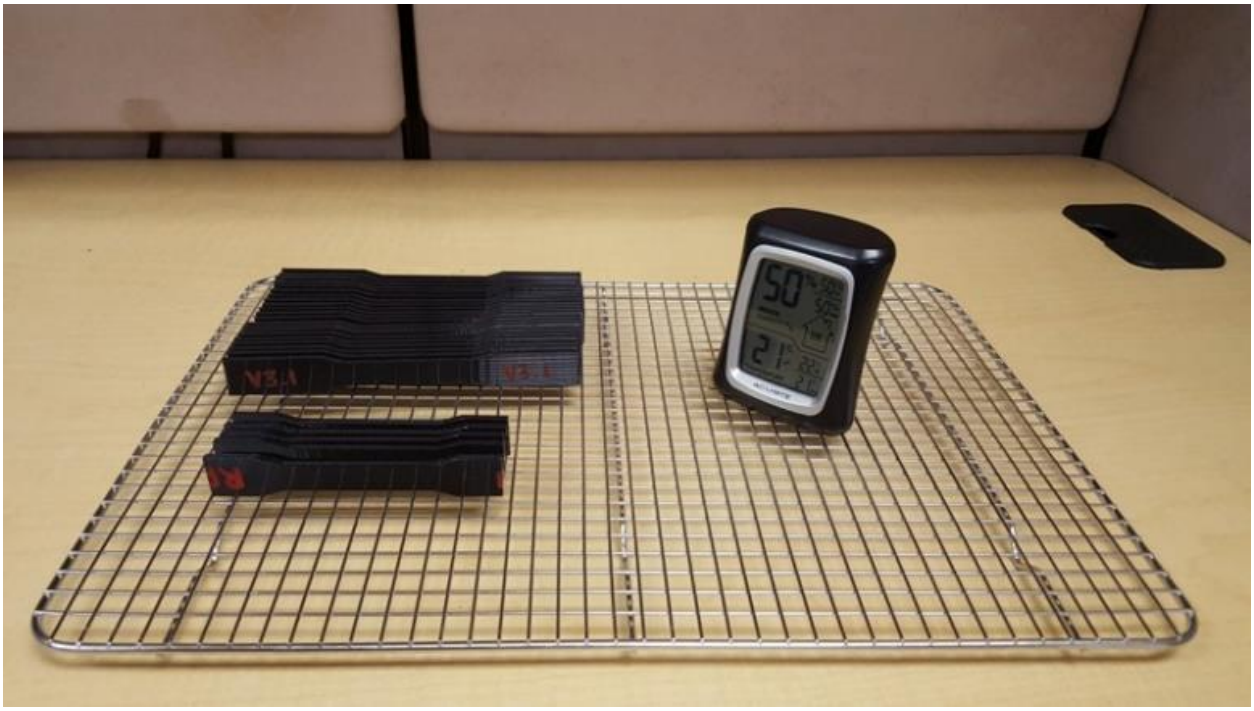

Figure 7. Preconditioning of ASTM D638 Geometry. The test coupons were spaced apart on the wired rack to allow full air circulation around the parts. The relative humidity and temperature were monitored by the Acurite Monitor.

2.3 Static Testing Methodology and Experimental Setup

The build parameters that were investigated in this report were contour thickness, number of contours, contour depth, raster angle, raster thickness, and build orientation. Only one build parameter was altered at a time with all other build parameters maintained at the default build settings. The raster thickness and the contour thickness were increased from 0.018 in. to 0.030 in.

by increments of 0.006 in. The relationship between contour thickness and the number contours was further investigated with the contour depth experiment. For this experiment, the contour depth was kept constant at 0.060 in. while the contour thickness and the number of contours were manipulated simultaneously. Lastly, the three different orientations were tested and compared to the ULTEM 9085 material specifications sheet provided by Stratasys. Table 1 below shows the test matrix for the static portion of this investigation.

Table 1. Static Material Properties Characterization Test Matrix

Static Experimental Build Parameters		**Default Build Parameters**	
Build Parameters	**Setting**	**Build Parameters**	**Setting**
Contour Thickness	0.018 in.	Contour Thickness	0.020 in.
	0.024 in.	Number of Contours	1 Contour
	0.030 in.	Raster Angle	45°/-45°
Number of Contours	1 Contour	Raster Thickness	0.0 in.
	2 Contours	Raster to Contour Air Gap	0.0 in.
	3 Contours	Raster to Raster Air Gap	0.0 in.
Contour Depth (0.060 in.)	2 Contour | Contour Thickness: 0.030 in.	Contour to Contour Air Gap	0.0 in.
	3 Contour | Contour Thickness: 0.020 in.		
Raster Angle	15°/-75°		
	30°/-60°		
Raster Thickness	0.018 in.		
	0.024 in.		
	0.030 in.		
Build Orientation	XYZ		
	XZY		
	ZXY		

2.3.1 Static Testing Experimental Setup

The static mechanical properties were characterized through a series of tension-tension tests following the procedure outlined in ASTM D638. The tensile tests were performed on an Instron 4468 material testing machine equipped with a 5 kN load cell. The strain of the gage section was measured by a MTS 634.12E-54 extensometer with a 1 in. gage length and a maximum strain of 0%-50%. The testing speed was set to 0.2 in./min. Five repetitions of the same test were performed on each build parameter to ensure repeatability within the data. Figure 8 below shows the experimental setup for the tensile tests.

Figure 8. Experimental Setup for Static Testing. A 5 kN Instron 4468 load frame was used to conduct the static tests for ULTEM 9085 coupons. A MTS 634.12E-54 extensometer was used to measure the strain of the gage section as shown in right picture.

2.3.2 Build Orientation ZXY Geometry Change

Only two out of the three different build orientations were successfully manufactured for testing. The tall aspect ratio of the Orientation ZXY caused delamination between the layers toward the top (larger z-axis dimension). A detailed analysis of the failure mechanism is provided in End Use Parts Manufacturing Best Practices. The geometry for the ZXY Orientation deviated from a

standard ASTM 638 Type I geometry to a shorten rectangular bar with the same gage section area. This new geometry followed the specifications outlined in ASTM 3039 Standard Test Method for Tensile Properties of Polymer Matrix Composite Materials.[14] The ASTM 3039 geometry has also been used to test additive manufactured materials because the layering of properties is conceptually very similar to layered composites. Figure 9 shows the fully dimensioned rectangular bar.

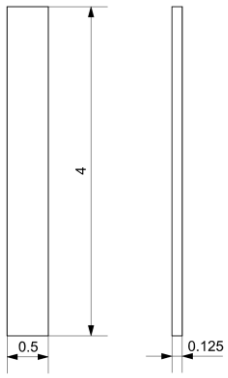

Figure 9. Fully Dimensioned Drawing ASTM 3039 Geometry. The fully dimensioned drawing of the rectangular bar manufactured for Orientation ZXY was designed in accordance with ASTM 3039.

2.4 Fatigue Testing Methodology & Experimental Setup

The fatigue characterization of additive manufactured ULTEM 9085 was broken down into three distinct experiments. The first portion involved performing standard tension-tension (R=0.1) uniaxial fatigue tests. The data from the tension-tension tests were used to generate the S-N curves for ULTEM 9085. These curves were compared to another dataset generated by Fischner & Schoppner.[12] Next, low stress fatigue tests with stress values of 250 psi were carried out to demonstrate that ULTEM 9085 is more than capable of handling low stress cyclic loads expected for StreamVane applications. The value of 250 psi was chosen at the request of the Air Force Research Laboratory (AFRL). Previous work by AFRL demonstrated that the maximum steady

stress on the StreamVane is 280 psi. However, the unsteady fluctuating stresses were in the ranges of 9.4 psi.[15]

2.4.1 Standard Tension-Tension Uniaxial Fatigue Test (R=0.1) Methodology

The S-N curves for additive manufactured ULTEM 9085 were generated using the procedures outlined in ASTM D7791-17.[16] Three samples were tested at four different stress levels that corresponded to the percentage of ultimate tensile stress. The fatigue testing machine was programmed to maintain an R-Ratio of R=0.1. The R-Ratio is the ratio of the minimum stress over the maximum stress as seen in Equation (12).

$$R = \frac{\sigma_{min}}{\sigma_{max}} \tag{1}$$

The coupons in this investigation were manufactured using the default build parameters in the XZY orientation. Please see Table 2 for the tension-tension fatigue test matrix.

Table 2. Tension-Tension Fatigue Test Matrix with Default Build Parameters

Tension-Tension Fatigue Test Matrix (R=0.1)			**Coupon Build Settings**	
Ultimate Tensile Strength [psi]	10100		**Build Parameters**	**Settings**
Test Frequency [Hz]	5		Contour Thickness	0.020 in.
Stress Level [% UTS]	**σ_{max} [psi]**	**σ_{min} [psi]**	Number of Contours	1 Contour
80	8080	808	Raster Angle	45°/-45°
60	6060	606	Raster Thickness	0.020 in.
30	3030	303	Raster to Contour Air Gap	0.0 in.
20	2020	202	Raster to Raster Air Gap	0.0 in.
			Contour to Contour Air Gap	0.0 in.
			Build Orientation	XZY

2.4.2 Build Parameters Variation Fatigue Test (R=0.1) Methodology

Fatigue tests were conducted with coupons manufactured with varying contour and raster thicknesses to determine the effects of the build parameters on fatigue life. The contour thickness and raster thickness were both increased to 0.030 in. The build orientation remained constant at the XZY Orientation. Three specimens were tested at 5 Hz and four different stress levels of 80% UTS, 60% UTS, 30% UTS, and 20% UTS. The tests utilized the standard tension-tension procedure mentioned above where R=0.1. Please refer to Table 3 below for the test matrix.

Table 3. Tension-Tension Fatigue Test Matrix with Various Build Parameters

Build Parameters Variation Fatigue Test Matrix (R=0.1)				**Default Build Parameters**	
Ultimate Tensile Strength [psi]		10100		**Build Parameters**	**Settings**
Test Frequency [Hz]		5		Number of Contours	1 Contour
Build Parameter	**Stress Level [% UTS]**	**σ_{max} [psi]**	**σ_{min} [psi]**	Raster Angle	45°/-45°
Contour Thickness: 0.030 in.	80	8080	808	Raster to Contour Air Gap	0.0 in.
	60	6060	606	Raster to Raster Air Gap	0.0 in.
	30	3030	303	Contour to Contour Air Gap	0.0 in.
	20	2020	202	Build Orientation	XZY
Raster Thickness: 0.030 in.	30	3030	303		
	20	2020	202		

2.4.3 Low Stress Fatigue Test (R=0.1)

Three coupons were tested at a stress level of 2.5% UTS. ASTM D7791 specifies that the fatigue test should be manually terminated end at 10^7 cycles, and fatigue run-out declared if the samples do not fail. However, due to the limited resource and the availability of the machine, fatigue run out was defined as 10^6 cycles. Table 4 shows the test matrix and coupon build parameters for the low stress fatigue test.

Table 4. Low Stress Fatigue Test Matrix with Default Build Parameters.

Fully Reversed Fatigue Test Matrix (R=-1)			**Coupon Build Settings**	
Ultimate Tensile Strength [psi]	10100		**Build Parameters**	**Settings**
Test Frequency [Hz]	5		Contour Thickness	0.020 in.
Stress Level [% UTS]	**σ_{max} [psi]**	**σ_{min} [psi]**	Number of Contours	1 Contour
2.5	250	25	Raster Angle	45°/-45°
			Raster Thickness	0.020 in.
			Raster to Contour Air Gap	0.0 in.
			Raster to Raster Air Gap	0.0 in.
			Contour to Contour Air Gap	0.0 in.
			Build Orientation	XZY

2.4.4 Experimental Setup for Tension-Tension Fatigue Test (R=0.1)

Two different load frames were used to conduct standard tension-tension fatigue tests because of the limitations of each machine. A MTS 810 with a 50 kN load cell was used to conduct fatigue tests at stress levels of 80% UTS and 60% UTS. However, the MTS 810 is not capable of maintaining a constant R-Ratio at the lower stress levels due to the compliance of the material, load cell resolution (50 N), and the size of the hydraulic servo-valve. Attempts were made to tune the MTS 810, but it was determined that further aggressive tuning might have created an unsafe situation due to the instability of the control system. An ElectroPuls E1000 was used to perform the fatigue tests at the 30% UTS, 20% UTS, and 10% UTS stress levels. The E1000 utilized a 2 kN load cell with a resolution of 2 N. This machine used electrically control actuators to enable it to precisely hit the targeted maximum and minimum stresses. Please see Figure 10 below for the experimental setup of the MTS 810 and the ElectroPul E1000.


Figure 10. Fatigue Testing Experimental Setup. The ElectroPuls E1000 on the left was used for stress levels less than 50% of ultimate tensile stress. The MTS 810 on the right was used for stress levels greater than 50% of the ultimate tensile stress.

2.4.5 Fully Reversed (R=-1) Fatigue Testing

The fully reverse testing was conducted to investigate the fatigue performance of ULTEM 9085 under tension-compression cyclic loading. The R-Ratio was programmed to R=-1.0, where the load frame cycles between a constant magnitude compressive load and tension load. The fully reversed fatigue testing was conducted on the ElectroPuls E1000. Three coupons with default build parameters in the XZY Orientation were tested at three different stress levels. Initially, the stress levels were determined using the modified Goodman relationship. The modified Goodman relationship attempts to collapse S-N data for different R-ratios to a single parametrization. The relationship can be observed in Equation (2), where σ_{ar} is the equivalent stress, σ_a is the alternating stress, $\sigma_m$is the mean stress, and σ_u is the ultimate tensile stress.

$$\sigma_{ar} = \frac{\sigma_a}{1 - \frac{\sigma_m}{\sigma_u}} \tag{2}$$

Equation (2) can be simplified in terms of ultimate tensile strength using the definition of mean stress and alternating stress. To demonstrate the application of this relationship, the next few paragraphs will derive the equivalent stresses using a R-Ratio of $R = 0.1$ and a fatigue test stress level of 30% UTS. The mean stress (σ_m) is the average between the maximum stress (σ_{max}) and the minimum stress (σ_{min}), as shown in Equation (3).

$$\sigma_m = \frac{(\sigma_{max} + \sigma_{min})}{2} \tag{3}$$

The alternating stress (σ_a) is defined as the difference between the maximum stress (σ_{max}) and minimum stress (σ_{min}) divided by two, as shown in Equation (4).

$$\sigma_a = \frac{(\sigma_{max} - \sigma_{min})}{2} \tag{4}$$

Assuming that an R-Ratio of $R = 0.1$ and a fatigue test stress level of 30% UTS, Equation (12) can be refined to Equation (5) below, where σ_{min} is the minimum stress and σ_u is the ultimate tensile stress. The maximum stress is 30% of the ultimate tensile stress.

$$0.1 = \frac{\sigma_{min}}{0.3\sigma_u} \tag{5}$$

Equation (5) can be rearranged to isolate the two unknown variables as shown in Equation (6).

$$\sigma_{min} = 0.03\sigma_u \tag{6}$$

σ_{min} in Equation (3) and Equation (4) is redefined using Equation (6) and σ_{max} is converted to terms of ultimate tensile stress to produce Equation (7) and Equation (8).

$$\sigma_m = \frac{0.3\sigma_u + 0.03\sigma_u}{2} \tag{7}$$

$$\sigma_a = \frac{0.3\sigma_u - 0.03\sigma_u}{2} \tag{8}$$

Equation (9) is the simplified version of Equation (2) with assumption that the R-Ratio is $R = 0.1$ and the fatigue test stress level is 30% UTS. The method shown in Equation (2)-Equation (9) is used to generate the equivalent stress between R=0.1 and R=-1.0 for additive manufactured ULTEM 9085 using the modified Goodman approach.

$$\sigma_{ar} = 0.16\sigma_u \tag{9}$$

However, preliminary data suggested that the modified Goodman approach is not valid for ULTEM 9085. Therefore, twelve coupons were subjected to cyclic loading at 5 Hz with varying stress levels of 25% UTS, 20% UTS, 15% UTS, and 10% UTS. The stress levels were kept below 30% UTS due to the limitation of the machine and buckling issues. Please see Table 5 below for the test matrix for the fully reversed test.

Table 5. Fully Reversed Fatigue Test Matrix

Fully Reversed Fatigue Test Matrix (R=-1)			**Coupon Build Settings**	
Ultimate Tensile Strength [psi]	10100		**Build Parameters**	**Settings**
Test Frequency [Hz]	5		Contour Thickness	0.020 in.
Stress Level [% UTS]	**σ_{max} [psi]**	**σ_{min} [psi]**	Number of Contours	1 Contour
25	2525	-2525	Raster Angle	45°/-45°
20	2020	-2020	Raster Thickness	0.020 in.
15	1515	-1515	Raster to Contour Air Gap	0.0 in.
10	1010	-1010	Raster to Raster Air Gap	0.0 in.
			Contour to Contour Air Gap	0.0 in.
			Build Orientation	XZY

The geometry of the test coupons was modified to eliminate buckling in the tension compression fatigue tests. The buckling forces for the samples were calculated using the Euler's Buckling relation shown in Equation (10), where$F_{Buckling}$ is the buckling force, E is the Young's Modulus, I is the moment of inertia, K is the end condition factor, and L is the unsupported length.

$$F_{Buckling} = \frac{\pi^2 EI}{(KL)^2} \tag{10}$$

The end condition factor was specified as $K = 0.5$ due to the assumptions of fixed rotational and fixed translational at the ends. Please refer to Figure 11 below for a graphical representation of a completely fixed-end beam.

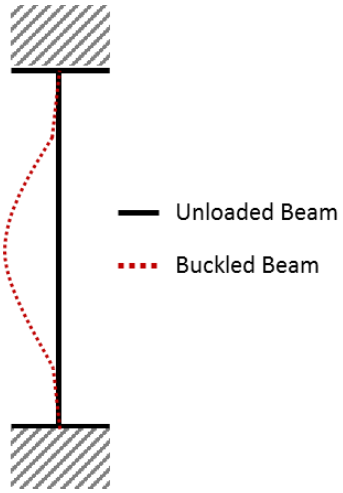

Figure 11. Fixed End Conditions Diagram. The solid line represents the beam not buckling, while the red dashed line is the bucked beam with both fixed rotational and fixed translational ends.

The moment of inertia was calculated using the following equation, where b is the base and h is the height of the cross sectional area.

$$I_x = \frac{bh^3}{12} \tag{11}$$

Equation (10) calculated the bucking force to be 33 lbf. The calculated buckling force assumed that the end conditions are completely fixed and a simple rectangular geometry exists for the entire coupon. The simple rectangular geometry is the worst case scenario where the cross-sectional area of the gage section is assumed for the entire length of the coupon. Experimentally, the buckling force was determined to be 43 lbf, which is significantly lower than the desired force 158 lbf. The 158 lbf equates to a stress level of 2525 psi (25% UTS). The buckling force was increased by shortening the gripping region and the gage section to decrease the unsupported length. The gripping region had to be reduced because the grips on the E1000 were not deep enough to fully engage the standard ASTM 638 Type I geometry. Please refer to Figure 12 below to see the shallow grip depths on the E1000.

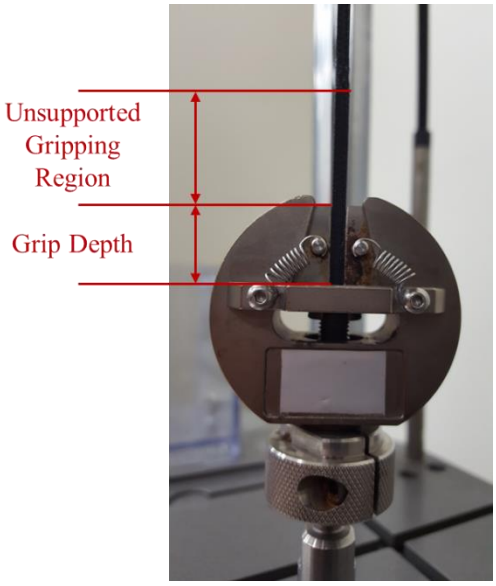

Figure 12. Shallow Grip Depth on E1000. The depth of the grips was not deep enough to fully engage the gripping region of the ASTM D638 Type I geometry. The excessive gripping region added the unsupported length which greatly reduced the buckling force.

The gripping region length from both ends and the gage section length were reduced by 0.875 in. and 1.25 in. respectively. The thickness, width, and radius of the shoulder of the coupon remained constant. The calculated buckling force for the new geometry is 315 lbf, which is twice the load of the desired bucking force. Figure 13 below shows the fully dimensioned drawing of the coupon used for fully reversed testing.

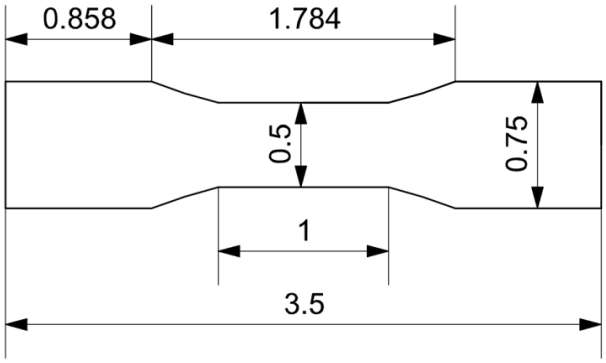

Figure 13. Fully Dimensioned Drawing Modified ASTM D638 Geometry. The fully dimensioned shortened coupon showed above deviated from ASTM standards. A verification test was conducted to ensure that the shortened coupon has similar material properties as the ASTM D638 Type I geometry.

The shortened coupons should not have buckled, but the shorten samples showed signs of buckling at 68 lbf of compressive force. This bucking occurred because the mounting shaft of top grip on the ElectroPuls lacked the necessary stiffness to handle the compressive loads. Figure 14 below shows the top grip translating under compressive load. The translational motion applied a lateral force to the coupons. This lateral force from the top grip caused the specimen to buckle.

Figure 14. Translating Grip on the E1000. The top grip's mounting shaft does not have enough stiffness to support the compressive load. The bending of the mounting shaft applied a lateral load to the specimen causing it to buckle.

Figure 15.Tools for Modifying E1000 Grip Mounting Rod. The M6X1.0 bolts were measured to approximately 22mm and cut using a hacksaw. A file and a die were used to removed debris from the threads to ensure smooth fastening.

Figure 16 shows the new configuration in relation to the old configuration. The new configuration and shorten coupon were verified by a standard tension-tension test at 30% UTS. The data correlated very well between the old and new setup correlated very well. Thus, the modified experimental setup and shorten coupons were used to conduct the fully reversed fatigue tests.

Figure 16. Reconfigured E1000 Fatigue Testing Machine. The picture to the left shows the E1000 in the original configuration with the load cell at the top. The picture to the right shows E1000 with the shortened coupon, shortened grip's mounting rod, and the load cell was moved to the bottom of the machine.

Chapter 3 Results & Discussion

This section will present the data collected from the static tests and the fatigue tests. Only one build parameter is tested at a time. All other build parameters were kept at the default settings specified in the experimental design section.

3.1 Static Testing Results

This subsection will present the ultimate tensile strength of the different build orientations, contour thicknesses, numbers of contours, contour depths, raster thicknesses, and raster angles. Asides from the build orientation tests, all specimens were manufactured in the XZY Orientation. The XZY Orientation was selected because that aspect ratio closely resembles the aspect ratio of a single vane on a StreamVane. Five coupons were tested per build parameter variation. The average ultimate tensile strengths are reported in the following subsections. Additionally, the mass analysis will discuss the effect of part density on the mechanical strength of additive manufactured ULTEM 9085.

3.1.1 Build Orientation

Three different build orientations were tested and compared to the data specification sheet for ULTEM 9085 provided by Stratasys. The naming convention for the build orientation followed the ASTM 52921 naming convention.[17] This standard labeled the orientation with descending magnitude of the dimensions correlating to the different axes of the component. Figure 17 and Figure 18 shows the two different build orientations that were successfully manufactured using the ASTM D638 Type I geometry. The geometry for the build orientation ZXY was modified to the rectangular geometry specified in ASTM 3039 as shown in Figure 19. The ZXY Orientation

was modified due to manufacturing defects that occurred with the tall aspect ratio. More information regarding the failure can be found in Chapter 4.

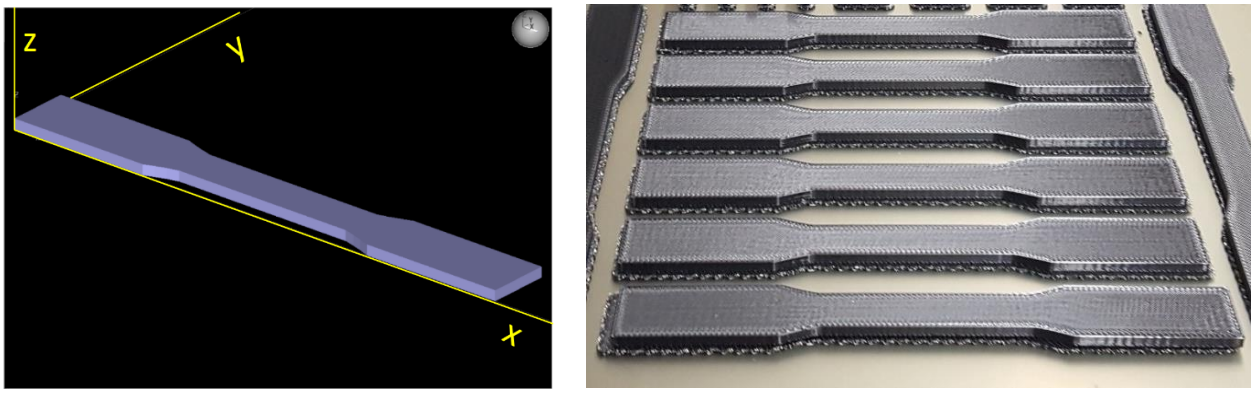

Figure 17. Build Orientation XYZ. The largest dimension of the coupon is parallel to the x-axis and followed by the y-axis and then the z-axis. The build direction is perpendicular to the yellow build sheet.

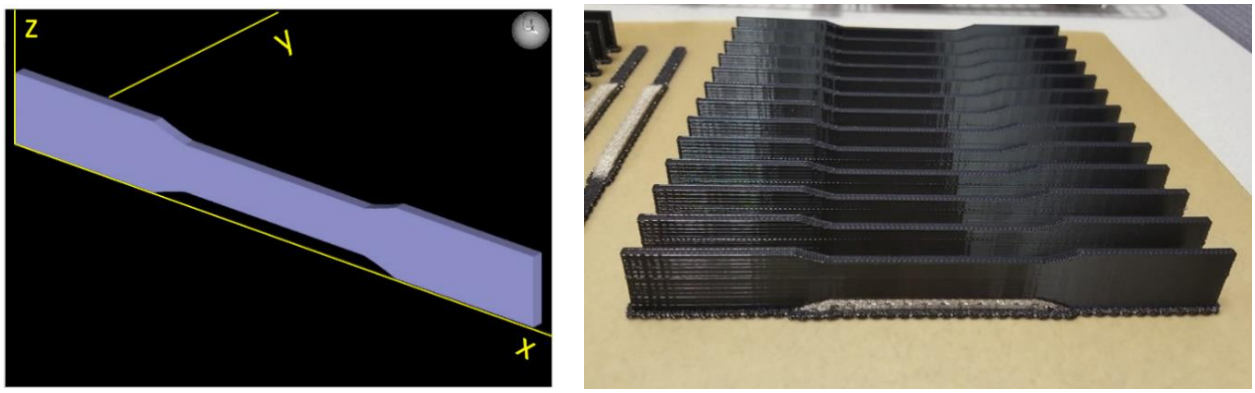

Figure 18. Build Orientation XZY. The largest dimension of the coupon is parallel to the x-axis and followed by the z-axis and then the y-axis. The build direction is perpendicular to the yellow build sheet.

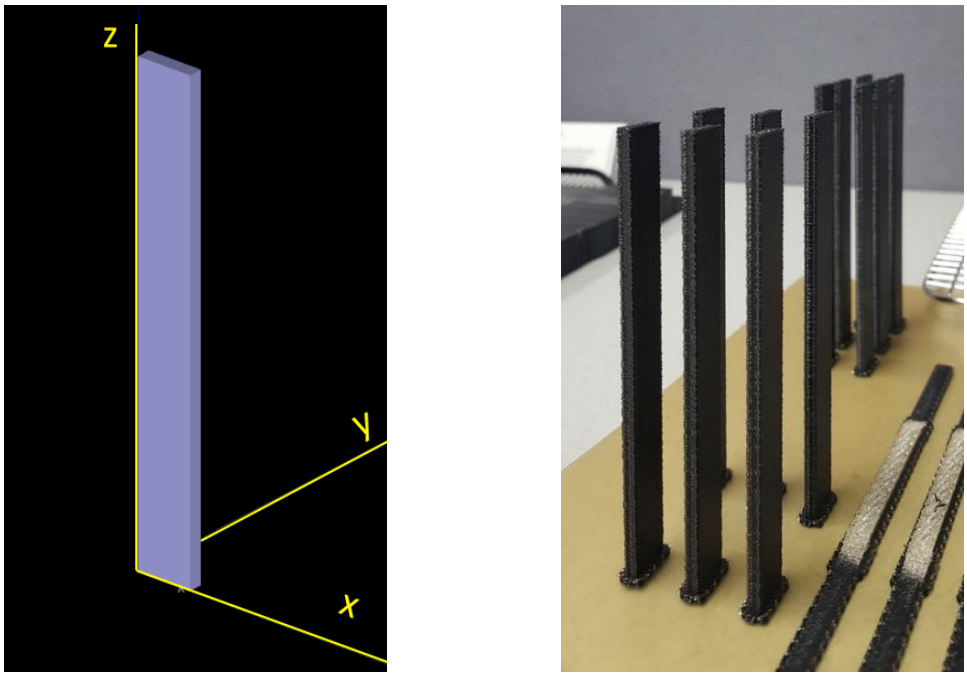

Figure 19. Build Orientation ZXY. The largest dimension of the coupon is parallel to the z-axis and followed by the x-axis and then the y-axis. The build direction is perpendicular to the yellow build sheet. The standard ASTM D638 Type I geometry was not successfully printed in the ZXY orientation.

The XZY orientation specimens have the greatest ultimate tensile strength of 10100 psi, followed by 8170 psi and 5460 psi for the XYZ orientation and ZXY orientation, respectively. The data for the XZY orientation matched very closely with the material specification sheet from Stratasys. The percent difference for the ZXY orientation between the OEM specifications and the data gathered was 11%. However, the variability in the ultimate tensile strength was within the range of the ultimate tensile strength listed by Stratasys. Figure 20 compared the UTS of the different orientations with the data provided by Stratasys.

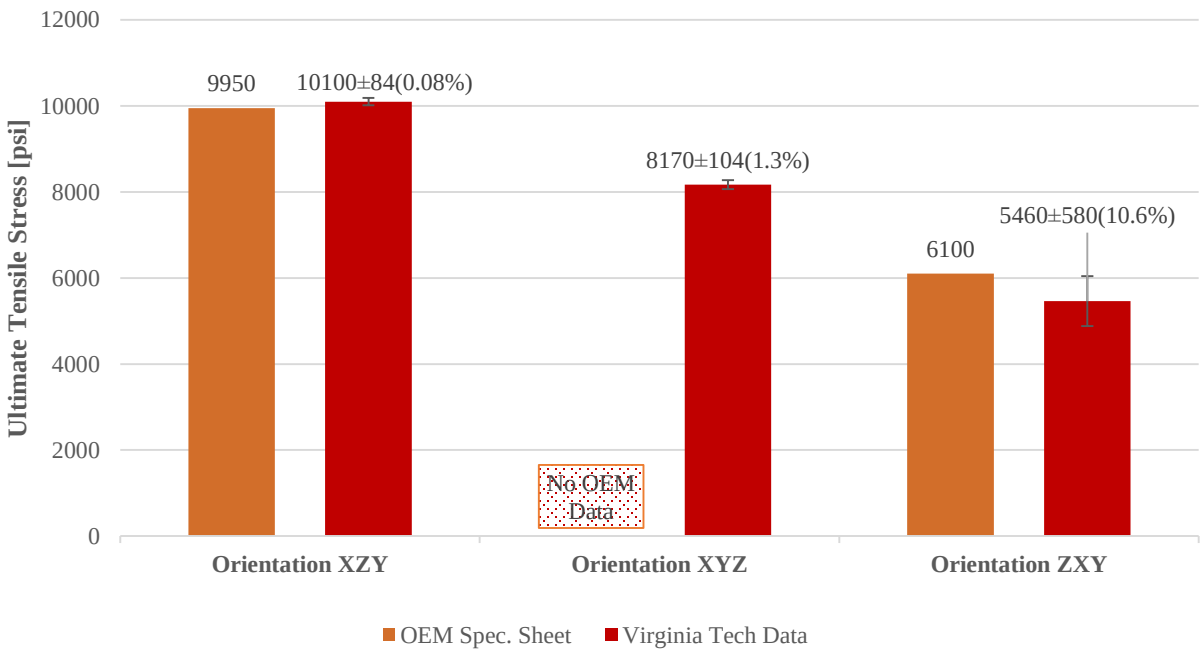

Figure 20. Verification of OEM ULTEM 9085 Material Specification Sheet Graph. The ULTEM 9085 data gathered from the three different orientations were compared to the data provided by Stratasys. The OEM material specification did not provide data for XYZ Orientation.

3.1.2 Contour Thickness

The contour thicknesses that were tested ranged from 0.018 in. – 0.030 in. in increments of 0.006 in. The contour thickness is defined as the thickness of a single bead of material on the outermost shell of the geometry, as shown in Figure 21. Figure 21 is a graphical representation with exaggerated build parameters used to demonstrate the definition of the contour thickness. Figure 22 - Figure 24 shows the test coupons with contour thicknesses of 0.018 in., 0.024 in., and 0.030 in. respectively.

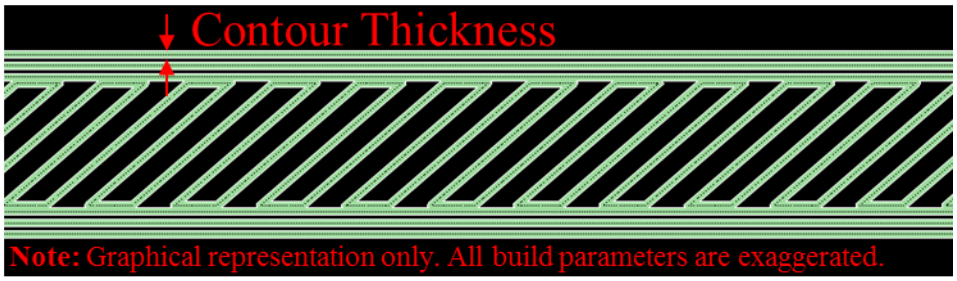

Figure 21. Contour Thickness Graphical Representation. The contour thickness is defined as the width of a single material pass of the outer shell of the geometry.

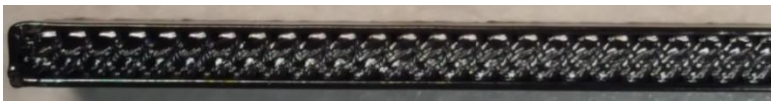

Figure 22. Contour Thickness: 0.018 in. Test Coupon. A single contour with a thickness of 0.018 in. was deposited to manufacture the test coupon.

Figure 23. Contour Thickness: 0.024 in. Test Coupon. A single contour with a thickness of 0.024 in. was deposited to manufacture the test coupon.

Figure 24. Contour Thickness: 0.030 in. Test Coupon. A single contour with a thickness of 0.030 in. was deposited to manufacture the test coupon.

Figure 25 below depicts the summary of the mechanical strength in relation to the different contour thicknesses. A linear relationship was observed from the data. The ultimate tensile strength increased proportionally with the contour thickness. The percent change between the contour thicknesses of 0.018 in. and 0.030 in. was 12%. The raw data for the contour thickness is found in Chapter 6Appendix E.

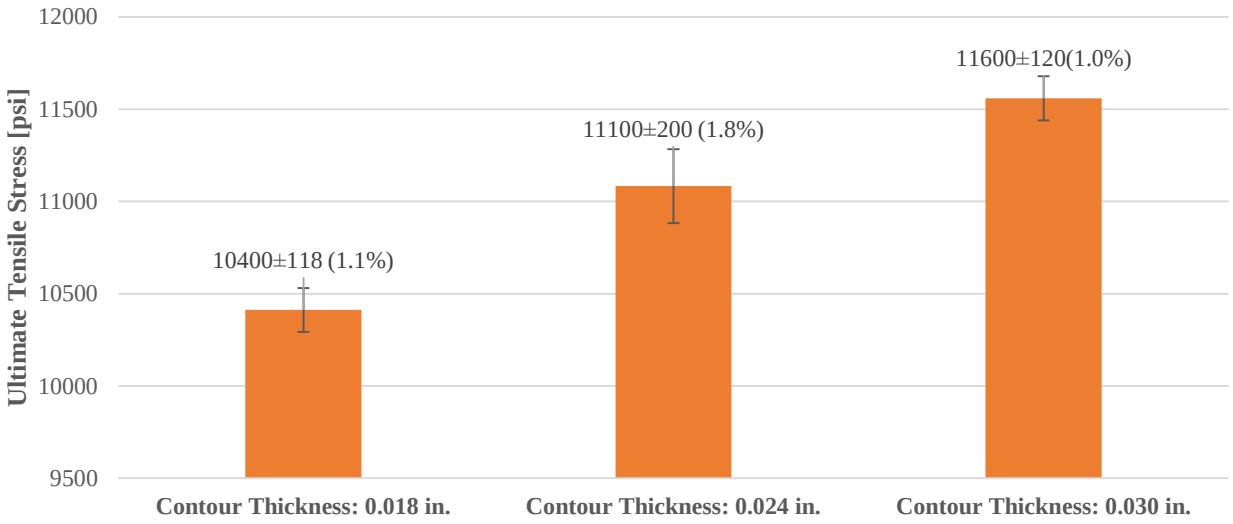

Figure 25. Contour Thickness Comparison Graph. The test coupons were manufactured in XZY Orientation with varying contour thicknesses. All other build parameters remained constant. The ultimate tensile strength increased linearly with the increase in contour thickness.

The contours in the gage section were extruded as continuous filaments parallel with the loading direction. Therefore, thicker contours are capable of enduring higher stresses. An individual ULTEM 9085 continuous filament has the same material properties as the bulk material properties. The layer-to-layer build process is the main reason that additive manufactured parts have varying mechanical properties from the bulk material properties.

3.1.3 Number of Contours

A series of static tests were performed to investigate the effects of the number of contours on the ultimate tensile strength. The contours increased from 1 – 3 contours in increments of 1. Figure 26 below defines the number of contours as the number of outer shells extruded before the raster fill. Figure 27 – Figure 29 depicts the samples with 1 contour, 2 contours, and 3 contours respectively. The sample with 3 contours did not have any raster fill due to the thickness of the geometry and the contour depth. The lack of raster fill may cause the part to delaminate under the right conditions. Further details regarding this phenomenon will be discussed in Chapter 4.

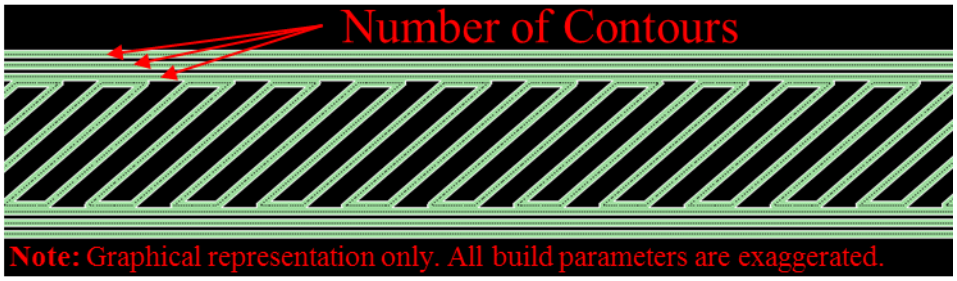

Figure 26. Number of Contours Graphical Representation. The number of contours is the number of outer shells that the machine deposits before filling in the interior of the geometry.

Figure 27. One Contour Test Coupon. One contour with a contour thickness of 0.020 in. was deposited to manufacture the test coupon.

Figure 28. Two Contour Test Coupon. Two contours with a contour thickness of 0.020 in. was deposited to manufacture the test coupon.

Figure 29. Three Contour Test Coupon. Three contours with a contour thickness of 0.020 in. was deposited to manufacture the test coupon. No raster fill was used due to the number of contours used and the overall thickness of the test coupon.

Figure 30 below compares the ultimate tensile strength for the three different quantities of contours. Similar to the contour thickness trend, the mechanical strength increased as the number of contours increased. The highest UTS was observed at 12100 psi with the coupon manufactured with 3 contours. The UTS decreased to 11800 psi and 10100 psi as the number of contours decreased to 2 contours and 1 contour respectively.

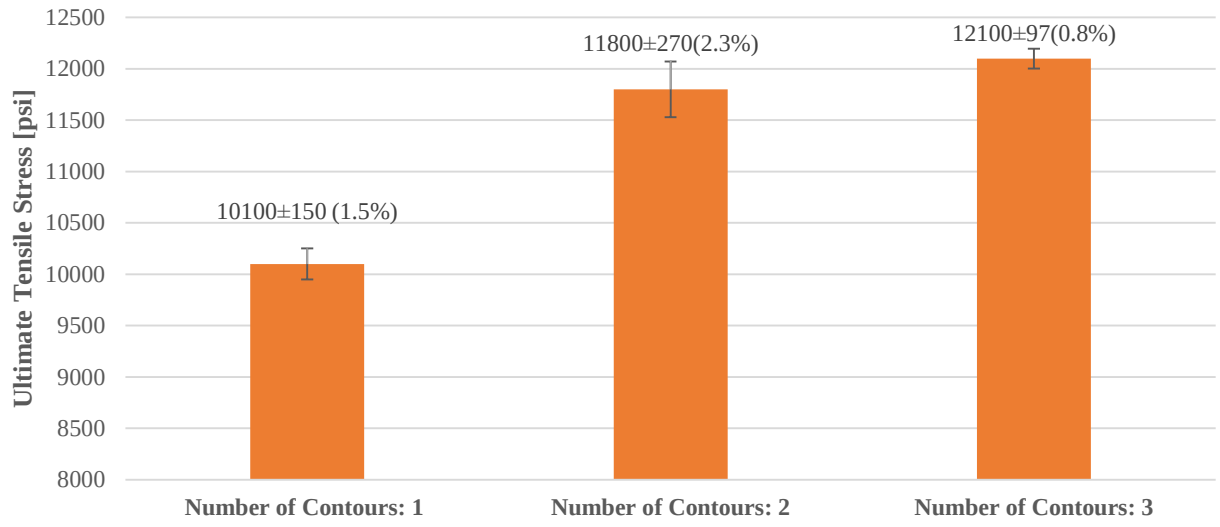

Figure 30. Number of Contours Comparison Graph. The test coupons were manufactured in XZY Orientation with varying numbers of contours with a constant contour thickness of 0.020 in. The ultimate tensile strength increases linearly with the increasing number of contours.

The larger number of contours allowed the coupon to exhibit higher ultimate tensile stress. This phenomenon is very similar to the one discussed in the previous section with the contour thickness. The number of contours directly correlated with the cross-sectional area of the continuous filament that is parallel to the loading direction. The larger area of the continuous filament exhibits properties that closely resemble the bulk material properties. However, if the load is applied perpendicularly to the sample, the mechanical strength will dramatically drop. This can be observed in the ZXY Orientation static test.

3.1.4 Contour Depth

The contour depth experiment was conducted to determine whether the number of contours or the contour thickness has a greater effect on the UTS. The contour depth is defined as the total thickness of the contour regardless of the contour thickness or the number of contours. Figure 31 depicts the definition of contour depth.

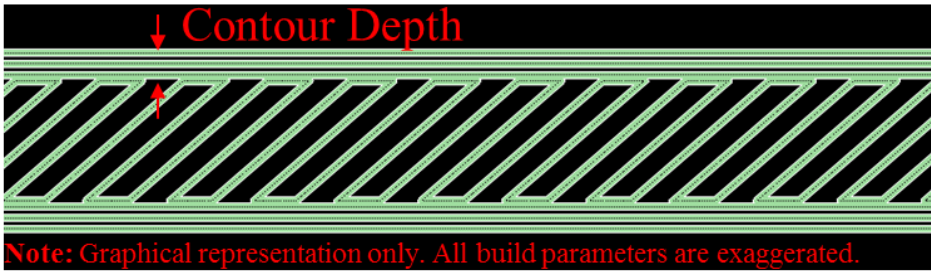

Figure 31. Contour Depth Graphical Representation. The contour depth is the mathematical product of the contour thickness and the number of contours.

The contour depth for this investigation was kept constant at 0.060 in. One sample population was manufactured with 3 contours, each with a contour thickness of 0.020 in. Another sample population was manufactured with 2 contours, each with a contour thickness of 0.020 in. Figure 32 – Figure 33 represent the variation of contour thicknesses and numbers of contours. Both samples did not have any raster fill due to the contour depth and the overall dimensional thickness of the coupons. Further analysis of the relations between raster fill and contour depth is provided in Chapter 4.

Figure 32. Contour Depth Test Coupon A. Three contours each with a contour thickness of 0.020 in. were deposited to generate a test coupon with a contour depth of 0.060 in.

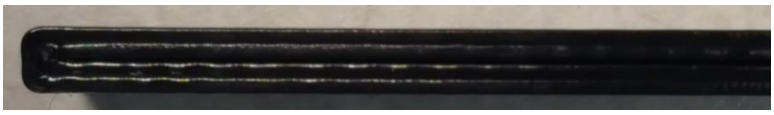

Figure 33. Contour Depth Test Coupon B. Two contours each with a contour thickness of 0.030 in. were deposited to generate a test coupon with a contour depth of 0.060 in.

The ultimate tensile strength between the two sample populations remained constant when the contour depths were identical. The average UTS for the specimen with 3 contours is 12100 psi and the average UTS for the specimen with 2 contours is 12200 psi. These two values are

relatively close as seen in Figure 34. The contour depth test demonstrated that the product of the two build parameters directly influences the strength of the coupon regardless of the values of the individual build parameters. A two-sample t-test was conducted to determine if the mean between the two sample populations are significantly different. The statistical tests produced a p-value of 0.017 which is greater than the significance level of $\alpha = 0.01$. Therefore, the mean strengths for samples produced with the two different contour depths are the same with a 99% confidence.

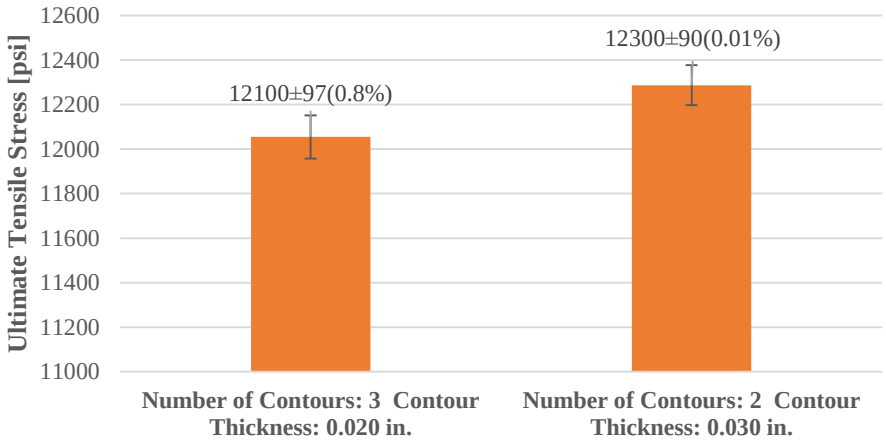

Figure 34. Contour Depth Comparison Graph. The coupons were manufactured in Orientation XZY with a constant contour depth of 0.060 in. The number of contours and the contour thicknesses were varied accordingly. The data suggested that the mean averages for both of the samples are not significantly different.

3.1.5 Raster Thickness

Five samples were manufactured with three different raster thicknesses to investigate the effect of raster thickness on mechanical strength. The raster thickness is the width of the material bead used to fill the interior of the geometry. Figure 35 is the graphical definition of the raster thickness. The raster thicknesses that were tested were 0.018 in., 0.024 in., and 0.030 in. Figure 36 – Figure 38 shows the different raster thicknesses.

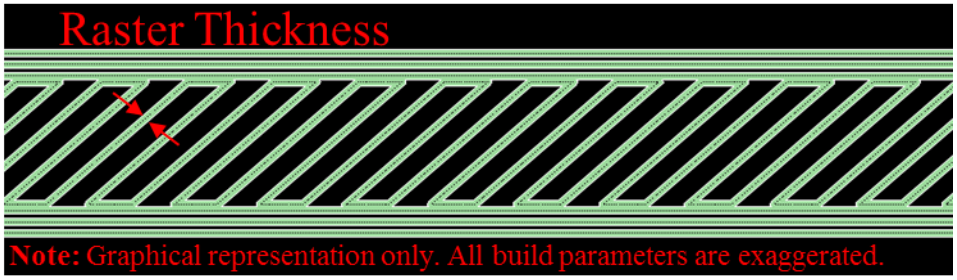

Figure 35. Raster Thickness Graphical Representation. The raster thickness is the thickness of a single bead of material used to fill the interior area of the geometry.

Figure 36. Raster Thickness: 0.018 in. Test Coupon. The interior of the geometry was filled with material beads with a thickness of 0.018 in.

Figure 37. Raster Thickness: 0.024 in. Test Coupon. The interior of the geometry was filled with material beads with a thickness of 0.024 in.

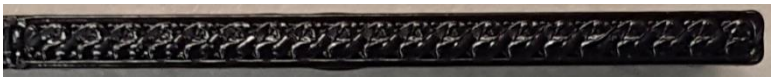

Figure 38. Raster Thickness: 0.030 in. Test Coupon. The interior of the geometry was filled with material beads with a thickness of 0.030 in.

The coupon with the largest raster thickness of 0.030 in. demonstrated the greatest tensile strength of 11000 psi. The ultimate tensile strength linearly decreased to 10500 psi and 10200 psi

the as the raster thicknesses were reduced to 0.024 in. and 0.018 in. respectively. Figure 39 compared the three different ultimate tensile stresses for the different raster thicknesses.

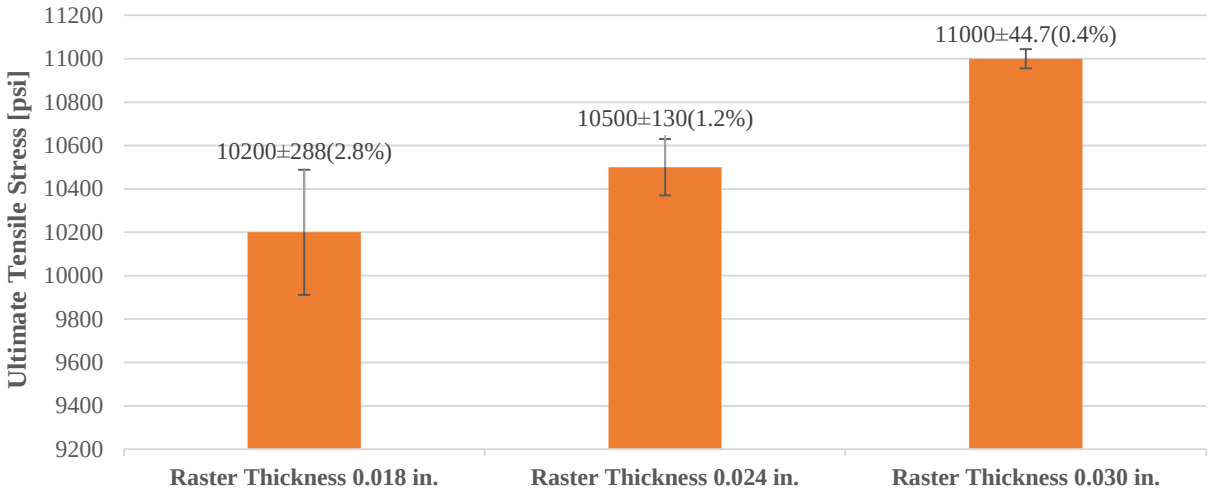

Figure 39. Raster Thickness Comparison Graph. The coupons were manufactured in Orientation XZY with a varying raster thickness. The ultimate tensile strength increased linearly with the raster thicknesses.

The larger raster thicknesses were able to handle higher loads because more continuous material was extruded to fill the interior of the parts. The larger percentage of continuous filament used in a part brings the mechanical properties of the part closer to bulk material properties.

3.1.6 Rectangular Bar Raster Thickness (Layer Adhesion)

Fifteen rectangular bars were manufactured with varying raster thicknesses to determine the effects of raster thickness on the layer adhesion strength in the build direction. The rectangular bars were manufactured in the ZXY orientation with the geometry from ASTM 3039. The build direction is in line with the direction of the force applied in the ZXY orientation. Therefore, the bond strength between the layers can be tested in this orientation. Figure 40– Figure 42 show the different rectangular bars with different raster thickness ranging from 0.018 in. – 0.030 in.

Figure 40. Rectangular Bar Raster Thickness 0.018 in. The interior of the rectangular bar was filled with a raster thickness of 0.018 in.

Figure 41. Rectangular Bar Raster Thickness 0.024 in. The interior of the rectangular bar was filled with a raster thickness of 0.024 in.

Figure 42. Rectangular Bar Raster Thickness 0.030 in. The interior of the rectangular bar was filled with a raster thickness of 0.030 in.

An Analysis of Variance (ANOVA) was performed using Minitab 8 to compare the means between the different raster thicknesses. Table 6 below is the Fisher Least Significant Different Method (LSD) Pairwise Comparison Table with a 95% confidence interval used to compare the different coupons with different raster thicknesses. The mean ultimate tensile strength between the coupons with a raster thickness of 0.024 in. and 0.018 in. was not significantly different because they both were assigned the group letter A. The mean ultimate tensile strength between coupons with a raster thickness of 0.018 in. and 0.030 in. was similar. There was a significant difference between the mean UTS between the coupons with 0.024 in. and 0.030 in. raster thickness because those samples do not share the same group letter. The ANOVA and the data collected suggested that a thicker raster thickness does not equate to a stronger layer adhesion. The medium size raster thickness of 0.024 in. demonstrated the highest UTS at 5910 psi. The

extreme ends of the raster thicknesses exhibited a UTS of 5710 psi and 5410 psi for raster thicknesses of 0.018 in. and 0.030 in. respectively. Figure 43 shows the comparison between the ultimate tensile strengths for the three different sample population.

Table 6. Fisher Pairwise Comparisons – Using Fisher Least Significant Differences Method

Description	Sample Size (N)	Mean [psi]	Grouping
Raster Thickness: 0.024 in.	5	5906	A
Raster Thickness: 0.018 in.	5	5708	A,B
Raster Thickness: 0.030 in.	5	5410	B

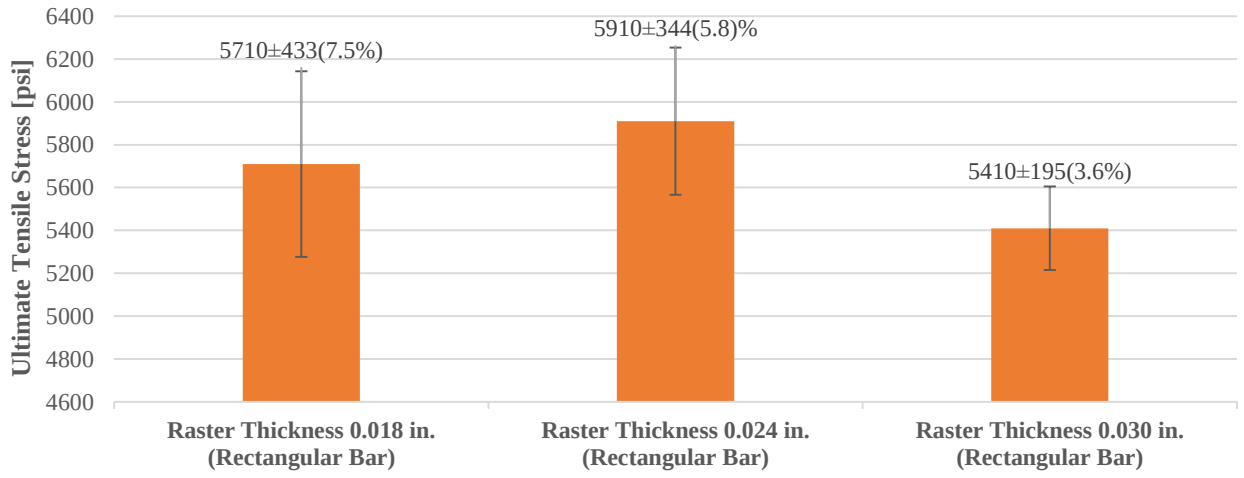

Figure 43. Rectangular Bar | Raster Thickness Comparison Graph. Five rectangular bars were manufactured in the ZXY Orientation. The geometry were selected based on ASTM

3.1.7 Raster Angle

Three different raster angles were tested to determine the effect of the interior fill orientation and the ultimate tensile strength of ULTEM 9085. The raster angle is defined as the angle between the x-axis of the build plane to the orientation of the raster bead. Typically, the raster angle

alternates 90º between each layer. Figure 44 and Figure 45 demonstrates the graphical definition of raster angle.

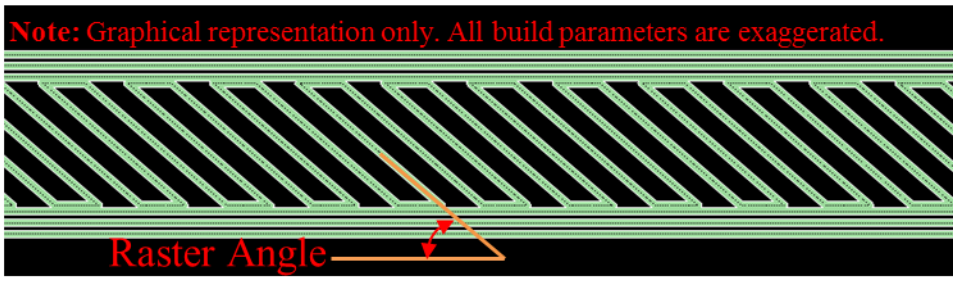

Figure 44. Raster Angle Graphical Representation (Layer n). The raster angle is defined as the angle between the x-direction of the machine with respect to the raster-direction.

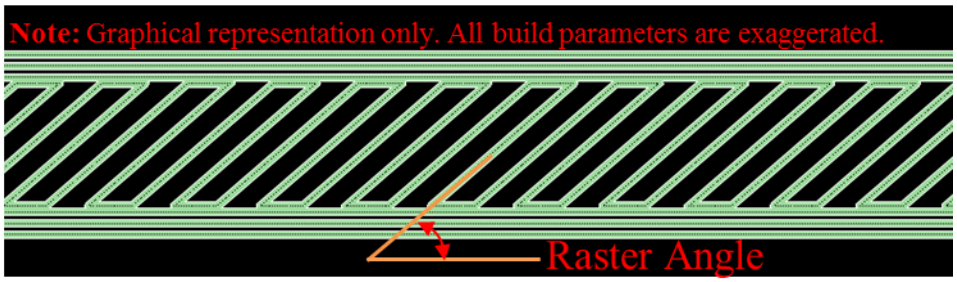

Figure 45. Raster Angle Graphical Representation (Layer n+1). The raster angle rotates by 90º between each alternating layer.

Fifteen coupons were manufactured with three different raster angles of 15º/-75º, 30º/-60º, and 45º/-45º. Figure 46 – Figure 48 shows the geometry of the different raster angles. The raster angles were selected based on the available configuration in Stratasys' Insight Revision software.

Figure 46. Raster Angle 15º/-75º. The test coupons were manufactured with a raster angle of 15º on layer n and a raster angle of -75º on layer n+1.

Figure 47. Raster Angle 30º/-60º. The test coupons were manufactured with a raster angle of 30º on layer n and a raster angle of -60º on layer n+1.

Figure 48. Raster Angle 45º/-45º. The test coupons were manufactured with a raster angle of 45º on layer n and a raster angle of -45º on layer n+1.

The raster angles of 45º/-45º and 30º/-60º exhibited very similar ultimate tensile stresses of 10100 psi and 10300 psi respectively. The raster angle 15º/-75º exhibited a much lower tensile stress of 9360 psi. The comparison between the three different raster angles can be observed in Figure 49.

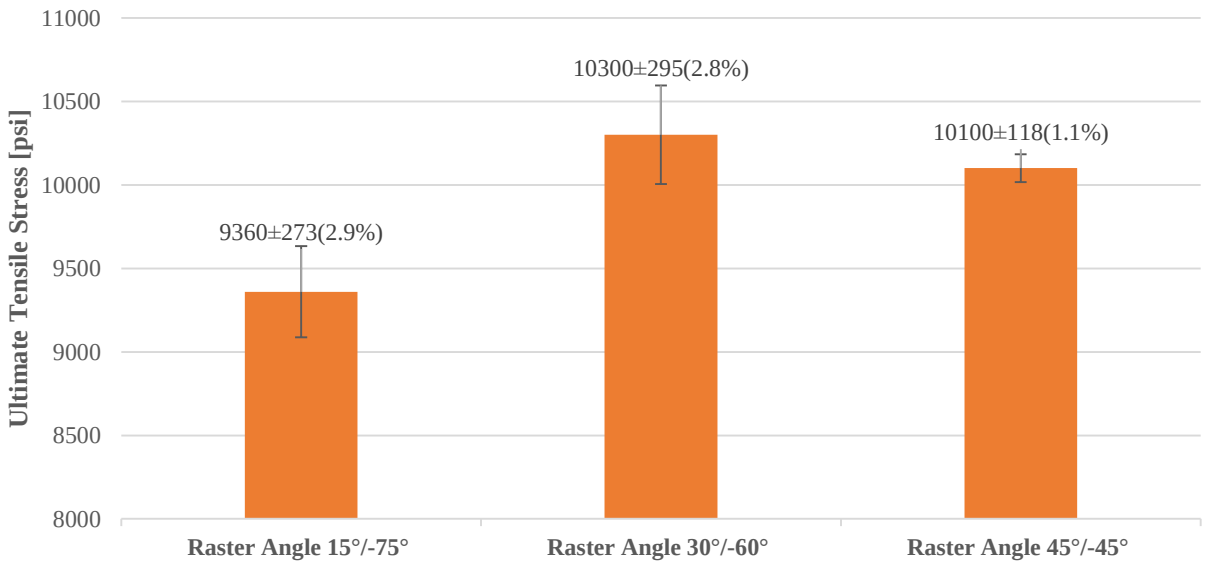

Figure 49. Raster Angle Comparison. The coupons were manufactured in Orientation XZY with a varying raster angles.

The raster angle 15º/-75º had the lowest strength because the interior beads were not oriented in the direction of the applied load. At the layers with the 15º raster angle, the load was distributed

between the filament and the bonds between each raster bead. However, the layers with the -75º raster angle did not contribute to the ultimate tensile strength as much as the 15º layer. Raster angles of 75º lead to an interior fill that was almost perpendicular to the orientation of the applied load. Previous tests (ZXY orientation) demonstrated that the part was the weakest when the load was perpendicular to the direction of the continuous filament. Raster angles 30º/-60º and 45 º /-45 º distributed the stress more evenly between the continuous filament and the bonds between each raster filament.

3.1.8 Mass and Dimension Analysis

The dimension analysis was performed to verify the geometric accuracy of the additive manufactured components. The thickness and the width of the gage section were recorded for all coupons, in addition to the mass. Please refer to Chapter 6Appendix B for the raw data of the mass and physical dimensions. The thicknesses and widths were averaged among the five samples for each build parameters. Figure 50 below shows the relationship between the thicknesses and widths.

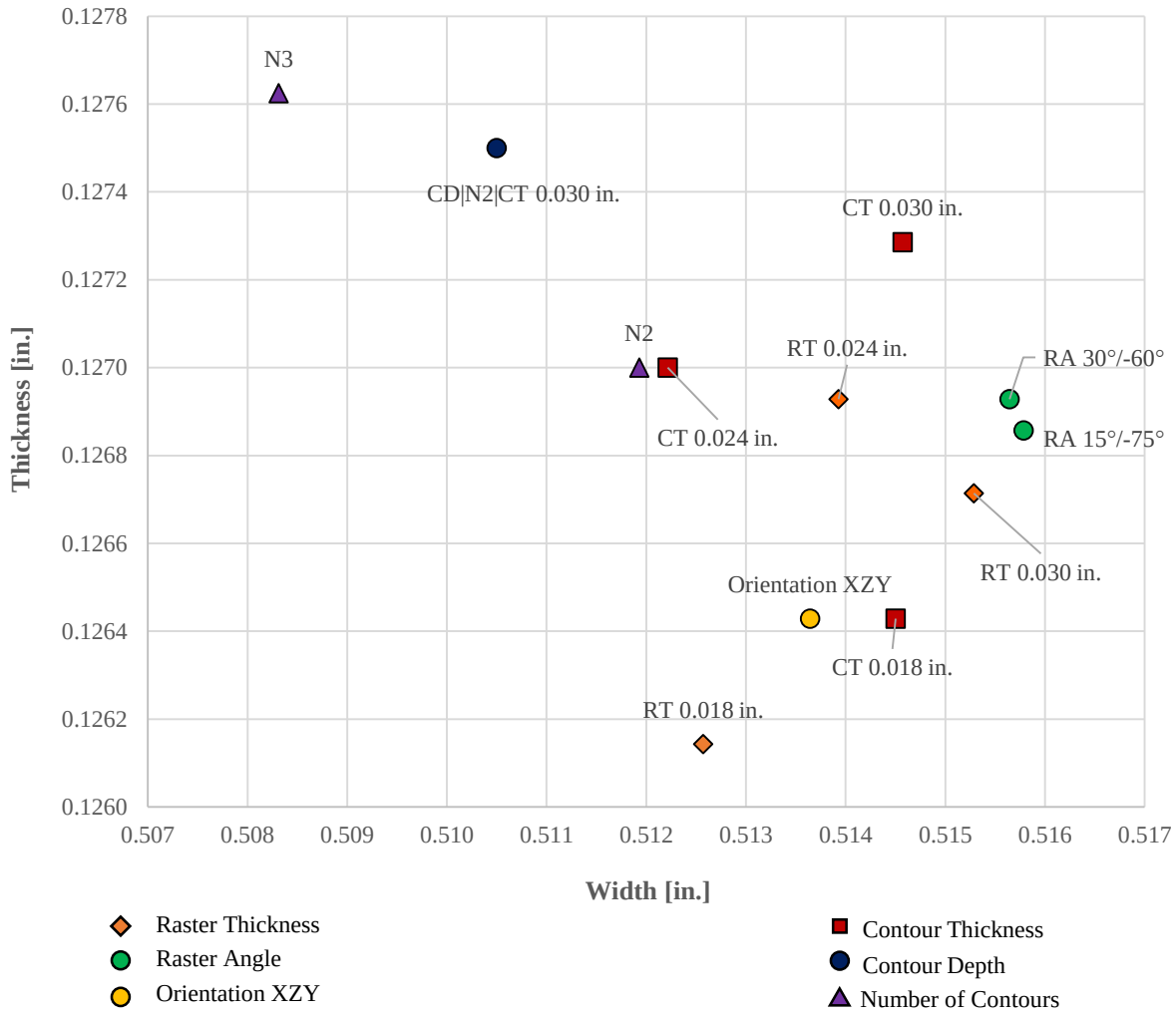

Figure 50. Gage Section Dimensional Accuracy Comparison between Different Build Parameters. The thicknesses and the widths of each sample populations were averaged and plotted together on a scattered plot.

The maximum width deviation from the samples was 0.1276 in. This value is 0.0026 in. larger than the design width of 0.125 in. However, the deviation is within range of the XY build platform resolution of ± 0.005 in. for the Fortus 400MC. The dimensions of additive manufactured parts in the XY plane are the most accurate. The maximum deviation for the width was 0.016 in. larger than the design width of 0.500 in. The dimensional accuracy in build direction is constraint by the layer height and the resolution of the machine. Figure 51 shows that the build parameter can also affect the dimensional accuracy in the build direction and the mass

of the coupon. A positive linear trend was observed as the mass of the coupon increased with the width.

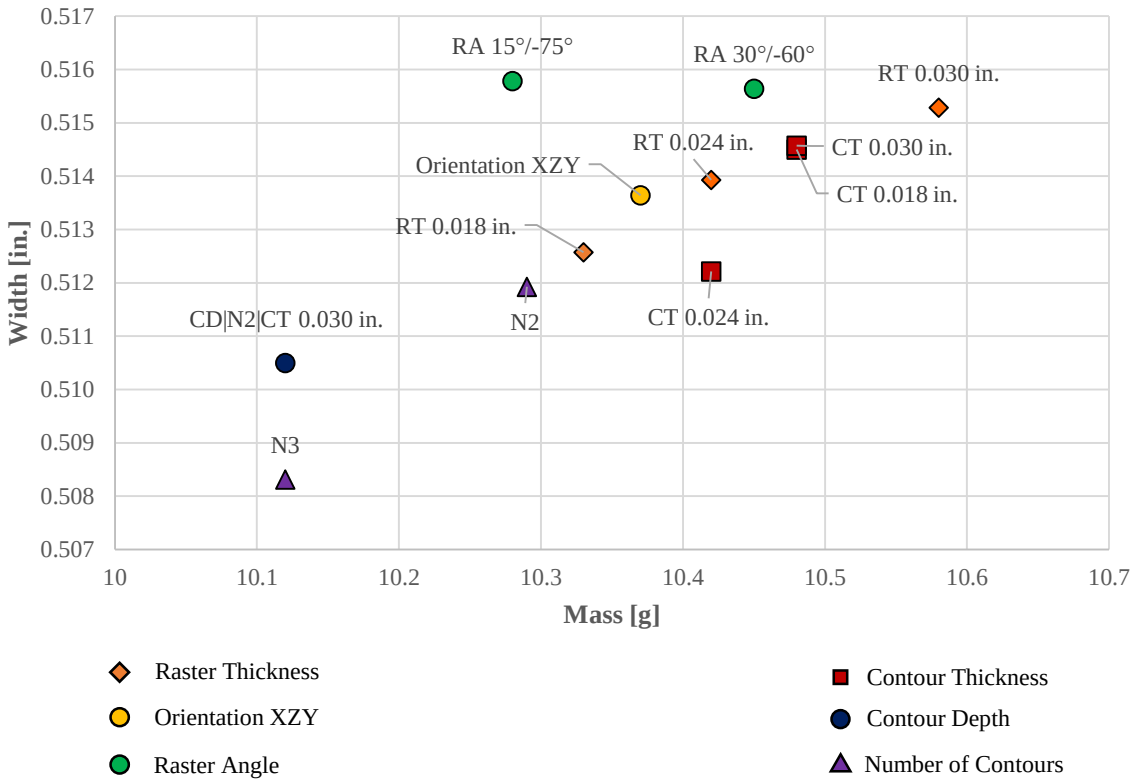

Figure 51. Gage Section Width Dimensional Accuracy in Relation to Mass of Coupon. The width for each sample population was averaged and plotted against the average mass of each sample population.

The dimension measurements demonstrated that the Fortus 400MC is capable of maintaining tight geometry tolerances in the build plane XY, regardless of the different build parameters. However, if the specified build parameters required geometric compensation, the machine uses the dimensional freedom of the build direction. For example, as the raster thickness increases the mass of the test geometry increases linearly with the width. In this scenario, the thickness in the XY plane remained within the resolution of the machine. However, the width increased with raster thickness. In other words, the layers become thicker with raster thickness. Figure 52 below shows the build Orientation XZY with the width and thickness labeled.

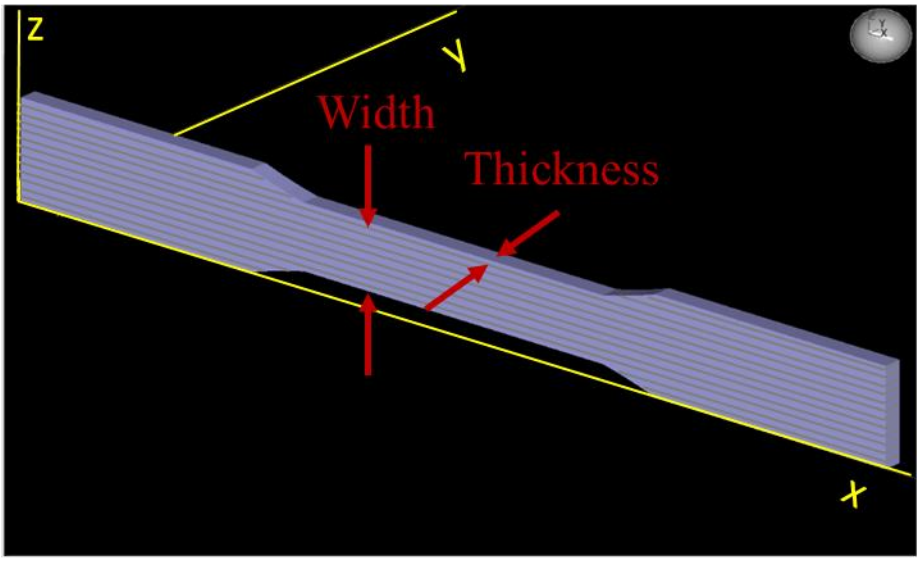

Figure 52. Dimensional Graphical Representation. The thickness refers the dimension perpendicular to the x-axis, while the width refers to the dimension parallel to the z-axis. The grey line represents the build layers of the coupon.

The mass analysis was broken down into two categories. The first category compared all of the contour-dominant build parameter variations such as contour thickness, number of contours, and contour depth. Figure 53 below illustrates a negative linear relationship between the mass and the ultimate tensile strength for contour dominant build parameters. The red squares represent the different contour thicknesses. The mass of the contour thicknesses remained constant with the exception of the 0.024 in. However, the ultimate tensile strength increased with contour depth. As the number of contours was increased, less raster fill was deposited in the interior of the geometry. Thus, the mass decreased with increasing contour depth. This observation suggested that the majority of the tension load was supported by the contour because the specimen with 2 contours and a contour thickness of 0.030 in. exhibited the highest ultimate tensile stress of 12300 psi with a low mass of 10.12 g. The low mass was contributed by the lack of raster fill and voids.

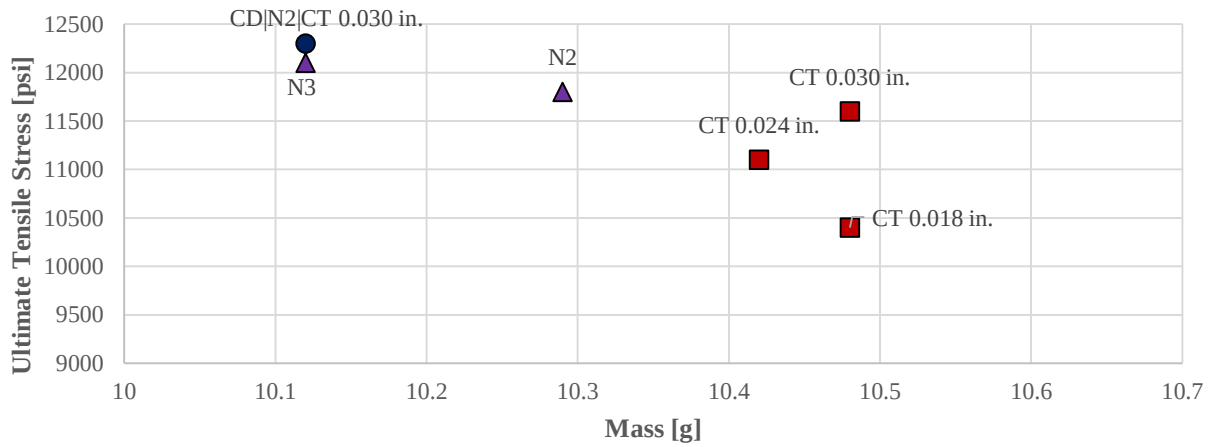

Figure 53. Contour Dominant Build Parameter Variation Comparison between Mass and UTS. The mass for the sample population with varying contour build parameters were plotted against the ultimate tensile stress.

The second category compared the mass and ultimate tensile load of all the raster dominant build parameter variations such as the raster angle and the raster thickness. Figure 54 below shows the correlation between the mass and the ultimate tensile strength of the raster dominant build parameters. The increased in raster thicknesses resulted in both an increase in ultimate tensile stress and mass. The thicker raster slightly increased the width of the gage section by 0.0153 in. as shown in Figure 51. Additionally, the mass for the raster thickness increased linearly with the width. The increase in mass and width at the gage section allowed the thicker raster to have a higher ultimate tensile strength. Similarly, the raster angle demonstrated similar characteristics. The raster angle of 30º/-60º has the largest mass of 10.45 g and an ultimate tensile stress of 10300 psi. While, the raster angle of 15º/-75º has the lowest mass of 10.28 g and an ultimate tensile stress of 9360 psi. The gage section width of the 15º/-75º and 30º/-60º raster angle remained relatively constant at 0.516 in. Therefore, the mass is one of the main contributors to the ultimate tensile strength for the various raster angle.

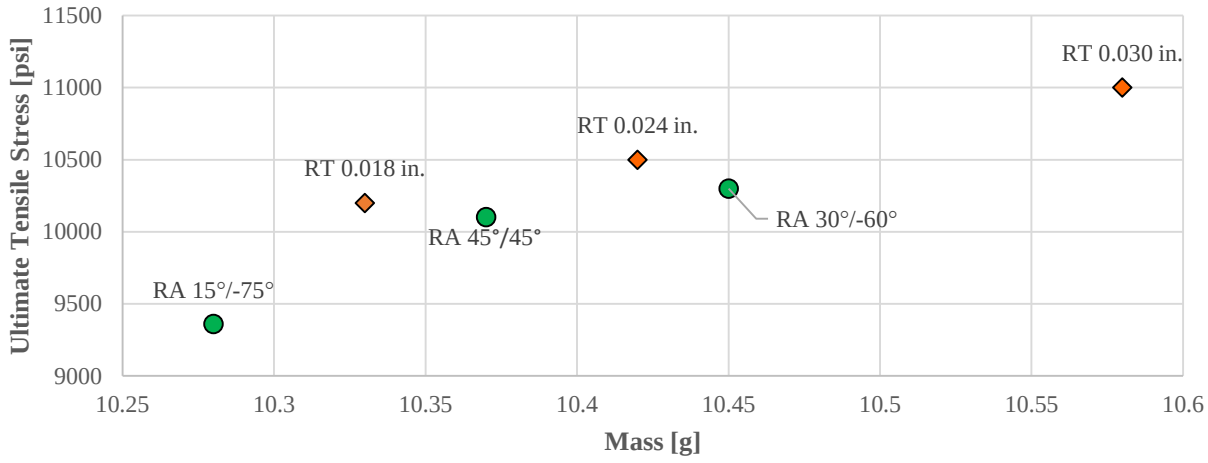

Figure 54. Raster Dominant Parameter Variation Comparison between Mass and UTS. The mass for the sample population with varying raster build parameters was plotted against the ultimate tensile stress.

3.2 Fatigue Testing Results

3.2.1 Standard Tension-Tension Fatigue Test Results (R=0.1)

The standard tension-tension fatigue testing was performed using the ASTM 638 Type I geometry. Three sample were tested at each of the four stress levels of 80% UTS, 60% UTS, 30% UTS, and 20% UTS. Figure 55 below shows the S-N curve for AM ULTEM 9085. The fitting curve for the dataset was generated by the methods mentioned in ASTM D7791. The average fatigue life for stress levels 80%, 60%, 30%, and 20% of ultimate tensile strength was 385, 1923, 24999, and 91822 cycles respectively. Please refer to Appendix F for the raw data of the standard tension-tension fatigue tests.

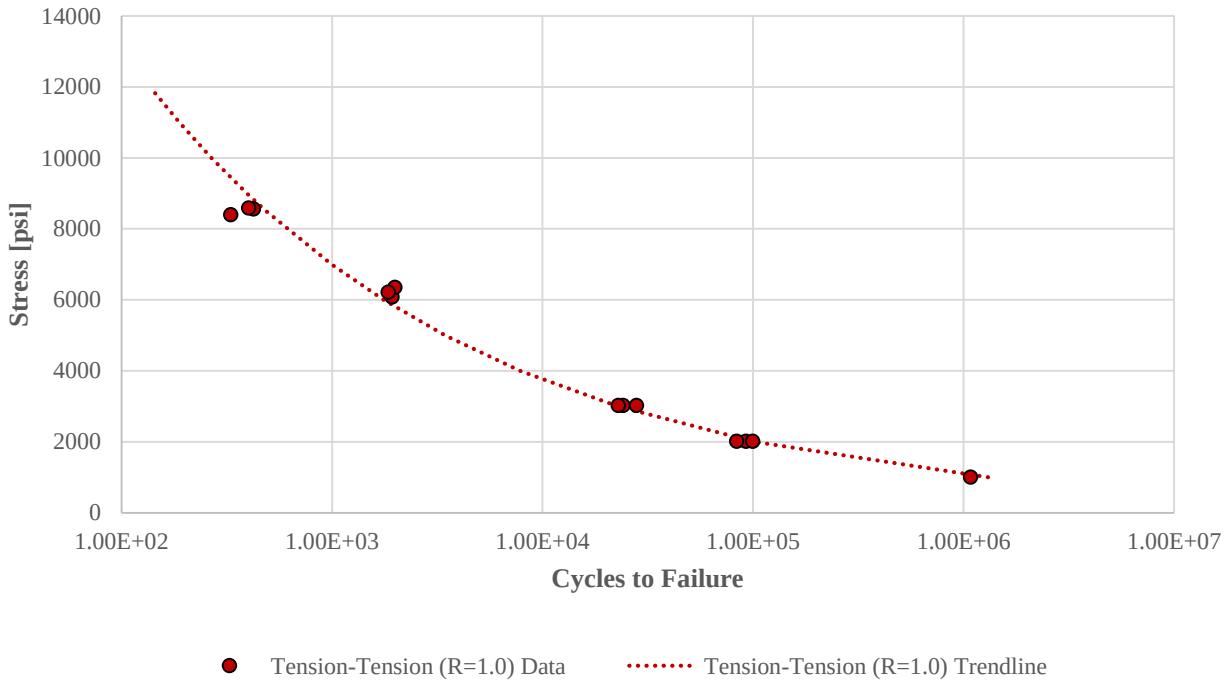

Figure 55. S-N Curve Generated by Virginia Tech. 3 samples were tested at the stresses of 8517 psi (80% UTS), 6127 psi (60% UTS), 3030 psi (30% UTS), and 2020 psi (20% UTS). Only 1 sample was tested at the stress of 1010psi (10% UTS) due to the long nature of fatigue testing. All coupons were manufactured in the XZY orientation with the default build parameters (Table 2).

The results from the standard tension-tension fatigue test were compared to another data set produced by Fischer et al. Fischer S-N curves for ULTEM 9085 were generated by testing five specimen at various stress levels from 10% to 90% of the ultimate tensile strength. The tension-tension fatigue data produced at Virginia Tech compares very well with the data from Fischer & Schoppner. (See Figures 56.)

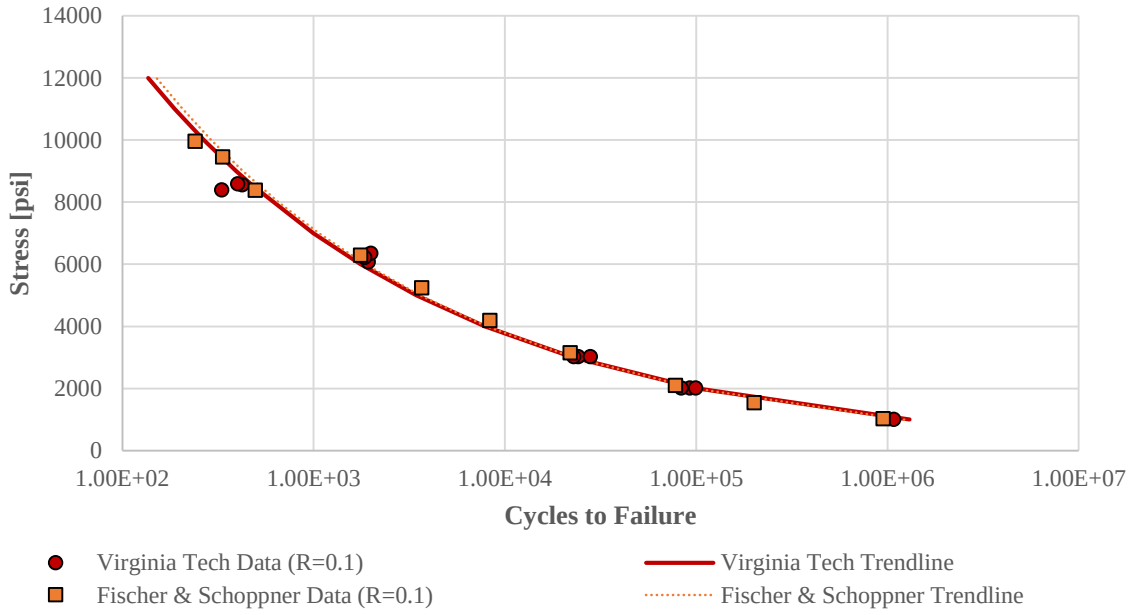

Figure 56. Tension-Tension Fatigue Data Comparison between VT and Fischer & Schoppner. The data points and the S-N curves from the two research groups correlated extremely well. Different load frames were used between VT (MTS 810 % ElectroPuls E1000) and Fischer & Schoppner (Type Zwick HC10). All coupons were manufactured in the XZY orientation with the default build parameters (Table 2).

3.2.2 Build Parameters Variation Fatigue Test Results (R=0.1)

Two different build parameters were varied to determine the effects of raster thicknesses and contour thicknesses on the ultimate tensile stress of ULTEM 9085. Three coupons with a contour thickness of 0.030 in. were tested at each of the four different stress levels of 80% UTS, 60% UTS, 30% UTS, and 20% UTS. Due to the resource constraints, three coupons with a raster thickness of 0.030 in. were tested at each of the two stress levels of 30% UTS and 20% UTS.

Figure 57 below plotted the S-N curve for the default build parameters coupons in red with circles and a dotted line, the S-N curve for the 0.030 in. contour thickness coupons in orange with triangles and a dashed-dot line, and the S-N curve for the 0.030 in. raster thickness coupons in purple with squares and a dashed line. At the 80% UTS, the average fatigue life increased from 384 cycles to 808 cycles (103% increase) when the contour thickness was increased from

0.020 in. to 0.030 in. Similarly, at 60% UTS the thicker contour coupons exhibit an average of 42.8% higher fatigue life (2746 cycles), and at 30% UTS the fatigue life increased by 14% (28556 cycles). At lower stress levels, the two sample populations have very similar fatigue life.

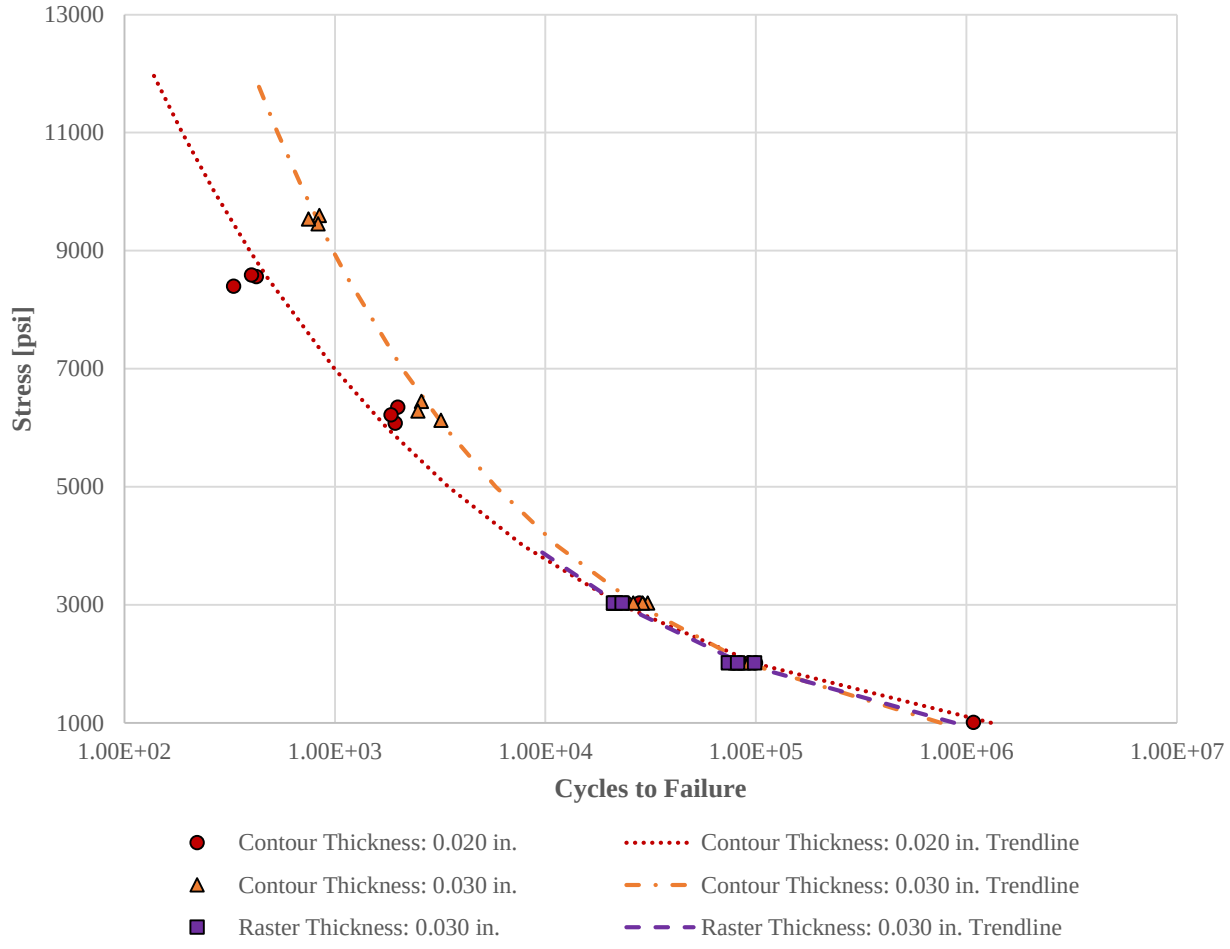

Figure 57. S-N Curve for Different Build Parameters. Due to limited resources the 6 samples with a raster thickness of 0.030 in. were tested at 30% UTS and 20% UTS to generate the purple S-N curve. 9 samples with contour thickness of 0.030 in. were used to generate the orange S-N curve. All coupons were manufactured in the XZY orientation with the default build parameters (Table 3).

The thicker contour improved the fatigue life because a thicker contour means a higher concentration of continuous material deposited in the direction of the applied load. However, the

fatigue life was not significantly improved at the lower stress levels for the coupons with the thicker contour.

In contrast, the average fatigue life decreased at the lower stresses when the raster thickness was increased from 0.020 in. to 0.030 in. The average fatigue life decreased from 24998 cycles to 21853 cycles (12.6%) and 91822 cycles to 84750 cycles (7.70%) with respect to the stress levels of 30% UTS and 20% UTS. The smaller number of raster passes in the infill contributed to the decrease in fatigue life. The larger number of raster passes between the contours has more surface area for adhesion between the raster filament. Once delamination between the raster filaments occurred, the infill of the coupon no longer carried the applied load effectively, which accelerated the failure. Please see Figure 58 and Figure 59 for further explanation of raster passes.

Figure 58. Raster Passes for Raster Thickness: 0.018 in. Coupons. The raster passes are defined as the line of material that the machine deposit to fill in the interior of the part. The red dots resembled the beginning of each raster passes. 34 raster passes exist for 0.018 in. raster thickness coupon in the gripping region. The default build parameter has a raster thickness of 0.020 in. and 24 raster passes in the gripping region. The 0.018 in raster thickness was depicted above to clearly demonstrate the number of raster passes.

Figure 59. Raster Passes for Raster Thickness: 0.030 in Coupons. The raster passes are defined as the line of material that the machine deposit to fill in the interior of the part. The red dots resembled the beginning of each raster passes. 21 raster passes exist for 0.030 in. raster thickness coupon in the gripping region.

3.2.3 Low Stress Tension-Tension Fatigue Test Results (R=0.1)

Gillaugh et al. attached strain gauges to flow distortion devices called StreamVanes to study the static and unsteady dynamic loads.[15] The StreamVane was placed under static load on a "bench top" to investigate the structural response. Additionally, the unsteady dynamic stresses were

investigated by mounting the StreamVane to an in-flow cascade facility and varying the Mach Number from M=0.351 – M=0.482. The maximum static stress observed was 280 psi and the maximum steady state dynamic stress observed was 9.4 psi. Per request of the Air Force Research Laboratory, three ASTM 638 Type I geometry coupons with default build parameters were tested at 2.5% of ultimate tensile strength. The curve fit for the Virginia Tech fatigue data suggested that the specimen would fail at 217000000 cycles at stress level of 2.5% UTS. This cycle count equates to a test duration of 502 days at 5 Hz cyclic frequency. The tests were halted at 1000000 cycles and fatigue run-out was declared because of the time and resource constraints. Table 7 below shows that none of the three coupons failed after a million cycles.

Table 7. Low Stress Tension-Tension Fatigue Test Results

Ultimate Tensile Strength [psi]:				**10100**	
% UTS	**Test Code**	**σ_{max} [psi]**	**σ_{min} [psi]**	**Cycles**	**Status**
2.5%	TT1	250	25	1075738 – no failure	Completed
2.5%	TT2	250	25	1697761 – no failure	Completed
2.5%	TT3	250	25	1209296 – no failure	Completed

3.2.4 Fully Reversed Testing (R=-1)

The fully reversed tests were conducted using a shorter coupon geometry due to buckling issues during the compressive load. The new coupon geometry reduced the gage section length to 1 in. and the gripping region length to 0.858 in. One shortened coupon manufactured with the default build parameters was used to verify the tension-tension fatigue life at 30% UTS. Figure 60 shows that the results from the verification test matched very well with the original fatigue data using

the standard ASTM 638 Type I geometry. The fatigue life for the shortened coupon is represented by the orange square. The shortened coupon geometry was used for the remainder of the fully reversed fatigue tests.

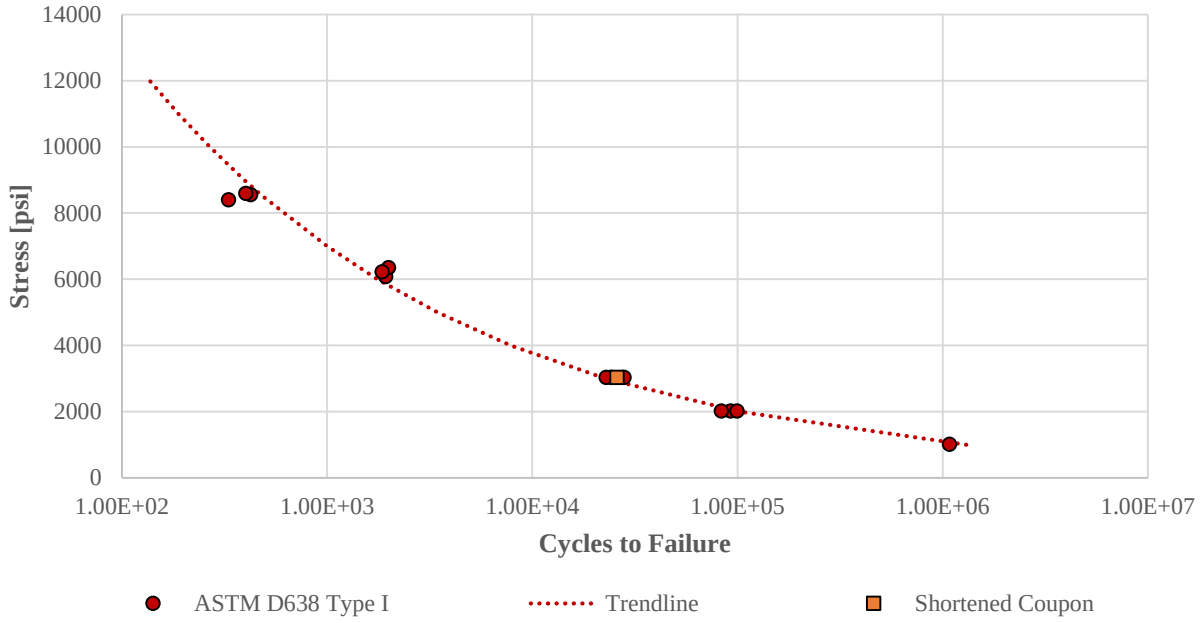

Figure 60. Shorten Coupon Fatigue Characterization Comparison to Standard ASTM D638 Geometry. The orange square represents the fatigue life for the shortened coupon at 30% UTS. The fatigue life of the new geometry matched very well with standard testing geometry. Only one shortened coupon manufactured in the orientation XZY with the default build parameters was used for verification due to the limited resource.

Initially, the modified Goodman approach was used to correlate the fully reversed data to the tension-tension data. However, the data collected did not support the modified Goodman approach. As a result, three samples were tested at four different stress levels of 25%, 20%, 15%, and 10% of the ultimate tensile strength to generate the fully reversed fatigue characteristics for additive manufactured ULTEM 9085. Figure 61 below shows that the tension-tension data is represented by the red circles, the tension-compression data is represented by the orange squares, and the Modified Goodman Prediction is represented by the purple dash-dot line. The data points for the modified Goodman prediction was generated based on Equation (2). The calculated

equivalent stresses were input into the characteristic equation for the standard tension-tension fatigue data to calculate the equivalent fatigue life. The tension-compression loading is slightly more damaging to the test samples than the tension-tension loading. However, the damaging effect is not as severe as suggested by the modified Goodman approach. (The Modified Goodman relationship is a very conservative estimation for additive manufactured ULTEM 9085.)

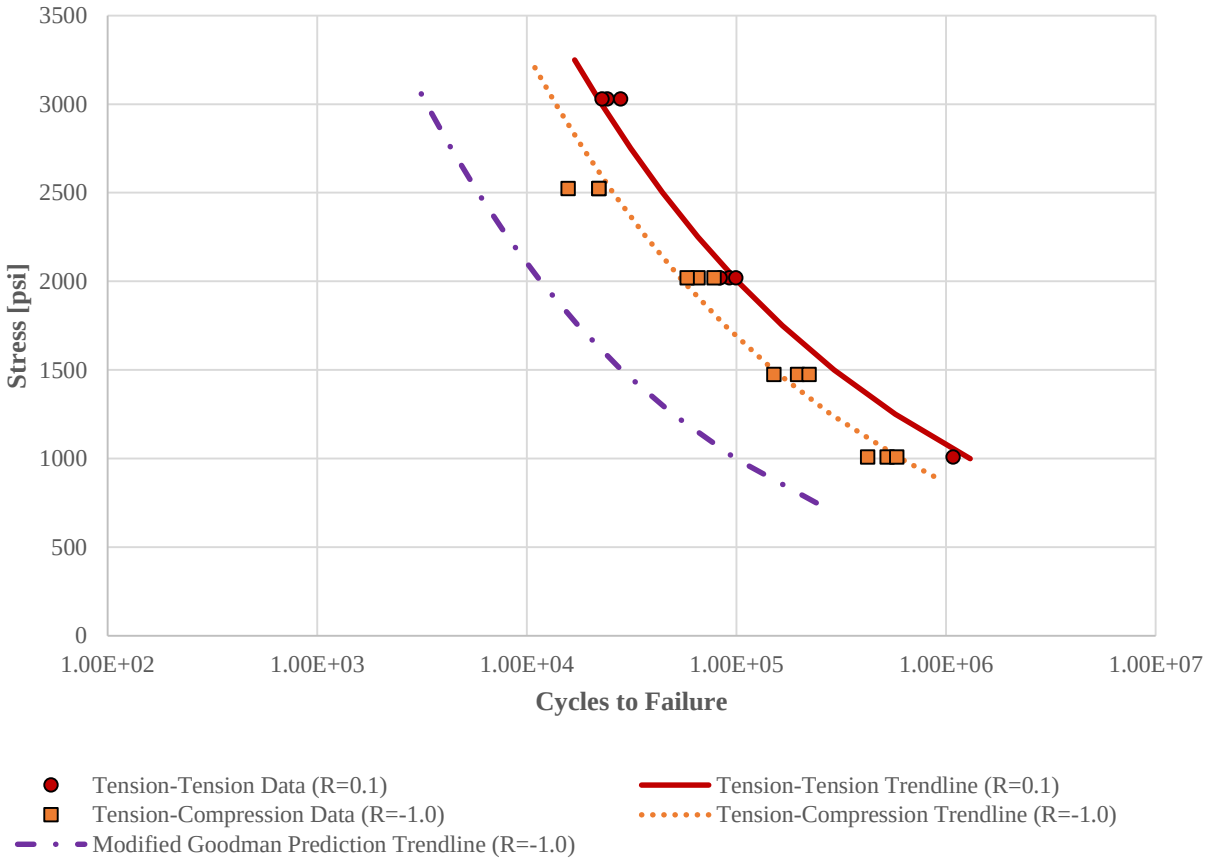

Figure 61. Fully Reversed Fatigue S-N Curve Compared with Tension-Tension Fatigue S-N Curve. The tension-compression cyclic load is more damaging to additive manufactured ULTEM 9085. However, the effects are not as extreme as the Modified Goodman Relation. The tension-compression data was generated using the shortened coupons manufactured orientation XZY with the default build parameters (Table 5).

Because of the extremely conservative nature of the modified Goodman approach, a simple effective tensile Model (ETM) was developed to better predict the fatigue life of ULTEM 9085.

The Effective Tensile model assumes that tensile fatigue loading is much more damaging than compressive loading, to the extent that the compression loading can be neglected. A potential physical basis for this behavior is that crack growth occurs only during the tensile portion of the load cycle. Figure 62 shows the cyclic sine wave that is used for fatigue testing. The dotted orange line represents the cyclic loading when R = 0.1 and the solid red line represents the cyclic loading when R =-1.0. The load is always positive during the tension-tension tests. Therefore, the entire stress range for tension-tension tests contributes to the crack propagation. However, only half of the stress range for the tension-compression loading contributes to the crack growth.

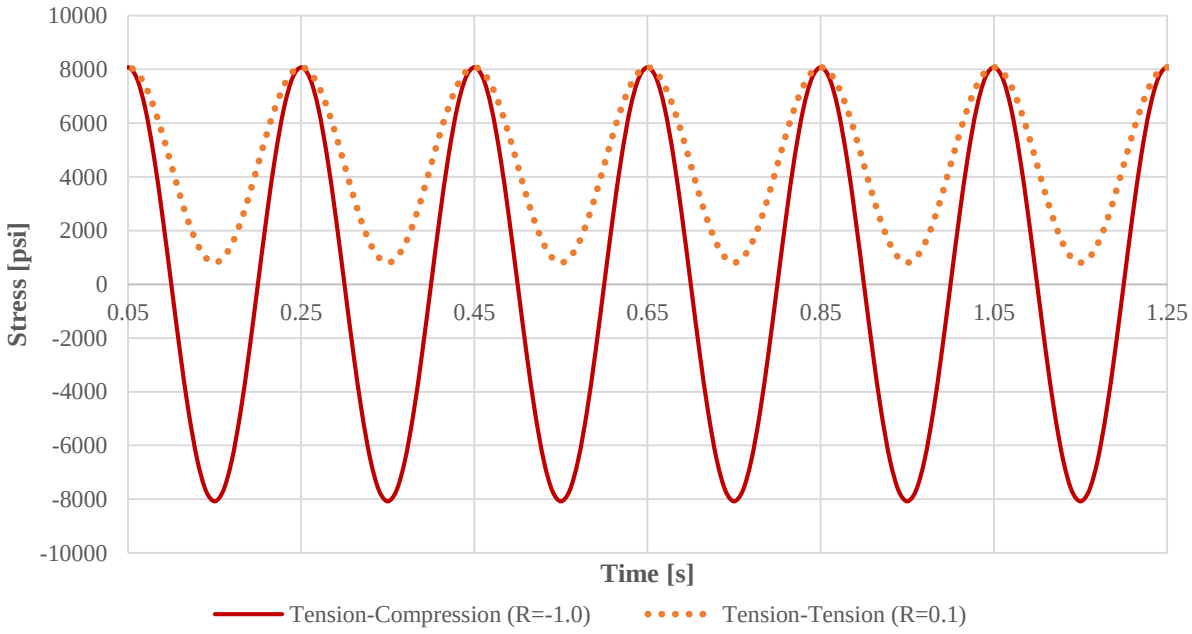

Figure 62. Sine Wave of Cyclic Loading for Fatigue Tests. The solid red line represents the fully revered loading and the orange dotted line represents the tension-tension loading. The ETM assumes that the crack only propagates when the stress is above the zero axis.

The effective stress range can be calculated using Equation **Error! Reference source not found.** w here $\Delta\sigma_{effective}$ is the effective tensile stress acting on the part, σ_{max} is the maximum stress, and σ_{min} is the minimum stress. The assumption that the crack only propagates during the tension

load constricts $\sigma_{min} \geq 0$. If $\sigma_{min} < 0$, the assumption that $\sigma_{min} = 0$ is made to satisfy the condition that the crack only grows during tension loading.

$$\begin{aligned} \Delta\sigma_{effective} &= \sigma_{max} - \sigma_{min} && \sigma_{min} \geq 0 \\ \Delta\sigma_{effective} &= \sigma_{max} && \sigma_{min} < 0 \end{aligned} \tag{12}$$

The data for the tension-tension fatigue tests, the tension-compression fatigue tests, the Modified Goodman prediction, and the Effective Tensile model are plotted in Figure 63. The red solid line represents the curve fit for the standard tension-tension data the orange dotted line represents the curve fit for the tension-compression data. The blue dashed line was generated by inputting the tension-tension fatigue data into the Effective Tensile Model. The EFM generated an S-N curve that closely resembled the S-N curve generated by the tension-compression data. The EFM is a much more effective model to use to correlate the different R-Ratios for FDM ULTEM 9085. The purple dashed-dotted line represents the conservative Modified Goodman prediction.

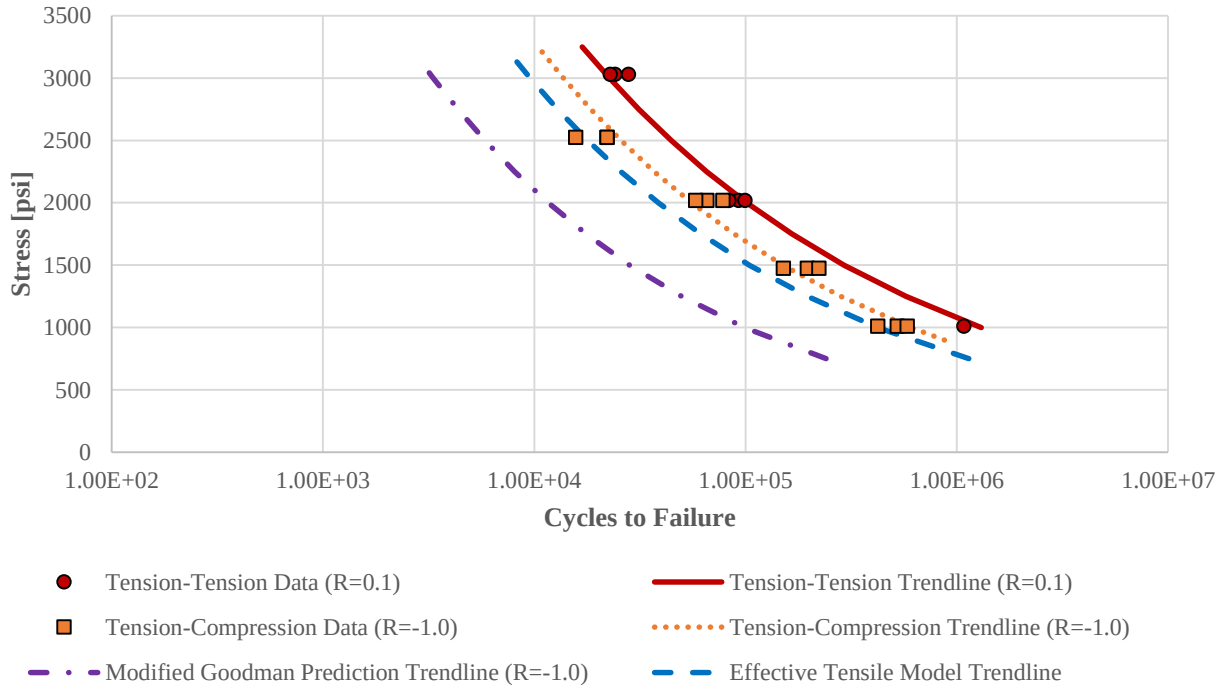

Figure 63. Tension-Compression Model Comparison to Fully Revered Trendline. The Modified Goodman was an extremely conservative approach to correlate the different R=Ratios for ULTEM 9085. The ETM generated a S-N curve that closely resembled the fully reversed data collected.

Chapter 4 End Use Parts Manufacturing Best Practices

4.1 Layer Stepping

The discretized, layer-to-layer build process leads to stress concentrations. These stress concentrations can be seen in Figure 64 below. The layer stepping occurred when the x-axis and y-axis dimensions change between each layer. For the build orientation XZY, the stepping occurred at the radius between the gage section and the gripping section. The effects of these stress concentrations can be reduced by minimizing the geometric differences in the XY build planes with respect to the build direction. Additionally, smaller nozzle sizes can be used to decrease the layer height between each layer. However, further analysis is needed to optimize the layer height and the effects of stress concentrations. The optimization is geometry dependent. Therefore, a general solution cannot be provided.

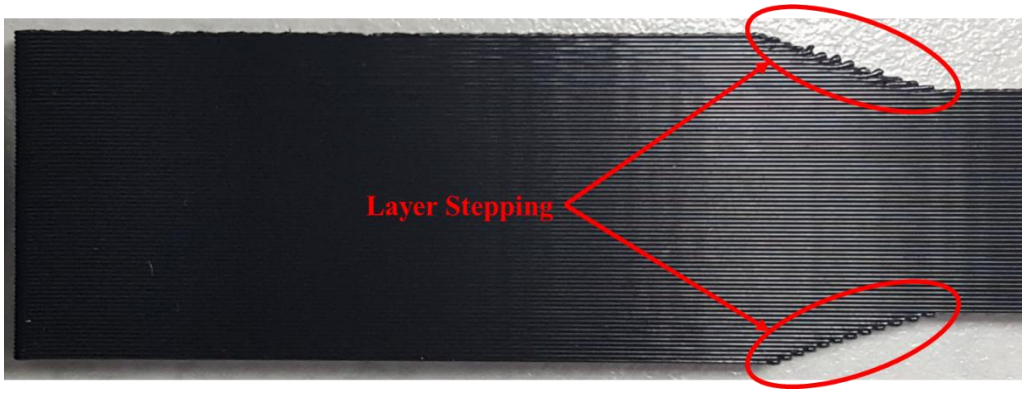

Figure 64. Layer Stepping Due to Discretization of Radius. The layer stepping on the radiuses of the coupon creates a stress concentration.

4.2 Stress Concentration Caused by Material Voids

Extrusion additive manufacturing technologies layer the part with elliptical beads of material. The vertical and horizontal stacking of the thermoplastic elliptical cylinders created voids within

the additive manufactured part. These voids can affect the mechanical strength of the components. Figure 65 below depicts the locations of the voids that naturally occurred at the end of each raster bead. The change in direction and the radius of the material bead prevented the individual roads from being flush with one another. Thus, the voids existed at the outer perimeter of the raster fill. The voids naturally occurred at the necking region of the ASTM D638 Type I geometry. These voids created a stress concentration that caused multiple coupons failing at the shoulder of the test geometry. Previous research was performed to compare the results from ASTM D638 Type I geometry and ASTM 3039 geometry.[18] The data suggested that ASTM 3039 geometry were better suited for additive manufactured parts. However, ASTM D638 Type I geometry is widely used for testing.

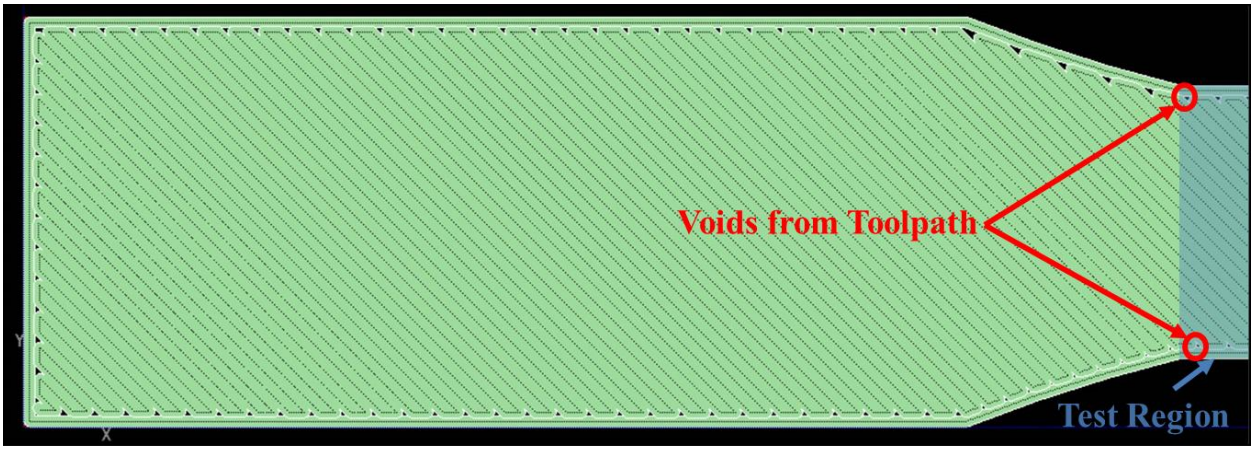

Figure 65. Stress Concentration Generated by Voids. Material voids will always occur in the current extrusion additive manufacturing technologies. The voids are the gaps between the stacked elliptical cylinders of thermoplastic.

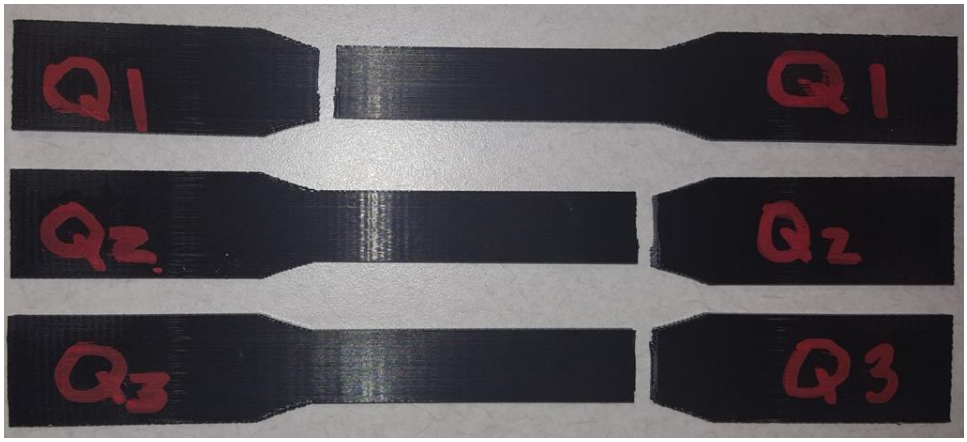

Figure 66. Typical Failure at the Neck Region Due to Voids. The voids in at the radius created a stress concentration at the neck causing the coupon to fail in this region. Other coupons failing towards the middle of the gage section demonstrated very similar ultimate tensile strength as coupons failing closer to the neck region.

One method that can be used to minimize the percentage of voids in an FDM part is by decreasing the raster-to-raster air gap and the contour-to-raster air gap. The default setting for both of the build parameters are 0.0 in. Previous study by Spikowski et al. have suggested that a negative air gap will increase the density of the part and increase the ultimate tensile strength.[7] However, utilizing negative air gap increases the risk of the nozzle clogging, which will result in a failed print. Based on experiences from Stratasys' (OEM) engineers, clogging was an issue when the air gaps were set to values smaller than -0.002 in. The recommendation for this scenario is to keep the air gaps build parameters at 0.0 in. to minimize production defects. The nozzle can clog at any time during the print. If the nozzle clogs towards the end of the print, then significant material, time, and cost were invested into a failed print.

4.3 Stress Concentration Caused by Seam Placement

The seam placement is another form of stress concentration caused by the different build parameters. The default setting for the Fortus 400MC at Virginia Tech placed the seam at the exact same coordinates between each layer as shown in Figure 67 and Figure 68. The seam placement at the shoulder of the test coupon caused consistent failure at the same location.

Figure 69 below shows that the crack initiates at the shoulder and propagates through the rest of the cross-sectional area.

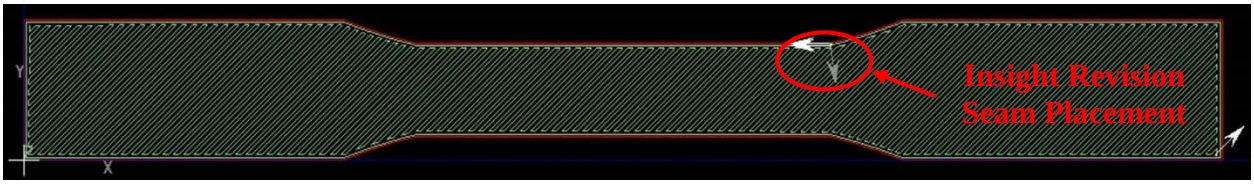

Figure 67. Stress Concentration Due to Seam Placement in Stratasys Insight Revision. Stratasys Insight Revision software placed the seam at the same coordinates between each layer. The seam placement in the contour significantly weaken the material properties of ULTEM 9085.

Figure 68. Stress Concentration Due to Seam Place on Test Coupon. The contour seam placement is at the same location between each layer on the test coupon.

Figure 69. Failure Outside of the Test Region Due to Seam Placement. The crack propagated from the seam into the shoulder of ASTM D638 Type I geometry. The failure did not occur purely in the gage section. Therefore, the data for the coupons with the seam placement at the shoulder is invalid.

The stress concentration caused by the seams were eliminated by specifying random seam placement using Stratasys Insight Revision software. This function generated a tool path where

the seams were randomly placed on the contour of the geometry. Figure 70 below demonstrated randomly placed seams in the gripping region of the test geometry.

Figure 70. Randomly Placed Seams on Test Coupon. Stratasys Insight Revision software was used to specify random seam placement between each layer.

Figure 71 below demonstrated that the test coupons with the randomly placed seams have a higher ultimate tensile strength. Both sample populations were manufactured with default build parameters in the XYZ orientation. The randomly placed seam coupons have an ultimate tensile strength of 8170 psi and the default seam placement coupon have an ultimate tensile strength of 7940 psi. The variation between the two sample groups overlapped at the mean value. Therefore, a statistical test of two means was performed to identify whether the two means were significantly different. The test demonstrated that the two means were significantly different with a 95% confidence level. This data recommends that the seams should be randomly placed throughout the additive manufactured parts to improve the mechanical properties. Additionally, the user may be able to strategically place the seams outside of the stress zone to maximize the strength of the component.

Figure 71. Seam Placement UTS Comparison Graph. The default seam placement created a stress concentration at the necking region. This stress concentration reduced the average mechanical strength by 230 psi.

4.4 Delamination Due to Insufficient Raster Fill

The data for the contour depth suggested that thicker contour geometries have a higher ultimate tensile strength. However, the contour depth should not be specified to where there is insufficient clearance to deposit a raster fill. The lack of raster fill created a part that is significantly weaker in the transverse direction of the applied load because of poor layer adhesion as seen in Figure 72.

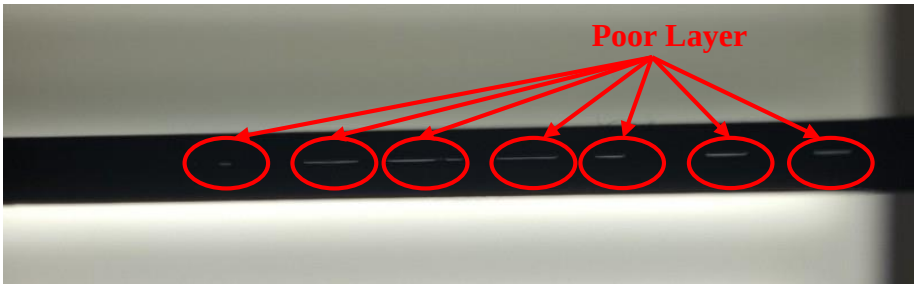

Figure 72. Poor Layer Adhesion on Test Coupons. The lack of raster fill between the contour resulted in poor layer adhesion. The air gaps was observed when the sample was held up to the light.

Figure 73 and Figure 74 shows specimen N1 with a build parameter of three contours and a 0.020 in. contour thickness. Inlayer delamination between the contours occurred when the specimen failed. The contour separation was exaggerated to show that the contours did not bond properly without a raster fill. The gage section has the poorest layer adhesion because the material was deposited as individual bead next to each other. While, the gripping region is formed by stacking rectangular contours.

Figure 73. Front View of Coupon with 3 Contours Failure. Delamination occurred due to the lack of raster fill in the gage section.

Figure 74. Top View of Coupon with 3 Contours Failure. The delamination in the gage section became more noticeable after the sample failed. The force shockwave at the failure separated the two contour. The delamination was exaggerated for graphical purposes.

Similarly, inlayer delamination also occurred with test geometries using two contours and a 0.030 in. contour thickness. These test geometries gage section completely delaminate and broke at both ends as shown in Figure 75 and Figure 76. The multiple failure locations was the result of a sudden release of energy when the specimen failed. At the point of failure, the strain of the material rapidly decreased causing a force wave to propagate along the gage section. The propagating force wave separated the two contours along the thickness plane. The delaminated sheet of ULTEM 9085 is not able to withstand the force when the wave reaches the shoulder of the gage section. Thus, two failures were observed at both ends of the gage section.

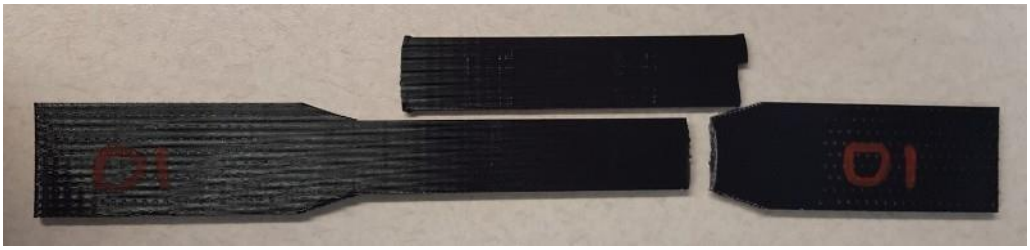

Figure 75. Front View of Coupon with 2 Contours and a Contour Thickness of 0.030 in. Failure. The force shockwave from the sudden failure propagated up the gage section and completely delaminated the contour in the gage section. The gage section has two contour deposited side by side without a raster fill.

Figure 76. Top View of Coupon with 2 Contours and a Contour Thickness of 0.030 in. Failure. The force shockwave from the sudden failure propagated up the gage section and completely delaminated the contour in the gage section. The gage section has two contour deposited side by side without a raster fill.

The contour depth should be maximized to obtain the best mechanical strength. The interior of the geometry should have enough clearance to support a raster fill to maximize inlayer adhesion between the material beads. Figure 77 below demonstrates the relationship between the part thickness, contour depth, and raster thickness in the XY build plane. The green rectangles represent the contour of the geometry and the gray rectangle represents the clearance between the contours.

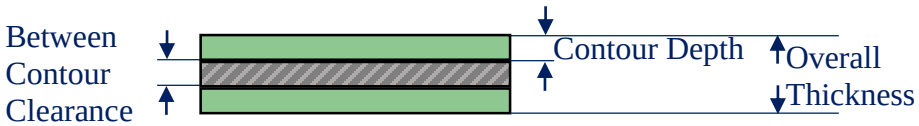

Figure 77. Contour Depth and Raster Fill Best Practice Schematic. The contour thickness and raster thickness should be selected during the design phase to provide maximum strength and layer adhesion. The relation between these two build parameter is dependent on the geometry.

Equation (13) below can be used as a criterion during the design process to ensure that there is sufficient clearance between the contours for a raster fill. The equation was developed by

subtracting the total contour depth from the overall part thickness to define the between contour clearance. The clearance between the contours has to be greater than the specified raster thickness for an interior raster fill to exist.

$$T - 2CD \geq RT \tag{13}$$

The variables are defined as T is the overall thickness of the part, CD is the contour depth, and RT is the raster thickness.

4.5 Cantilever Beam Effect on Tall Aspect Ratio Geometry

The standard ASTM D638 Type I geometry samples were not successfully printed in the ZXY orientation. Figure 78 below shows that delamination occurred during the printing process. The back two samples had stray strands of ULTEM 9085 filament that did not adhere correctly to the upper gripping region of the coupon. The two specimens in the middle of the front fell over after failing to adhere to the build plate. The two specimens on the front right started to develop poor surface finishes toward the top of the geometry. These manufacturing defects were caused by the cantilever beam effect due to the tall aspect ratio. The cantilever beam effect occurred during the raster fill portion of the layer construction. The oscillation of the extruding nozzle added a cyclic lateral force to the tall specimen. The compliant material vibrated in synchronize with the motion of the nozzle. This vibration caused the poor surface finish toward the upper grips and knocked over two specimens.

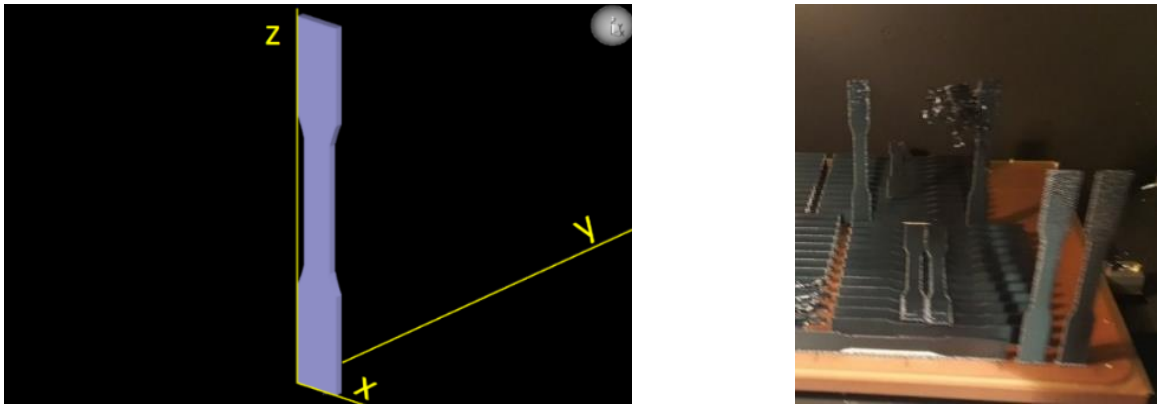

Figure 78. ASTM D638 Type I Build Orientation ZXY Failed Print. The failed printed was caused by the tall aspect ratio of the geometry. The cantilever beam effect caused the specimen to oscillate. The vibration prevented the layers from being deposit correctly.

The ASTM D638 Type I geometry did not show signs of the cantilever beam effect until the middle of the top gripping region. Therefore, it is recommended that the height of the specimen should not exceed 4.75 in. for a base ratio (length by width) of 0.75 in. by 0.125 in. The cantilever beam will not be an issue if the thickness to height ratio is greater 0.0263 and the width to height ratio is greater than 0.1579. Additionally, support material can be added increase the aspect ratio to the correct range. These relationships are expressed in Equation (14) and Equation (15) where a is the width, b is the thickness, and h is the height of the geometry.

$$\frac{a}{h} > 0.1579 \tag{14}$$

$$\frac{b}{h} > 0.0263 \tag{15}$$

If the aspect ratios meet both of the requirements outlined in Equation (14) and Equation (15), then the cantilever beam effect should not cause the print to fail. This conclusion was made with the assumptions that the cross-sectional area of the geometry was rectangular and that the raster angle was 45º/-45º.

4.6 Build Parameters Interactions

4.6.1 Following is a brief discussion of the different interactions between the different build parameters. The study is not fully conclusive. However, it is starting point to further the understanding of the material properties for ULTEM 9085.

4.6.2 Contour Thickness and Raster Thickness

The increase in contour thickness did not increase the mass of the coupon as shown by the red squares in Figure 50. As the contour thickness increased, the percentage of raster depth decreased to maintain the correct overall dimension of the test geometry. The raster depth is defined as the overall depth of the raster portion of the test coupon. The reduction of the raster depth is also shown in Figure 50. The red squares demonstrated that the overall thickness varied from 0.1264 in. – 0.1273 in. for contour thicknesses of 0.018 in. – 0.030 in. respectively. The increase in thickness without an increase in mass means that the raster depth had to be reduced to maintain a constant mass and a relatively constant overall test coupon thickness.

4.6.3 Contour Thickness and Raster Thickness

The contour dominant build parameters (contour thickness and number of contours) have a significantly higher impact on the mechanical strengths of the test specimens manufactured with build orientation XZY. These coupons have a larger number of layers with the contours parallel to the direction of the load applied. The blue lines in Figure 79 represent the contours of each of the layers. The ratio of contour depth to raster depth is significantly higher in orientation XZY.

The raster dominant build parameters (raster thickness and raster angle) have a greater influence on the ultimate tensile stress for the coupons manufactured with orientation XYZ. The raster depth to contour depth ratio is much larger in orientation XYZ. This orientation is called the

"minimum z" build orientation. The lower number of layers also minimizes the effect that the contours have on the mechanical properties of the coupon. The blue lines in Figure 80 represent the contours of each layer in the orientation XYZ.

The ultimate tensile strength in the orientation ZXY is determined by the strength of the polymer entanglement between the layers. In other words, the coupons manufactured in orientation ZXY tests the force required to delaminate the layers. The load is applied in the direction that the coupon is manufactured, where the applied load is perpendicular to the contours. The blue lines in Figure 81 represent the contours of each layer for orientation ZXY. Further investigation is needed to fully understand the effects of the different build parameters on the layer bond quality.

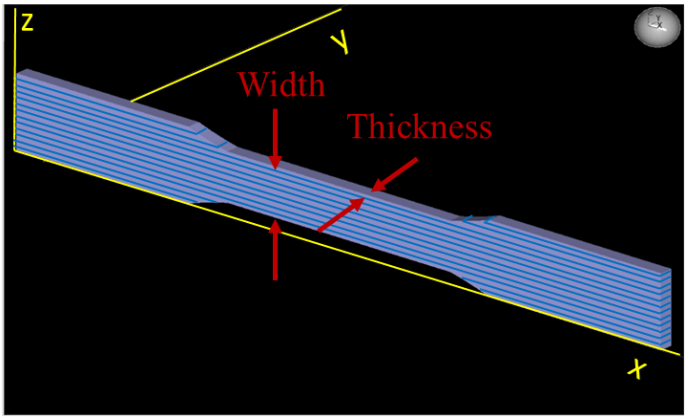

Figure 79. Orientation XZY Layers. The blue lines represents the contours of each layer in the orientation XZY.

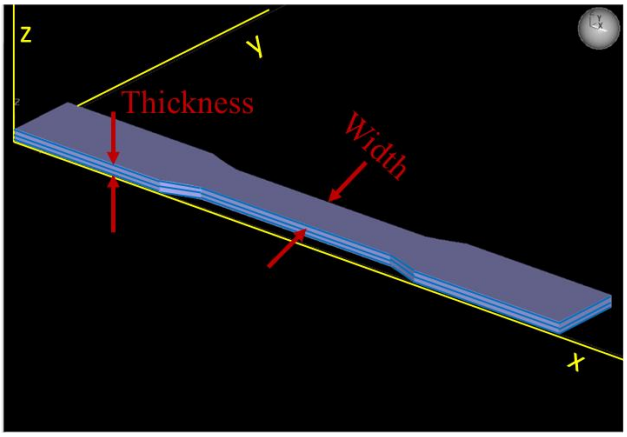

Figure 80. Orientation XYZ Layers. The blue lines represents the contours of each layer in the orientation XYZ.

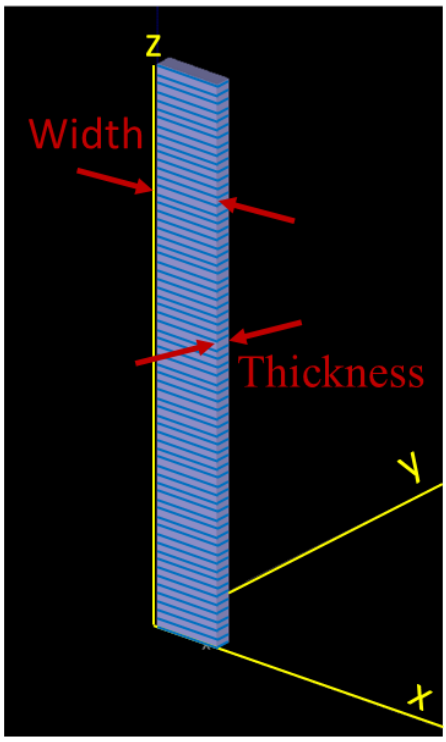

Figure 81. Orientation ZXY Layers. The blue lines represents the contours of each layer in the orientation ZXY.

Chapter 5 Recommendations and Conclusions

5.1 Summary of Results

This investigation was conducted to characterize the static tensile and fatigue properties for ULTEM 9085. All specimens were manufactured in accordance with ASTM D638 Type I geometry. The test coupons were labeled, weighed, and measured after manufacturing. Before each test, the coupons were pre-conditioned in standard laboratory conditions for 40 hours. The pre-conditioning procedures were developed in accordance with ASTM D618. The ambient conditions were recorded during each test to maintain compliance with ASTM standards.

The tensile mechanical properties tests were conducted on 15 different sample populations. Each population consisted of 5 samples. Only one build parameter was varied between each sample set. The other build parameters remained at the default setting. All coupons are manufactured in XZY orientation except for the specimens used in the various build orientation tensile tests.

Three different build orientations were tested and compared to the material specification sheet provided by Stratasys (OEM). The ultimate tensile strengths for XYZ orientation, XZY orientation, and ZXY orientation were 8170 psi, 9950 psi, and 6100 psi respectively. The ultimate tensile stresses compared very well with the specification sheet. The largest deviation between the gathered data and the specification sheet was 11% from the results for the ZXY orientation data.

The contour thickness, number of contours, and raster thickness all have a positive linear relationship between the build parameters and the ultimate tensile strength. The coupon with the thickest contour of 0.030 in. produced an ultimate tensile strength of 11600 psi. The thickest

coupons with a contour raster of 0.030 in have a 12% ultimate tensile strength increase over the thinnest coupons with a contour thickness of 0.018 in. at 10400 psi. Similarly, the coupons with the thickest raster of 0.030 in. produced an ultimate tensile strength of 11000 psi. The UTS for the decreasing raster thicknesses were 10500 psi and 10200 psi respectively. The contour depth verification tests confirmed that the ultimate tensile strength remained constant when the contour depth remained constant. The contour depth is the product of the number of contours and the contour thickness. The raster angle of $30^{o}/-60^{o}$ produced the highest ultimate tensile strength of 10300 psi. The UTS for raster angles $45^{o}/-45^{o}$ and $15^{o}/-75^{o}$ followed behind with UTS values of 10100 psi and 9360 psi respectively. The mass analysis demonstrated that a linear trend existed between the mass of the coupons with varying raster angle and ultimate tensile strength. The raster angle $15^{o}/-75^{o}$ produced the lowest UTS because the average mass of the coupons were only 10.28 g. While, the coupons with the raster angle $30^{o}/-60^{o}$ have the highest mass of 10.45 g.

The next segment of the investigation was conducted to characterize the fatigue life of additive manufactured ULTEM 9085. All specimen for the fatigue tests were manufactured in accordance to ASTM D638 except for the fully reversed fatigue tests. The coupon geometry had to be shortened due to buckling issues during the compression loading. The test frequency for all tests was kept constant at 5 Hz and 3 coupons were used per varying test conditions to ensure repeatability.

The standard tension-tension test produced results that matched previous data generated by others. The average cycles were 384, 1923, 24998, 91822 cycles with respect to stress levels of 80% UTS, 60% UTS, 30% UTS, and 20 % UTS. Next, the raster thickness and contour thickness were increased to 0.030 in. for two different sample population. Only one build parameter was varied per population. The thicker contour exhibited a 103% increase over the default build

parameter coupons at a stress level of 80% UTS. As the stress levels decreased, the differences between the fatigue lives of the coupons with the increased contour thickness and the coupons with default build parameter approached zero. The coupon with the increased raster thickness demonstrated lower fatigue life at the lower stress levels because there were less raster passes. The fully reversed tested concluded that the modified Goodman approached was an extremely conservative approach for additive manufactured ULTEM 9085. Thus, an Effective Tensile model was developed to better correlate the different R-Ratio and the equivalent stresses. The ETM was validated with fully reversed data at the 25% UTS, 20% UTS, 15% UTS, and 10% UTS stress levels.

5.2 Manufacturing Best Practices

The investigation revealed many manufacturing key learnings that were exposed by the gathered data and failed prints. The seam placements have a significant effect on the mechanical properties of the part. The seams created a stress concentration when they were placed at the same coordinates between each layer on the part. Therefore, the seams should be randomly placed throughout the geometry. The raster fill contributed greatly to the bond quality between the contours of each layer. The data suggested that the thickest contour depth produced the highest ultimate tensile strength. However, the data is bias because the loading pattern on a real part is much more complex. On the test specimen, the load was applied parallel to the direction of the contour. The contour was constructed with a continuous filament, which has the closest mechanical properties to the bulk material. The raster fill provided additional strength to the part for non-axial loads. The part should be manufactured with the thickest contour depth, while maintaining a raster fill. The aspect ratio of a part can also affect the success of the build. The force of the nozzle caused tall aspect ratio parts to oscillate as the nozzle was filling in the raster.

This oscillation prevented the layers from bonding correctly, which led to failed prints. Support material or well design aspect ratio should be utilized to ensure a successful print.

5.3 Future Research Opportunities

The research conducted provided great insight into the additive manufacturing process and the material ULTEM 9085. As AM technologies are becoming widely adopted, the applications are becoming increasingly demanding. Thus, further research is needed to advance the capabilities of extrusion additive manufacturing technologies.

This investigation only characterized the material properties of a single thermoplastic ULTEM 9085. As the demands for stronger components rise, further material research is needed. One area of interest is using fiber-reinforced filaments to improve the mechanical properties of the material. Previous studies have concluded that combining carbon fiber with thermoplastic filaments can increase the mechanical strength by 20%.[19] Additionally, cutting edge technologies from the industry is demonstrating that continuous carbon fiber filament can be used to reinforce the part. This concept is similar to using rebar in concrete. Research is needed to understand how to optimize the build process as well as characterized the material properties of these composite materials.

The data from this experiment is only valid for parts that are manufactured in a single piece of ULTEM 9085. The build volume is restricted by size of the machine. Many organizations are interested in printing parts that are larger than the current capabilities of the available machines. Therefore, further research is needed to develop new bonding techniques for extrusion additive manufacturing materials. The joint and bonding methods need to be characterized the ensure that the parts are able to be used as end-use products.

Extensive research has been conducted on the effects of build parameters on the static properties of ULTEM 9085. Therefore, the fatigue data for ULTEM 9085 should be further develop with future research. Currently, the fatigue characteristics for two different build parameters were characterized in this investigation. Prospective research can incorporate different raster angles, air gaps, build orientations, etc. to further investigate the effects that build parameters have on the fatigue life of ULTEM 9085.

Lastly, the Effective Tensile model needs to be further developed and validated. The model only correlated the equivalent stress between two R-Ratios (R = -1.0 and R = 0.1) in this investigation. Different R-Ratios need to be tested to ensure the validity of the ETM. If the model is proven, a correlation factor can be developed to use the model between different extrusion additive manufactured materials.

Chapter 6 Appendix

List of Figures

List of Tables

Appendix A: Naming Convention Key

Table A-1. Test Codes Used to Label Testing Coupons

Naming Convention Key		
Test Code	**Test Description**	**Test Type**
A	Standard Build XYZ (User Seam Placement)	Static
A.1	Standard Build XYZ (Random Seam Placement)	Static
B	Standard Build XZY	Static
E	Raster Angle: 15º/-75º	Static
F	Raster Angle: 30º/-60º	Static
G	Raster Thickness: 0.018 in.	Static
H	Raster Thickness: 0.024 in.	Static
I	Raster Thickness: 0.030 in.	Static
J	Contour Thickness: 0.018 in.	Static
K	Contour Thickness: 0.024 in.	Static
L	Contour Thickness: 0.030 in.	Static
M	Number of Contour: 2	Static
N	Number of Contour: 3	Static
O	Contour Thickness: 0.03 in.; Number of Contours: 2	Static
Q	Tension-Tension Fatigue at 80% UTS	Fatigue
R	Tension-Tension Fatigue at 60% UTS	Fatigue
Y.1	Contour Thickness: 0.030 in. at 20% UTS	Fatigue
Z	Contour Thickness: 0.030 in. at 80% UTS	Fatigue
AA	Contour Thickness: 0.030 in. at 60% UTS	Fatigue
GG	Raster Thickness: 0.030 in. at 30% UTS	Fatigue
HH	Raster Thickness: 0.030 in. at 20% UTS	Fatigue
NN	Tension-Tension Fatigue at 30% UTS	Fatigue
OO	Tension-Tension Fatigue at 20% UTS	Fatigue
PP	Tension-Tension Fatigue at 10% UTS	Fatigue
QQ	Fully Reversed Fatigue at 16% UTS	Fatigue
RR	Fully Reversed Fatigue at 10% UTS	Fatigue
TT	Orientation XZY: Low Stress < 250 PSI	Fatigue
VV	Fully Reversed Fatigue at 20% UTS	Fatigue
WW	Fully Reversed Fatigue at 25% UTS	Fatigue
XX	Fully Reversed Fatigue at 10% UTS	Fatigue

Appendix B: Pre-testing Physical Properties Verification

Table B-1. Physical Properties for Static Test Coupons

Static Coupons Pre-test Physical Properties Verification						
Test Description	**Test Sample ID Code**	**Date Measured**	**WC [in]**	**T [in]**	**Cross Sectional Area [in^2]**	**Mass [g]**
Standard Build XYZ (Optimized Seam Placement)	A1	1/10/2017	0.5015	0.1380	0.0692	N/A
Standard Build XYZ (Optimized Seam Placement)	A2	1/10/2017	0.5020	0.1385	0.0695	N/A
Standard Build XYZ (Optimized Seam Placement)	A3	1/10/2017	0.5020	0.1380	0.0693	N/A
Standard Build XYZ (Optimized Seam Placement)	A4	1/10/2017	0.5030	0.1375	0.0692	N/A
Standard Build XYZ (Optimized Seam Placement)	A5	1/10/2017	0.4995	0.1380	0.0689	N/A
Standard Build XYZ (Random Seam Placement)	A1.1	1/10/2017	0.5012	0.1380	0.0692	N/A
Standard Build XYZ (Random Seam Placement)	A2.1	1/10/2017	0.5005	0.1385	0.0693	N/A
Standard Build XYZ (Random Seam Placement)	A3.1	1/10/2017	0.5000	0.1380	0.0690	N/A
Standard Build XYZ (Random Seam Placement)	A4.1	1/10/2017	0.5000	0.1380	0.0690	N/A
Standard Build XYZ (Random Seam Placement)	A5.1	1/10/2017	0.5000	0.1375	0.0688	N/A
Standard Build XZY	B1	12/14/2016	0.5000	0.1375	0.0688	10.3600
Standard Build XZY	B2	12/14/2016	0.5000	0.1380	0.0690	10.3600
Standard Build XZY	B3	12/14/2016	0.5000	0.1380	0.0690	10.3600
Standard Build XZY	B4	12/14/2016	0.5000	0.1375	0.0688	10.3600
Standard Build XZY	B5	12/14/2016	0.5000	0.1380	0.0690	10.3600
Standard Build XZY	B6	12/14/2016	0.5000	0.1380	0.0690	10.3600
Standard Build XZY	B7	3/12/2017	0.5140	0.1260	0.0648	10.3900
Standard Build XZY	B8	3/12/2017	0.5135	0.1265	0.0650	10.3600
Standard Build XZY	B9	3/12/2017	0.5135	0.1270	0.0652	10.3800
Standard Build XZY	B10	3/12/2017	0.5130	0.1265	0.0649	10.3900
Standard Build XZY	B11	3/12/2017	0.5135	0.1260	0.0647	10.3400
Standard Build XZY	B12	3/12/2017	0.5140	0.1265	0.0650	10.3200
Standard Build XZY	B13	3/12/2017	0.5140	0.1265	0.0650	10.3800

Table B-2. Physical Properties for Static Test Coupons

Static Coupons Pre-test Physical Properties Verification						
Test Description	**Test Sample ID Code**	**Date Measured**	**WC [in]**	**T [in]**	**Cross Sectional Area [in^2]**	**Mass [g]**
Raster Angle: 15º/-75º	E1	3/12/2017	0.5150	0.1275	0.0657	10.2800
Raster Angle: 15º/-75º	E2	3/12/2017	0.5160	0.1270	0.0655	10.2600
Raster Angle: 15º/-75º	E3	3/12/2017	0.5160	0.1260	0.0650	10.2600
Raster Angle: 15º/-75º	E4	3/12/2017	0.5165	0.1270	0.0656	10.2600
Raster Angle: 15º/-75º	E5	3/12/2017	0.5145	0.1270	0.0653	10.3000
Raster Angle: 15º/-75º	E6	3/12/2017	0.5165	0.1265	0.0653	10.3000
Raster Angle: 15º/-75º	E7	3/12/2017	0.5160	0.1270	0.0655	10.2900
Raster Angle: 30º/-60º	F1	3/12/2017	0.5155	0.1270	0.0655	10.4300
Raster Angle: 30º/-60º	F2	3/12/2017	0.5155	0.1270	0.0655	10.4600
Raster Angle: 30º/-60º	F3	3/12/2017	0.5160	0.1270	0.0655	10.4200
Raster Angle: 30º/-60º	F4	3/12/2017	0.5165	0.1270	0.0656	10.4700
Raster Angle: 30º/-60º	F5	3/12/2017	0.5165	0.1275	0.0659	10.4500
Raster Angle: 30º/-60º	F6	3/12/2017	0.5140	0.1265	0.0650	10.4500
Raster Angle: 30º/-60º	F7	3/12/2017	0.5155	0.1265	0.0652	10.4700
Raster Thickness: 0.018 in.	G1	3/12/2017	0.5125	0.1265	0.0648	10.3400
Raster Thickness: 0.018 in.	G2	3/12/2017	0.5125	0.1260	0.0646	10.3400
Raster Thickness: 0.018 in.	G3	3/12/2017	0.5130	0.1260	0.0646	10.3000
Raster Thickness: 0.018 in.	G4	3/12/2017	0.5130	0.1265	0.0649	10.3500
Raster Thickness: 0.018 in.	G5	3/12/2017	0.5130	0.1260	0.0646	10.3100
Raster Thickness: 0.018 in.	G6	3/12/2017	0.5120	0.1260	0.0645	10.3500
Raster Thickness: 0.018 in.	G7	3/12/2017	0.5120	0.1260	0.0645	10.3300
Raster Thickness: 0.024 in.	H1	3/12/2017	0.5130	0.1275	0.0654	10.4200
Raster Thickness: 0.024 in.	H2	3/12/2017	0.5155	0.1265	0.0652	10.4200
Raster Thickness: 0.024 in.	H3	3/12/2017	0.5140	0.1270	0.0653	10.4600
Raster Thickness: 0.024 in.	H4	3/12/2017	0.5145	0.1270	0.0653	10.4200
Raster Thickness: 0.024 in.	H5	3/12/2017	0.5130	0.1265	0.0649	10.4200
Raster Thickness: 0.024 in.	H6	3/12/2017	0.5135	0.1275	0.0655	10.4200
Raster Thickness: 0.024 in.	H7	3/12/2017	0.5140	0.1265	0.0650	10.4200

Table B-3. Physical Properties for Static Test Coupons

Static Coupons Pre-test Physical Properties Verification						
Test Description	**Test Sample ID Code**	**Date Measured**	**WC [in.]**	**T [in.]**	**Cross Sectional Area [in.^2]**	**Mass [g]**
Raster Thickness: 0.030 in.	I1	3/12/2017	0.5150	0.1270	0.0654	10.6500
Raster Thickness: 0.030 in.	I2	3/12/2017	0.5145	0.1265	0.0651	10.5800
Raster Thickness: 0.030 in.	I3	3/12/2017	0.5140	0.1260	0.0648	10.5900
Raster Thickness: 0.030 in.	I4	3/12/2017	0.5165	0.1270	0.0656	10.5400
Raster Thickness: 0.030 in.	I5	3/12/2017	0.5160	0.1270	0.0655	10.5700
Raster Thickness: 0.030 in.	I6	3/12/2017	0.5155	0.1265	0.0652	10.5600
Raster Thickness: 0.030 in.	I7	3/12/2017	0.5155	0.1270	0.0655	10.6000
Contour Thickness: 0.018 in.	J1	2/4/2017	0.5127	0.1270	0.0651	10.4800
Contour Thickness: 0.018 in.	J2	2/4/2017	0.5123	0.1260	0.0645	10.4800
Contour Thickness: 0.018 in.	J3	2/4/2017	0.5128	0.1275	0.0654	10.4800
Contour Thickness: 0.018 in.	J4	2/4/2017	0.5123	0.1260	0.0645	10.4800
Contour Thickness: 0.018 in.	J5	2/4/2017	0.5120	0.1260	0.0645	10.4800
Contour Thickness: 0.018 in.	J6	2/4/2017	0.5118	0.1265	0.0647	10.4800
Contour Thickness: 0.018 in.	J7	2/4/2017	0.5120	0.1260	0.0645	10.4800
Contour Thickness: 0.024 in.	K1	2/4/2017	0.5120	0.1270	0.0650	10.4000
Contour Thickness: 0.024 in.	K2	2/4/2017	0.5130	0.1265	0.0649	10.4000
Contour Thickness: 0.024 in.	K3	2/4/2017	0.5120	0.1270	0.0650	10.4000
Contour Thickness: 0.024 in.	K4	2/4/2017	0.5125	0.1270	0.0651	10.4000
Contour Thickness: 0.024 in.	K5	2/4/2017	0.5125	0.1270	0.0651	10.4000
Contour Thickness: 0.024 in.	K6	2/4/2017	0.5130	0.1270	0.0652	10.4000
Contour Thickness: 0.024 in.	K7	2/4/2017	0.5105	0.1275	0.0651	10.4000

Table B-4. Physical Properties for Static Test Coupons

Static Coupons Pre-test Physical Properties Verification						
Test Description	**Test Sample ID Code**	**Date Measured**	**WC [in.]**	**T [in.]**	**Cross Sectional Area [in.^2]**	**Mass [g]**
Contour Thickness: 0.030 in.	L1	2/4/2017	0.5150	0.1275	0.0657	10.4200
Contour Thickness: 0.030 in.	L2	2/4/2017	0.5150	0.1280	0.0659	10.4200
Contour Thickness: 0.030 in.	L3	2/4/2017	0.5185	0.1260	0.0653	10.4200
Contour Thickness: 0.030 in.	L4	2/4/2017	0.5155	0.1270	0.0655	10.4200
Contour Thickness: 0.030 in.	L5	2/4/2017	0.5145	0.1285	0.0661	10.4200
Contour Thickness: 0.030 in.	L6	2/4/2017	0.5115	0.1270	0.0650	10.4200
Contour Thickness: 0.030 in.	L7	2/4/2017	0.5120	0.1270	0.0650	10.4200
Number of Contour: 2	M1	2/4/2017	0.5115	0.1265	0.0647	10.2900
Number of Contour: 2	M2	2/4/2017	0.5115	0.1275	0.0652	10.2900
Number of Contour: 2	M3	2/4/2017	0.5150	0.1265	0.0651	10.2900
Number of Contour: 2	M4	2/4/2017	0.5110	0.1275	0.0652	10.2900
Number of Contour: 2	M5	2/4/2017	0.5110	0.1265	0.0646	10.2900
Number of Contour: 2	M6	2/4/2017	0.5110	0.1275	0.0652	10.2900
Number of Contour: 2	M7	2/4/2017	0.5125	0.1270	0.0651	10.2900
Number of Contour: 3	N1	2/4/2017	0.5100	0.1275	0.0650	10.0500
Number of Contour: 3	N2	2/4/2017	0.5095	0.1275	0.0650	10.0500
Number of Contour: 3	N3	2/4/2017	0.5075	0.1275	0.0647	10.0500
Number of Contour: 3	N4	2/4/2017	0.5095	0.1285	0.0655	10.0500
Number of Contour: 3	N5	2/4/2017	0.5085	0.1275	0.0648	10.0500
Number of Contour: 3	N6	2/4/2017	0.5080	0.1285	0.0653	10.0500
Number of Contour: 3	N7	2/4/2017	0.5070	0.1270	0.0644	10.0500
Number of Contour: 3	N8	2/4/2017	0.5065	0.1270	0.0643	10.0500
Contour Thickness: 0.03 in.; Number of Contours: 2	O1	2/4/2017	0.5090	0.1270	0.0646	10.1200
Contour Thickness: 0.03 in.; Number of Contours: 2	O2	2/4/2017	0.5085	0.1280	0.0651	10.1200
Contour Thickness: 0.03 in.; Number of Contours: 2	O3	2/4/2017	0.5085	0.1280	0.0651	10.1200
Contour Thickness: 0.03 in.; Number of Contours: 2	O4	2/4/2017	0.5085	0.1270	0.0646	10.1200
Contour Thickness: 0.03 in.; Number of Contours: 2	O5	2/4/2017	0.5100	0.1280	0.0653	10.1200
Contour Thickness: 0.03 in.; Number of Contours: 2	O6	2/4/2017	0.5190	0.1270	0.0659	10.1200
Contour Thickness: 0.03 in.; Number of Contours: 2	O7	2/4/2017	0.5100	0.1275	0.0650	10.1200

Table B-5. Physical Properties for Fatigue Test Coupons

Fatigue Coupons Pre-test Physical Properties Verification							
Test Type	**Test Description**	**Test Sample ID Code**	**Date Measured**	**WC [in.]**	**T [in.]**	**Cross Sectional Area [in^2]**	**Mass [g]**
Fatigue	Tension-Tension Fatigue at 80% UTS	Q1	2/2/2017	0.5140	0.1272	0.0654	10.290
Fatigue	Tension-Tension Fatigue at 80% UTS	Q2	2/2/2017	0.5145	0.1260	0.0648	10.290
Fatigue	Tension-Tension Fatigue at 80% UTS	Q3	2/2/2017	0.5155	0.1278	0.0659	10.290
Fatigue	Tension-Tension Fatigue at 60% UTS	R1	2/2/2017	0.5137	0.1262	0.0648	10.270
Fatigue	Tension-Tension Fatigue at 60% UTS	R2	2/2/2017	0.5127	0.1260	0.0646	10.270
Fatigue	Tension-Tension Fatigue at 60% UTS	R3	2/2/2017	0.5137	0.1268	0.0651	10.270
Fatigue	Contour Thickness: 0.030 in. at 20% UTS	Y1.1	6/15/2017	0.5120	0.1275	0.0653	10.490
Fatigue	Contour Thickness: 0.030 in. at 20% UTS	Y2.1	6/15/2017	0.5120	0.1280	0.0655	10.480
Fatigue	Contour Thickness: 0.030 in. at 20% UTS	Y3.1	6/15/2017	0.5120	0.1280	0.0655	10.490
Fatigue	Contour Thickness: 0.030 in. at 80% UTS	Z1	3/12/2017	0.5155	0.1260	0.0650	10.510
Fatigue	Contour Thickness: 0.030 in. at 80% UTS	Z2	3/12/2017	0.5140	0.1270	0.0653	10.450
Fatigue	Contour Thickness: 0.030 in. at 80% UTS	Z3	3/12/2017	0.5145	0.1265	0.0651	10.450
Fatigue	Contour Thickness: 0.030 in. at 60% UTS	AA1	3/12/2017	0.5155	0.1265	0.0652	10.460
Fatigue	Contour Thickness: 0.030 in. at 60% UTS	AA2	3/12/2017	0.5155	0.1265	0.0652	10.460
Fatigue	Contour Thickness: 0.030 in. at 60% UTS	AA3	3/12/2017	0.5155	0.1265	0.0652	10.460
Fatigue	Contour Thickness: 0.030 in. at 30% UTS	BB1	3/12/2017	0.5150	0.1265	0.0651	10.470
Fatigue	Contour Thickness: 0.030 in. at 30% UTS	BB2	3/12/2017	0.5155	0.1260	0.0650	10.530
Fatigue	Contour Thickness: 0.030 in. at 30% UTS	BB3	3/12/2017	0.5155	0.1270	0.0655	10.480
Fatigue	Raster Thickness: 0.030 in. at 30% UTS	GG1	3/12/2017	0.5175	0.1265	0.0655	10.500
Fatigue	Raster Thickness: 0.030 in. at 30% UTS	GG2	3/12/2017	0.5180	0.1265	0.0655	10.520
Fatigue	Raster Thickness: 0.030 in. at 30% UTS	GG3	3/12/2017	0.5180	0.1270	0.0658	10.520
Fatigue	Raster Thickness: 0.030 in. at 20% UTS	HH1	3/12/2017	0.5190	0.1270	0.0659	10.510
Fatigue	Raster Thickness: 0.030 in. at 20% UTS	HH2	3/12/2017	0.5175	0.1270	0.0657	10.500
Fatigue	Raster Thickness: 0.030 in. at 20% UTS	HH3	3/12/2017	0.5195	0.1265	0.0657	10.510

Table B-6. Physical Properties for Fatigue Test Coupons

Fatigue Coupons Pre-test Physical Properties Verification							
Test Type	**Test Description**	**Test Sample ID Code**	**Date Measured**	**WC [in.]**	**T [in.]**	**Cross Sectional Area [in^2]**	**Mass [g]**
Fatigue	Raster Thickness: 0.030 in. at 60% UTS	II1	3/12/2017	0.5170	0.1270	0.0657	10.520
Fatigue	Raster Thickness: 0.030 in. at 60% UTS	II2	3/12/2017	0.5175	0.1275	0.0660	10.510
Fatigue	Raster Thickness: 0.030 in. at 60% UTS	II3	3/12/2017	0.5170	0.1265	0.0654	10.540
Fatigue	Raster Thickness: 0.030 in. at 80% UTS	JJ1	3/12/2017	0.5170	0.1270	0.0657	10.580
Fatigue	Raster Thickness: 0.030 in. at 80% UTS	JJ2	3/12/2017	0.5155	0.1270	0.0655	10.520
Fatigue	Raster Thickness: 0.030 in. at 80% UTS	JJ3	3/12/2017	0.5180	0.1265	0.0655	10.490
Fatigue	Tension-Tension Fatigue at 30% UTS	NN1	5/15/2017	0.5125	0.1275	0.0653	10.340
Fatigue	Tension-Tension Fatigue at 30% UTS	NN2	5/15/2017	0.5125	0.1270	0.0651	10.350
Fatigue	Tension-Tension Fatigue at 30% UTS	NN3	5/15/2017	0.5130	0.1270	0.0652	10.340
Fatigue	Tension-Tension Fatigue at 20% UTS	OO1	5/15/2017	0.5125	0.1285	0.0659	10.360
Fatigue	Tension-Tension Fatigue at 20% UTS	OO2	5/15/2017	0.5140	0.1270	0.0653	10.370
Fatigue	Tension-Tension Fatigue at 20% UTS	OO3	5/15/2017	0.5135	0.1275	0.0655	10.340
Fatigue	Tension-Tension Fatigue at 10% UTS	PP1	5/15/2017	0.5140	0.1270	0.0653	10.350
Fatigue	Tension-Tension Fatigue at 10% UTS	PP2	5/15/2017	0.5130	0.1270	0.0652	10.340
Fatigue	Tension-Tension Fatigue at 10% UTS	PP3	5/15/2017	0.5130	0.1270	0.0652	10.340
Fatigue	Fully Reversed Fatigue at 16% UTS	QQ1	5/15/2017	0.5125	0.1275	0.0653	10.340
Fatigue	Fully Reversed Fatigue at 16% UTS	QQ2	5/15/2017	0.5135	0.1275	0.0655	10.340
Fatigue	Fully Reversed Fatigue at 16% UTS	QQ3	5/15/2017	0.5140	0.1270	0.0653	10.350
Fatigue	Fully Reversed Fatigue at 10% UTS	RR1	5/15/2017	0.5135	0.1270	0.0652	10.340
Fatigue	Fully Reversed Fatigue at 10% UTS	RR2	5/15/2017	0.5130	0.1275	0.0654	10.340
Fatigue	Fully Reversed Fatigue at 10% UTS	RR3	5/15/2017	0.5125	0.1275	0.0653	10.360
Fatigue	Orientation XZY: Low Stress < 250 PSI	TT1	5/15/2017	0.5110	0.1270	0.0649	10.340
Fatigue	Orientation XZY: Low Stress < 250 PSI	TT2	5/15/2017	0.5130	0.1270	0.0652	10.360
Fatigue	Orientation XZY: Low Stress < 250 PSI	TT3	5/15/2017	0.5130	0.1280	0.0657	10.330

Table B-7. Physical Properties for Fatigue Test Coupons

Fatigue Coupons Pre-test Physical Properties Verification							
Test Type	**Test Description**	**Test Sample ID Code**	**Date Measured**	**WC [in.]**	**T [in.]**	**Cross Sectional Area [in^2]**	**Mass [g]**
Fatigue	Fully Reversed Fatigue at 20% UTS	VV1	6/15/2017	0.5110	0.1270	0.0649	5.590
Fatigue	Fully Reversed Fatigue at 20% UTS	VV2	6/15/2017	0.5110	0.1275	0.0652	5.600
Fatigue	Fully Reversed Fatigue at 20% UTS	VV3	6/15/2017	0.5100	0.1275	0.0650	5.570
Fatigue	Fully Reversed Fatigue at 25% UTS	WW1	6/15/2017	0.5100	0.1270	0.0648	5.600
Fatigue	Fully Reversed Fatigue at 25% UTS	WW2	6/15/2017	0.5110	0.1275	0.0652	5.600
Fatigue	Fully Reversed Fatigue at 25% UTS	WW3	6/15/2017	0.5110	0.1275	0.0652	5.600
Fatigue	Fully Reversed Fatigue at 10% UTS	XX1	6/15/2017	0.5125	0.1270	0.0651	5.600
Fatigue	Fully Reversed Fatigue at 10% UTS	XX2	6/15/2017	0.5125	0.1280	0.0656	5.600
Fatigue	Fully Reversed Fatigue at 10% UTS	XX3	6/15/2017	0.5120	0.1280	0.0655	5.600

Appendix C: Pre-conditioning Data

Table C-1. Precondition Data for Static Test Coupons

Static Coupons Pre-conditioning Data						
Test Type	**Test Description**	**Test Sample ID Code**	**Duration [hr]**	**Date Conditioned**	**Temperature [ºC]**	**Relative Humidity [%]**
Static	Standard Build XYZ (Optimized Seam Placement)	A1	40	1/8/2017-1/10/2017	22	23
Static	Standard Build XYZ (Optimized Seam Placement)	A2	40	1/8/2017-1/10/2017	22	23
Static	Standard Build XYZ (Optimized Seam Placement)	A3	40	1/8/2017-1/10/2017	22	23
Static	Standard Build XYZ (Optimized Seam Placement)	A4	40	1/8/2017-1/10/2017	22	23
Static	Standard Build XYZ (Optimized Seam Placement)	A5	40	1/8/2017-1/10/2017	22	23
Static	Standard Build XYZ (Random Seam Placement)	A1.1	40	1/8/2017-1/10/2017	22	23
Static	Standard Build XYZ (Random Seam Placement)	A2.1	40	1/8/2017-1/10/2017	22	23
Static	Standard Build XYZ (Random Seam Placement)	A3.1	40	1/8/2017-1/10/2017	22	23
Static	Standard Build XYZ (Random Seam Placement)	A4.1	40	1/8/2017-1/10/2017	22	23
Static	Standard Build XYZ (Random Seam Placement)	A5.1	40	1/8/2017-1/10/2017	22	23
Static	Standard Build XZY	B1	40	12/12/2016-12/14/2016	23	31
Static	Standard Build XZY	B2	40	12/12/2016-12/14/2016	23	31
Static	Standard Build XZY	B3	40	12/12/2016-12/14/2016	23	31
Static	Standard Build XZY	B4	40	12/12/2016-12/14/2016	23	31
Static	Standard Build XZY	B5	40	12/12/2016-12/14/2016	23	31
Static	Standard Build XZY	B6	40	12/12/2016-12/14/2016	23	31
Static	Raster Angle: 15º/-75º	E1	40	3/21/2017-3/23/2017	23	21
Static	Raster Angle: 15º/-75º	E2	40	3/21/2017-3/23/2017	23	21
Static	Raster Angle: 15º/-75º	E3	40	3/21/2017-3/23/2017	23	21
Static	Raster Angle: 15º/-75º	E4	40	3/21/2017-3/23/2017	23	21
Static	Raster Angle: 15º/-75º	E5	40	3/21/2017-3/23/2017	23	21
Static	Raster Angle: 15º/-75º	E6	40	3/21/2017-3/23/2017	23	21
Static	Raster Angle: 15º/-75º	E7	40	3/21/2017-3/23/2017	23	21

Table C-2. Precondition Data for Static Test Coupons

Static Coupons Pre-conditioning Data						
Test Type	**Test Description**	**Test Sample ID Code**	**Duration [hr]**	**Date Conditioned**	**Temperature [ºC]**	**Relative Humidity [%]**
Static	Raster Angle: 30º/-60º	F1	40	3/21/2017-3/23/2017	23	21
Static	Raster Angle: 30º/-60º	F2	40	3/21/2017-3/23/2017	23	21
Static	Raster Angle: 30º/-60º	F3	40	3/21/2017-3/23/2017	23	21
Static	Raster Angle: 30º/-60º	F4	40	3/21/2017-3/23/2017	23	21
Static	Raster Angle: 30º/-60º	F5	40	3/21/2017-3/23/2017	23	21
Static	Raster Angle: 30º/-60º	F6	40	3/21/2017-3/23/2017	23	21
Static	Raster Angle: 30º/-60º	F7	40	3/21/2017-3/23/2017	23	21
Static	Raster Thickness: 0.018 in.	G1	40	3/21/2017-3/23/2017	23	21
Static	Raster Thickness: 0.018 in.	G2	40	3/21/2017-3/23/2017	23	21
Static	Raster Thickness: 0.018 in.	G3	40	3/21/2017-3/23/2017	23	21
Static	Raster Thickness: 0.018 in.	G4	40	3/21/2017-3/23/2017	23	21
Static	Raster Thickness: 0.018 in.	G5	40	3/21/2017-3/23/2017	23	21
Static	Raster Thickness: 0.018 in.	G6	40	3/21/2017-3/23/2017	23	21
Static	Raster Thickness: 0.018 in.	G7	40	3/21/2017-3/23/2017	23	21
Static	Raster Thickness: 0.024 in.	H1	40	3/21/2017-3/23/2017	23	21
Static	Raster Thickness: 0.024 in.	H2	40	3/21/2017-3/23/2017	23	21
Static	Raster Thickness: 0.024 in.	H3	40	3/21/2017-3/23/2017	23	21
Static	Raster Thickness: 0.024 in.	H4	40	3/21/2017-3/23/2017	23	21
Static	Raster Thickness: 0.024 in.	H5	40	3/21/2017-3/23/2017	23	21
Static	Raster Thickness: 0.024 in.	H6	40	3/21/2017-3/23/2017	23	21
Static	Raster Thickness: 0.024 in.	H7	40	3/21/2017-3/23/2017	23	21
Static	Raster Thickness: 0.030 in.	I1	40	3/21/2017-3/23/2017	23	21
Static	Raster Thickness: 0.030 in.	I2	40	3/21/2017-3/23/2017	23	21
Static	Raster Thickness: 0.030 in.	I3	40	3/21/2017-3/23/2017	23	21
Static	Raster Thickness: 0.030 in.	I4	40	3/21/2017-3/23/2017	23	21
Static	Raster Thickness: 0.030 in.	I5	40	3/21/2017-3/23/2017	23	21
Static	Raster Thickness: 0.030 in.	I6	40	3/21/2017-3/23/2017	23	21
Static	Raster Thickness: 0.030 in.	I7	40	3/21/2017-3/23/2017	23	21

Table C-3. Precondition Data for Static Test Coupons

Static Coupons Pre-conditioning Data						
Test Type	**Test Description**	**Test Sample ID Code**	**Duration [hr]**	**Date Conditioned**	**Temperature [ºC]**	**Relative Humidity [%]**
Static	Contour Thickness: 0.018 in.	J1	40	2/4/2017 -2/6/2017	21	23
Static	Contour Thickness: 0.018 in.	J2	40	2/4/2017 -2/6/2017	21	23
Static	Contour Thickness: 0.018 in.	J3	40	2/4/2017 -2/6/2017	21	23
Static	Contour Thickness: 0.018 in.	J4	40	2/4/2017 -2/6/2017	21	23
Static	Contour Thickness: 0.018 in.	J5	40	2/4/2017 -2/6/2017	21	23
Static	Contour Thickness: 0.018 in.	J6	40	2/4/2017 -2/6/2017	21	23
Static	Contour Thickness: 0.018 in.	J7	40	2/4/2017 -2/6/2017	21	23
Static	Contour Thickness: 0.024 in.	K1	40	2/4/2017 -2/6/2017	21	23
Static	Contour Thickness: 0.024 in.	K2	40	2/4/2017 -2/6/2017	21	23
Static	Contour Thickness: 0.024 in.	K3	40	2/4/2017 -2/6/2017	21	23
Static	Contour Thickness: 0.024 in.	K4	40	2/4/2017 -2/6/2017	21	23
Static	Contour Thickness: 0.024 in.	K5	40	2/4/2017 -2/6/2017	21	23
Static	Contour Thickness: 0.024 in.	K6	40	2/4/2017 -2/6/2017	21	23
Static	Contour Thickness: 0.024 in.	K7	40	2/4/2017 -2/6/2017	21	23
Static	Contour Thickness: 0.030 in.	L1	40	2/4/2017 -2/6/2017	21	23
Static	Contour Thickness: 0.030 in.	L2	40	2/4/2017 -2/6/2017	21	23
Static	Contour Thickness: 0.030 in.	L3	40	2/4/2017 -2/6/2017	21	23
Static	Contour Thickness: 0.030 in.	L4	40	2/4/2017 -2/6/2017	21	23
Static	Contour Thickness: 0.030 in.	L5	40	2/4/2017 -2/6/2017	21	23
Static	Contour Thickness: 0.030 in.	L6	40	2/4/2017 -2/6/2017	21	23
Static	Contour Thickness: 0.030 in.	L7	40	2/4/2017 -2/6/2017	21	23

Table C-4. Precondition Data for Static Test Coupons

Static Coupons Pre-conditioning Data						
Test Type	**Test Description**	**Test Sample ID Code**	**Duration [hr]**	**Date Conditioned**	**Temperature [ºC]**	**Relative Humidity [%]**
Static	Number of Contour: 2	M1	40	2/4/2017 -2/6/2017	21	23
Static	Number of Contour: 2	M2	40	2/4/2017 -2/6/2017	21	23
Static	Number of Contour: 2	M3	40	2/4/2017 -2/6/2017	21	23
Static	Number of Contour: 2	M4	40	2/4/2017 -2/6/2017	21	23
Static	Number of Contour: 2	M5	40	2/4/2017 -2/6/2017	21	23
Static	Number of Contour: 2	M6	40	2/4/2017 -2/6/2017	21	23
Static	Number of Contour: 2	M7	40	2/4/2017 -2/6/2017	21	23
Static	Number of Contour: 3	N1	40	2/4/2017 -2/6/2017	21	23
Static	Number of Contour: 3	N2	40	2/4/2017 -2/6/2017	21	23
Static	Number of Contour: 3	N3	40	2/4/2017 -2/6/2017	21	23
Static	Number of Contour: 3	N4	40	2/4/2017 -2/6/2017	21	23
Static	Number of Contour: 3	N5	40	2/4/2017 -2/6/2017	21	23
Static	Number of Contour: 3	N6	40	2/4/2017 -2/6/2017	21	23
Static	Number of Contour: 3	N7	40	2/4/2017 -2/6/2017	21	23
Static	Contour Thickness: 0.030 in.; Number of Contours: 2	O1	40	2/4/2017 -2/6/2017	21	23
Static	Contour Thickness: 0.030 in.; Number of Contours: 2	O2	40	2/4/2017 -2/6/2017	21	23
Static	Contour Thickness: 0.030 in.; Number of Contours: 2	O3	40	2/4/2017 -2/6/2017	21	23
Static	Contour Thickness: 0.030 in.; Number of Contours: 2	O4	40	2/4/2017 -2/6/2017	21	23
Static	Contour Thickness: 0.030 in.; Number of Contours: 2	O5	40	2/4/2017 -2/6/2017	21	23
Static	Contour Thickness: 0.030 in.; Number of Contours: 2	O6	40	2/4/2017 -2/6/2017	21	23
Static	Contour Thickness: 0.030 in.; Number of Contours: 2	O7	40	2/4/2017 -2/6/2017	21	23

Table C-5. Precondition Data for Static Test Coupons

Static Coupons Pre-conditioning Data						
Test Type	**Test Description**	**Test Sample ID Code**	**Duration [hr]**	**Date Conditioned**	**Temperature [ºC]**	**Relative Humidity [%]**
Static	Rectangular Bar Raster Thickness: 0.018 in.	KK1	40	3/22/2017-3/24/2017	23	21
Static	Rectangular Bar Raster Thickness: 0.018 in.	KK2	40	3/22/2017-3/24/2017	23	21
Static	Rectangular Bar Raster Thickness: 0.018 in.	KK3	40	3/22/2017-3/24/2017	23	21
Static	Rectangular Bar Raster Thickness: 0.024 in.	LL1	40	3/22/2017-3/24/2017	23	21
Static	Rectangular Bar Raster Thickness: 0.024 in.	LL2	40	3/22/2017-3/24/2017	23	21
Static	Rectangular Bar Raster Thickness: 0.024 in.	LL3	40	3/22/2017-3/24/2017	23	21
Static	Rectangular Bar Raster Thickness: 0.030 in.	MM1	40	3/22/2017-3/24/2017	23	21
Static	Rectangular Bar Raster Thickness: 0.030 in.	MM2	40	3/22/2017-3/24/2017	23	21
Static	Rectangular Bar Raster Thickness: 0.030 in.	MM3	40	3/22/2017-3/24/2017	23	21

Table C-6. Precondition Data for Fatigue Test Coupons

Fatigue Coupons Pre-conditioning Data						
Test Type	**Test Description**	**Test Sample ID Code**	**Duration [hr]**	**Date Conditioned**	**Temperature [ºC]**	**Relative Humidity [%]**
Fatigue	Tension-Tension Fatigue at 80% UTS	Q1	40	3/14/2017-3/16/2017	21	20
Fatigue	Tension-Tension Fatigue at 80% UTS	Q2	40	3/14/2017-3/16/2018	21	20
Fatigue	Tension-Tension Fatigue at 80% UTS	Q3	40	3/14/2017-3/16/2019	21	20
Fatigue	Tension-Tension Fatigue at 60% UTS	R1	40	3/14/2017-3/16/2020	21	20
Fatigue	Tension-Tension Fatigue at 60% UTS	R2	40	3/14/2017-3/16/2021	21	20
Fatigue	Tension-Tension Fatigue at 60% UTS	R3	40	3/14/2017-3/16/2022	21	20
Fatigue	Contour Thickness: 0.030 in. at 20% UTS	Y1.1	40	7/26/2017-7/28/2017	21	56
Fatigue	Contour Thickness: 0.030 in. at 20% UTS	Y2.1	40	7/26/2017-7/28/2017	21	56
Fatigue	Contour Thickness: 0.030 in. at 20% UTS	Y3.1	40	7/26/2017-7/28/2017	21	56
Fatigue	Contour Thickness: 0.030 in. at 80% UTS	Z1	40	3/13/2017-3/15/2017	22	22
Fatigue	Contour Thickness: 0.030 in. at 80% UTS	Z2	40	3/13/2017-3/15/2017	22	22
Fatigue	Contour Thickness: 0.030 in. at 80% UTS	Z3	40	3/13/2017-3/15/2017	22	22
Fatigue	Contour Thickness: 0.030 in. at 60% UTS	AA1	40	3/13/2017-3/15/2017	22	22
Fatigue	Contour Thickness: 0.030 in. at 60% UTS	AA2	40	3/13/2017-3/15/2017	22	22
Fatigue	Contour Thickness: 0.030 in. at 60% UTS	AA3	40	3/13/2017-3/15/2017	22	22
Fatigue	Contour Thickness: 0.030 in. 30% UTS	BB1	40	7/26/2017-7/28/2017	21	56
Fatigue	Contour Thickness: 0.030 in. 30% UTS	BB2	40	7/26/2017-7/28/2017	21	56
Fatigue	Contour Thickness: 0.030 in. 30% UTS	BB3	40	7/26/2017-7/28/2017	21	56
Fatigue	Raster Thickness: 0.030 in. at 30% UTS	GG1	40	7/26/2017-7/28/2017	21	56
Fatigue	Raster Thickness: 0.030 in. at 30% UTS	GG2	40	7/26/2017-7/28/2017	21	56
Fatigue	Raster Thickness: 0.030 in. at 30% UTS	GG3	40	7/26/2017-7/28/2017	21	56
Fatigue	Raster Thickness: 0.030 in. at 20% UTS	HH1	40	7/26/2017-7/28/2017	21	56
Fatigue	Raster Thickness: 0.030 in. at 20% UTS	HH2	40	7/26/2017-7/28/2017	21	56
Fatigue	Raster Thickness: 0.030 in. at 20% UTS	HH3	40	7/26/2017-7/28/2017	21	56

Table C-7. Precondition Data for Fatigue Test Coupons

Fatigue Coupons Pre-conditioning Data						
Test Type	**Test Description**	**Test Sample ID Code**	**Duration [hr]**	**Date Conditioned**	**Temperature [ºC]**	**Relative Humidity [%]**
Fatigue	Raster Thickness: 0.030 in. at 60% UTS	II1	40	7/26/2017-7/28/2017	21	56
Fatigue	Raster Thickness: 0.030 in. at 60% UTS	II2	40	7/26/2017-7/28/2017	21	56
Fatigue	Raster Thickness: 0.030 in. at 60% UTS	II3	40	7/26/2017-7/28/2017	21	56
Fatigue	Raster Thickness: 0.030 in. at 80% UTS	JJ1	40	7/26/2017-7/28/2017	21	56
Fatigue	Raster Thickness: 0.030 in. at 80% UTS	JJ2	40	7/26/2017-7/28/2017	21	56
Fatigue	Raster Thickness: 0.030 in. at 80% UTS	JJ3	40	7/26/2017-7/28/2017	21	56
Fatigue	Tension-Tension Fatigue at 30% UTS	NN1	40	5/15/2017-5/17/2017	22	45
Fatigue	Tension-Tension Fatigue at 30% UTS	NN2	40	5/15/2017-5/17/2017	22	45
Fatigue	Tension-Tension Fatigue at 30% UTS	NN3	40	5/15/2017-5/17/2017	22	45
Fatigue	Tension-Tension Fatigue at 20% UTS	OO1	40	5/17/2017-5/19/2017	22	54
Fatigue	Tension-Tension Fatigue at 20% UTS	OO2	40	5/17/2017-5/19/2017	22	54
Fatigue	Tension-Tension Fatigue at 20% UTS	OO3	40	5/17/2017-5/19/2017	22	54
Fatigue	Tension-Tension Fatigue at 10% UTS	PP1	40	5/19/2017-5/21/2017	20	54
Fatigue	Tension-Tension Fatigue at 10% UTS	PP2	40	5/19/2017-5/21/2017	20	54
Fatigue	Tension-Tension Fatigue at 10% UTS	PP3	40	5/19/2017-5/21/2017	20	54
Fatigue	Fully Reversed Fatigue at 16% UTS	QQ1	40	5/12/2017-5/14/2017	21	50
Fatigue	Fully Reversed Fatigue at 16% UTS	QQ2	40	5/12/2017-5/14/2017	21	50
Fatigue	Fully Reversed Fatigue at 16% UTS	QQ3	40	5/12/2017-5/14/2017	21	50
Fatigue	Fully Reversed Fatigue at 10% UTS	RR1	40	6/11/2017-6/13/2017	20	54
Fatigue	Fully Reversed Fatigue at 10% UTS	RR2	40	6/11/2017-6/13/2017	20	54
Fatigue	Fully Reversed Fatigue at 10% UTS	RR3	40	6/11/2017-6/13/2017	20	54
Fatigue	Orientation XZY: Low Stress < 250 PSI	TT1	40	6/10/2017-6/12/2017	24	39
Fatigue	Orientation XZY: Low Stress < 250 PSI	TT2	40	6/10/2017-6/12/2017	24	39
Fatigue	Orientation XZY: Low Stress < 250 PSI	TT3	40	6/10/2017-6/12/2017	24	39

Table C-8. Precondition Data for Fatigue Test Coupons

Fatigue Coupons Pre-conditioning Data						
Test Type	**Test Description**	**Test Sample ID Code**	**Duration [hr]**	**Date Conditioned**	**Temperature [ºC]**	**Relative Humidity [%]**
Fatigue	Fully Reversed Fatigue at 20% UTS	VV1	40	5/28/2017-5/30/2017	20	54
Fatigue	Fully Reversed Fatigue at 20% UTS	VV2	40	5/28/2017-5/30/2017	20	54
Fatigue	Fully Reversed Fatigue at 20% UTS	VV3	40	5/28/2017-5/30/2017	20	54
Fatigue	Fully Reversed Fatigue at 25% UTS	WW1	40	6/10/2017-6/12/2017	24	39
Fatigue	Fully Reversed Fatigue at 25% UTS	WW2	40	6/10/2017-6/12/2017	24	39
Fatigue	Fully Reversed Fatigue at 25% UTS	WW3	40	6/10/2017-6/12/2017	24	39
Fatigue	Fully Reversed Fatigue at 10% UTS	XX1	40	6/1/2017-6/3/2017	20	50
Fatigue	Fully Reversed Fatigue at 10% UTS	XX2	40	6/1/2017-6/3/2017	20	50
Fatigue	Fully Reversed Fatigue at 10% UTS	XX3	40	6/1/2017-6/3/2017	20	50

Appendix D: Testing Environmental Condition

Table D-1. Environmental Condition for Static Testing

Static Testing Environmental Conditions					
Dates	**Test Type**	**Test Description**	**Test Sample ID Code**	**Temperature [ºC]**	**Relative Humidity [%]**
1/19/2017	Static	Standard Build XYZ (User Seam Placement)	A1	21	31
1/19/2017	Static	Standard Build XYZ (User Seam Placement)	A2	21	31
1/19/2017	Static	Standard Build XYZ (User Seam Placement)	A3	21	31
1/19/2017	Static	Standard Build XYZ (User Seam Placement)	A4	21	31
1/19/2017	Static	Standard Build XYZ (User Seam Placement)	A5	21	31
1/19/2017	Static	Standard Build XYZ (User Seam Placement)	A6	21	31
1/25/2017	Static	Standard Build XYZ (Random Seam Placement)	A1.1	21	31
1/25/2017	Static	Standard Build XYZ (Random Seam Placement)	A2.1	21	31
1/25/2017	Static	Standard Build XYZ (Random Seam Placement)	A3.1	21	31
1/25/2017	Static	Standard Build XYZ (Random Seam Placement)	A4.1	21	31
1/25/2017	Static	Standard Build XYZ (Random Seam Placement)	A5.1	21	31
1/25/2017	Static	Standard Build XYZ (Random Seam Placement)	A6.1	21	31
3/23/2017	Static	Standard Build XZY	B1	24	24
3/23/2017	Static	Standard Build XZY	B2	24	24
3/23/2017	Static	Standard Build XZY	B3	24	24
3/23/2017	Static	Standard Build XZY	B4	24	24
3/23/2017	Static	Standard Build XZY	B5	24	24
3/23/2017	Static	Standard Build XZY	B6	24	24
3/23/2017	Static	Standard Build XZY	B7	24	24
3/23/2017	Static	Standard Build XZY	B8	24	24
3/23/2017	Static	Standard Build XZY	B9	24	24
3/23/2017	Static	Standard Build XZY	B10	24	24
3/23/2017	Static	Standard Build XZY	B11	24	24
3/23/2017	Static	Standard Build XZY	B12	24	24
3/23/2017	Static	Standard Build XZY	B13	24	24

Table D-2. Environmental Condition for Static Testing

Static Testing Environmental Conditions					
Dates	**Test Type**	**Test Description**	**Test Sample ID Code**	**Temperature [ºC]**	**Relative Humidity [%]**
3/23/2017	Static	Raster Angle: 15º/-75º	E1	24	24
3/23/2017	Static	Raster Angle: 15º/-75º	E2	24	24
3/23/2017	Static	Raster Angle: 15º/-75º	E3	24	24
3/23/2017	Static	Raster Angle: 15º/-75º	E4	24	24
3/23/2017	Static	Raster Angle: 15º/-75º	E5	24	24
3/23/2017	Static	Raster Angle: 15º/-75º	E6	24	24
3/23/2017	Static	Raster Angle: 15º/-75º	E7	24	24
3/23/2017	Static	Raster Angle: 30º/-60º	F1	24	24
3/23/2017	Static	Raster Angle: 30º/-60º	F2	24	24
3/23/2017	Static	Raster Angle: 30º/-60º	F3	24	24
3/23/2017	Static	Raster Angle: 30º/-60º	F4	24	24
3/23/2017	Static	Raster Angle: 30º/-60º	F5	24	24
3/23/2017	Static	Raster Angle: 30º/-60º	F6	24	24
3/23/2017	Static	Raster Angle: 30º/-60º	F7	24	24
3/23/2017	Static	Raster Thickness: 0.018 in.	G1	24	24
3/23/2017	Static	Raster Thickness: 0.018 in.	G2	24	24
3/23/2017	Static	Raster Thickness: 0.018 in.	G3	24	24
3/23/2017	Static	Raster Thickness: 0.018 in.	G4	24	24
3/23/2017	Static	Raster Thickness: 0.018 in.	G5	24	24
3/23/2017	Static	Raster Thickness: 0.018 in.	G6	24	24
3/23/2017	Static	Raster Thickness: 0.018 in.	G7	24	24

Table D-3. Environmental Condition for Static Testing

Static Testing Environmental Conditions					
Dates	**Test Type**	**Test Description**	**Test Sample ID Code**	**Temperature [ºC]**	**Relative Humidity [%]**
3/23/2017	Static	Raster Thickness: 0.024 in.	H1	24	24
3/23/2017	Static	Raster Thickness: 0.024 in.	H2	24	24
3/23/2017	Static	Raster Thickness: 0.024 in.	H3	24	24
3/23/2017	Static	Raster Thickness: 0.024 in.	H4	24	24
3/23/2017	Static	Raster Thickness: 0.024 in.	H5	24	24
3/23/2017	Static	Raster Thickness: 0.024 in.	H6	24	24
3/23/2017	Static	Raster Thickness: 0.024 in.	H7	24	24
3/23/2017	Static	Raster Thickness: 0.030 in.	I1	24	24
3/23/2017	Static	Raster Thickness: 0.030 in.	I2	24	24
3/23/2017	Static	Raster Thickness: 0.030 in.	I3	24	24
3/23/2017	Static	Raster Thickness: 0.030 in.	I4	24	24
3/23/2017	Static	Raster Thickness: 0.030 in.	I5	24	24
3/23/2017	Static	Raster Thickness: 0.030 in.	I6	24	24
3/23/2017	Static	Raster Thickness: 0.030 in.	I7	24	24
2/9/2017	Static	Contour Thickness: 0.018 in.	J1	18	30
2/9/2017	Static	Contour Thickness: 0.018 in.	J2	18	30
2/9/2017	Static	Contour Thickness: 0.018 in.	J3	18	30
2/9/2017	Static	Contour Thickness: 0.018 in.	J4	18	30
2/9/2017	Static	Contour Thickness: 0.018 in.	J5	18	30
2/9/2017	Static	Contour Thickness: 0.024 in.	K1	18	30
2/9/2017	Static	Contour Thickness: 0.024 in.	K2	18	30
2/9/2017	Static	Contour Thickness: 0.024 in.	K3	18	30
2/9/2017	Static	Contour Thickness: 0.024 in.	K4	18	30
2/9/2017	Static	Contour Thickness: 0.024 in.	K5	18	30

Table D-4. Environmental Condition for Static Testing

Static Testing Environmental Conditions					
Dates	**Test Type**	**Test Description**	**Test Sample ID Code**	**Temperature [ºC]**	**Relative Humidity [%]**
2/9/2017	Static	Contour Thickness: 0.030 in.	L1	18	30
2/9/2017	Static	Contour Thickness: 0.030 in.	L2	18	30
2/9/2017	Static	Contour Thickness: 0.030 in.	L3	18	30
2/9/2017	Static	Contour Thickness: 0.030 in.	L4	18	30
2/9/2017	Static	Contour Thickness: 0.030 in.	L5	18	30
2/9/2017	Static	Number of Contour: 2	M1	18	30
2/9/2017	Static	Number of Contour: 2	M2	18	30
2/9/2017	Static	Number of Contour: 2	M3	18	30
2/9/2017	Static	Number of Contour: 2	M4	18	30
2/9/2017	Static	Number of Contour: 2	M5	18	30
2/9/2017	Static	Number of Contour: 3	N1	18	30
2/9/2017	Static	Number of Contour: 3	N2	18	30
2/9/2017	Static	Number of Contour: 3	N3	18	30
2/9/2017	Static	Number of Contour: 3	N4	18	30
2/9/2017	Static	Number of Contour: 3	N5	18	30
2/9/2017	Static	Contour Thickness: 0.03 in.; Number of Contours: 2	O1	18	30
2/9/2017	Static	Contour Thickness: 0.03 in.; Number of Contours: 2	O2	18	30
2/9/2017	Static	Contour Thickness: 0.03 in.; Number of Contours: 2	O3	18	30
2/9/2017	Static	Contour Thickness: 0.03 in.; Number of Contours: 2	O4	18	30
2/9/2017	Static	Contour Thickness: 0.03 in.; Number of Contours: 2	O5	18	30

Table D-5. Environmental Condition for Fatigue Testing

Fatigue Testing Environmental Conditions					
Dates	**Test Type**	**Test Description**	**Test Sample ID Code**	**Temperature [ºC]**	**Relative Humidity [%]**
7/8/2017	Fatigue	Contour Thickness: 0.030 in. at 20% UTS	Y1.1	20	50
7/8/2017	Fatigue	Contour Thickness: 0.030 in. at 20% UTS	Y2.1	20	50
7/8/2017	Fatigue	Contour Thickness: 0.030 in. at 20% UTS	Y3.1	20	50
5/26/2017	Fatigue	Contour Thickness: 0.030 in. at 60% UTS	AA1	20	50
5/26/2017	Fatigue	Contour Thickness: 0.030 in. at 60% UTS	AA2	20	50
5/26/2017	Fatigue	Contour Thickness: 0.030 in. at 60% UTS	AA3	20	50
5/26/2017	Fatigue	Contour Thickness: 0.030 in. at 80% UTS	Z1	20	50
5/26/2017	Fatigue	Contour Thickness: 0.030 in. at 80% UTS	Z2	20	50
5/26/2017	Fatigue	Contour Thickness: 0.030 in. at 80% UTS	Z3	20	50
6/5/2017	Fatigue	Fully Reversed Fatigue at 10% UTS	XX1	21	50
6/5/2017	Fatigue	Fully Reversed Fatigue at 10% UTS	XX2	21	50
6/5/2017	Fatigue	Fully Reversed Fatigue at 10% UTS	XX3	21	50
6/13/2017	Fatigue	Fully Reversed Fatigue at 10% UTS	RR1	21	52
6/13/2017	Fatigue	Fully Reversed Fatigue at 10% UTS	RR2	21	52
6/13/2017	Fatigue	Fully Reversed Fatigue at 10% UTS	RR3	21	52
5/14/2017	Fatigue	Fully Reversed Fatigue at 16% UTS	QQ1	20	50
5/14/2017	Fatigue	Fully Reversed Fatigue at 16% UTS	QQ2	20	50
5/14/2017	Fatigue	Fully Reversed Fatigue at 16% UTS	QQ3	20	50
5/31/2017	Fatigue	Fully Reversed Fatigue at 20% UTS	VV1	20	51
5/31/2017	Fatigue	Fully Reversed Fatigue at 20% UTS	VV2	20	51
5/31/2017	Fatigue	Fully Reversed Fatigue at 20% UTS	VV3	20	51

Table D-6. Environmental Condition for Fatigue Testing

Fatigue Testing Environmental Conditions					
Dates	**Test Type**	**Test Description**	**Test Sample ID Code**	**Temperature [ºC]**	**Relative Humidity [%]**
6/12/2017	Fatigue	Fully Reversed Fatigue at 25% UTS	WW1	20	50
6/12/2017	Fatigue	Fully Reversed Fatigue at 25% UTS	WW2	20	50
6/12/2017	Fatigue	Fully Reversed Fatigue at 25% UTS	WW3	20	50
5/20/2017	Fatigue	Orientation XZY: Low Stress < 250 PSI	TT1	21	52
5/20/2017	Fatigue	Orientation XZY: Low Stress < 250 PSI	TT2	21	52
5/20/2017	Fatigue	Orientation XZY: Low Stress < 250 PSI	TT3	21	52
7/6/2017	Fatigue	Raster Thickness: 0.030 in. at 20% UTS	HH1	20	50
7/6/2017	Fatigue	Raster Thickness: 0.030 in. at 20% UTS	HH2	20	50
7/6/2017	Fatigue	Raster Thickness: 0.030 in. at 20% UTS	HH3	20	50
7/3/2017	Fatigue	Raster Thickness: 0.030 in. at 30% UTS	GG1	20	50
7/3/2017	Fatigue	Raster Thickness: 0.030 in. at 30% UTS	GG2	20	50
7/3/2017	Fatigue	Raster Thickness: 0.030 in. at 30% UTS	GG3	20	50
Not Tested	Fatigue	Raster Thickness: 0.030 in. at 60% UTS	II1	Not Tested	Not Tested
Not Tested	Fatigue	Raster Thickness: 0.030 in. at 60% UTS	II2	Not Tested	Not Tested
Not Tested	Fatigue	Raster Thickness: 0.030 in. at 60% UTS	II3	Not Tested	Not Tested
Not Tested	Fatigue	Raster Thickness: 0.030 in. at 80% UTS	JJ1	Not Tested	Not Tested
Not Tested	Fatigue	Raster Thickness: 0.030 in. at 80% UTS	JJ2	Not Tested	Not Tested
Not Tested	Fatigue	Raster Thickness: 0.030 in. at 80% UTS	JJ3	Not Tested	Not Tested
5/20/2017	Fatigue	Tension-Tension Fatigue at 10% UTS	PP1	21	52
5/20/2017	Fatigue	Tension-Tension Fatigue at 10% UTS	PP2	21	52
5/20/2017	Fatigue	Tension-Tension Fatigue at 10% UTS	PP3	21	52

Table D-7. Environmental Condition for Fatigue Testing

Fatigue Testing Environmental Conditions					
Dates	**Test Type**	**Test Description**	**Test Sample ID Code**	**Temperature [ºC]**	**Relative Humidity [%]**
5/20/2017	Fatigue	Tension-Tension Fatigue at 20% UTS	OO1	21	52
5/20/2017	Fatigue	Tension-Tension Fatigue at 20% UTS	OO2	21	52
5/20/2017	Fatigue	Tension-Tension Fatigue at 20% UTS	OO3	21	52
5/18/2017	Fatigue	Tension-Tension Fatigue at 30% UTS	NN1	21	49
5/18/2017	Fatigue	Tension-Tension Fatigue at 30% UTS	NN2	21	49
5/18/2017	Fatigue	Tension-Tension Fatigue at 30% UTS	NN3	21	49
5/26/2017	Fatigue	Tension-Tension Fatigue at 60% UTS	R1	20	50
5/26/2017	Fatigue	Tension-Tension Fatigue at 60% UTS	R2	20	50
5/26/2017	Fatigue	Tension-Tension Fatigue at 60% UTS	R3	20	50
5/26/2017	Fatigue	Tension-Tension Fatigue at 80% UTS	Q1	20	50
5/26/2017	Fatigue	Tension-Tension Fatigue at 80% UTS	Q2	20	50
5/26/2017	Fatigue	Tension-Tension Fatigue at 80% UTS	Q3	20	50

Appendix E: Static Testing Raw Data

Table E-1. Orientation XYZ Raw Data

Orientation XYZ		
Test Code	**Ultimate Tensile Stress [psi]**	**Average Ultimate Tensile Stress [psi]**
A2.1	8100	8170
A3.1	8140	
A4.1	8190	**Standard Deviation [psi]**
A5.1	8360	117
A6.1	8060	

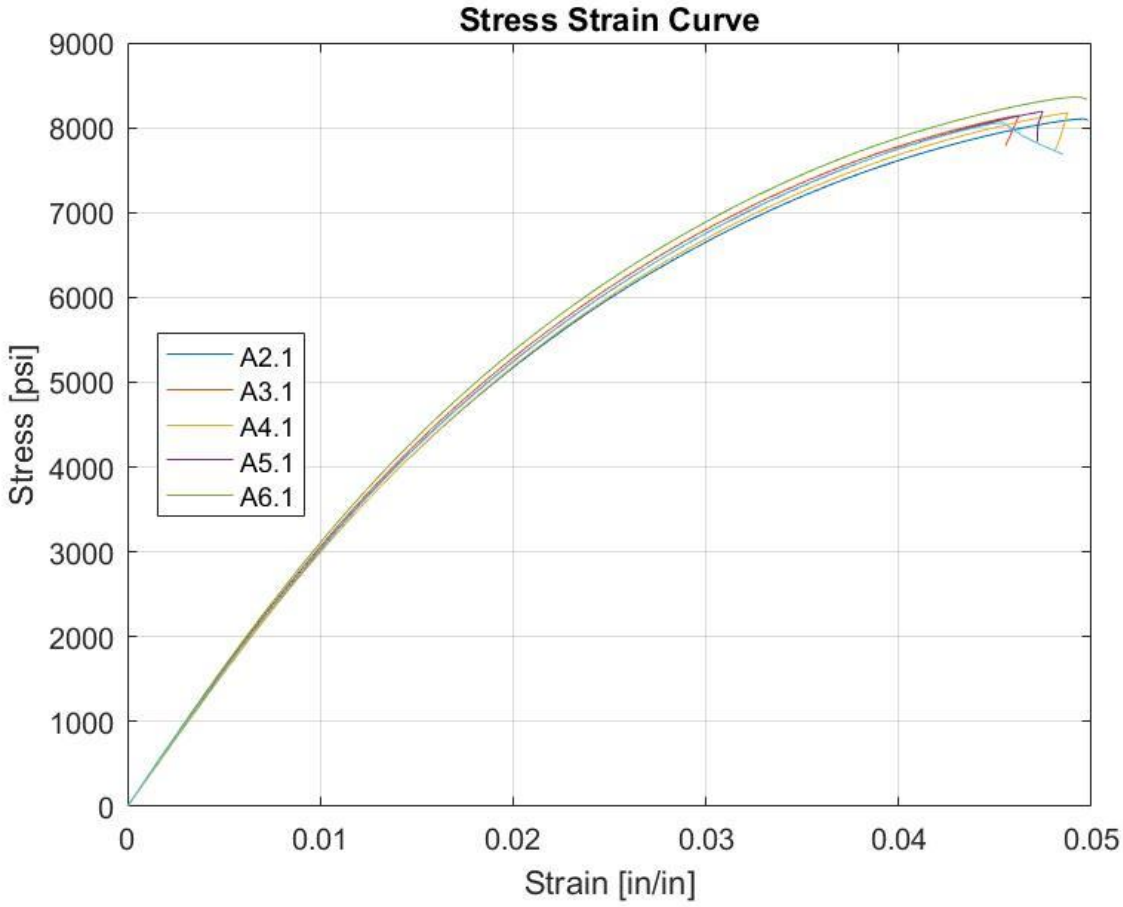

Figure E-1. Orientation XYZ Stress-Strain Curve

Table E-2. Orientation XZY Raw Data

Orientation XZY		
Test Code	**Ultimate Tensile Stress [psi]**	**Average Ultimate Tensile Stress [psi]**
B7	10000	10100
B8	10200	
B9	10100	**Standard Deviation [psi]**
B13	10100	76.4
B10	10000	

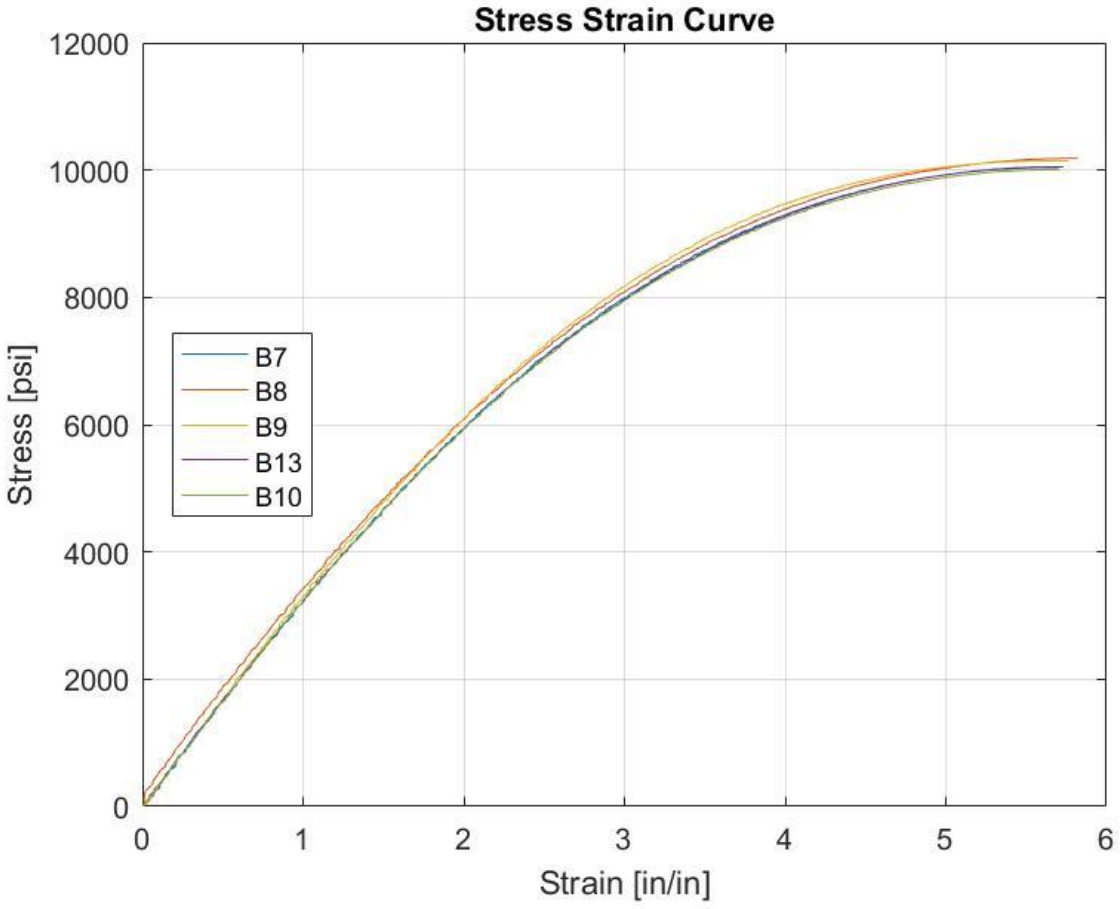

Figure E-2. Orientation XZY Stress-Strain Curve

Table E-3. Orientation ZXY Raw Data

Orientation ZXY		
Test Code	**Ultimate Tensile Stress [psi]**	**Average Ultimate Tensile Stress [psi]**
KK1	5240	5460
KK2	6160	
KK3	5840	**Standard Deviation [psi]**
KK4	4650	581
KK5	5410	

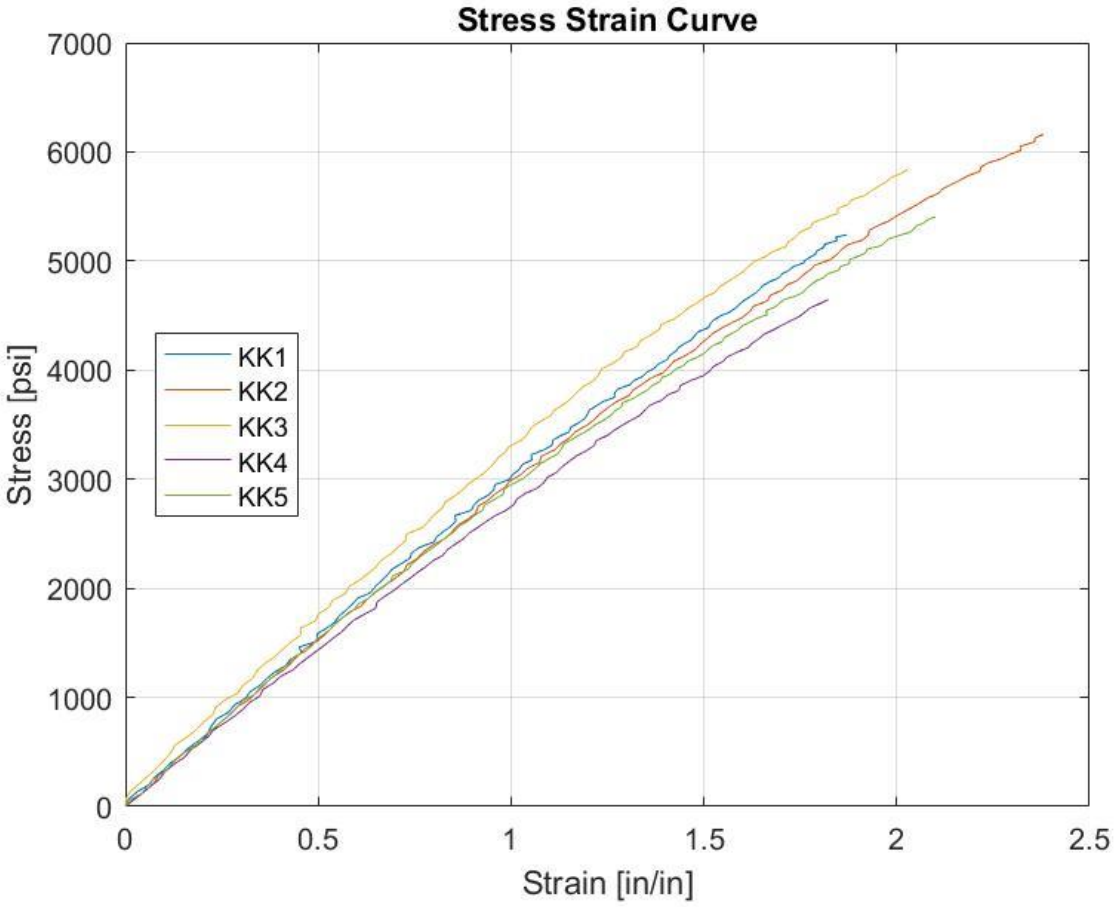

Figure E-3. Orientation ZXY Stress-Strain Curve

Table E-4. Contour Thickness: 0.018 in. Raw Data

Contour Thickness: 0.018 in.		
Test Code	**Ultimate Tensile Stress [psi]**	**Average Ultimate Tensile Stress [psi]**
J1	10300	10400
J2	10600	
J3	10300	**Standard Deviation [psi]**
J4	10500	118
J5	10400	

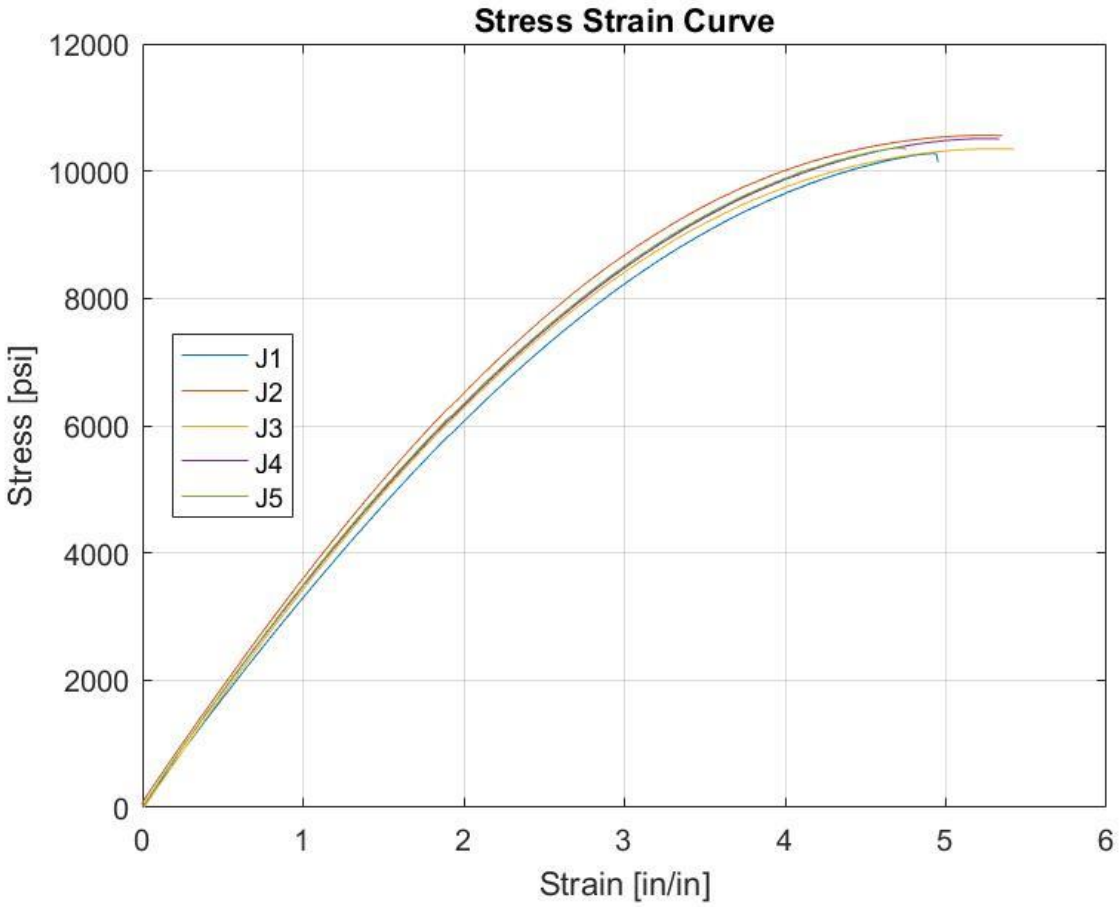

Figure E-4. Contour Thickness 0.018 in. Stress-Strain Curve

Table E-5. Contour Thickness: 0.024 in. Raw Data

Contour Thickness: 0.024 in.		
Test Code	**Ultimate Tensile Stress [psi]**	**Average Ultimate Tensile Stress [psi]**
K1	11200	11100
K2	11200	
K3	11200	**Standard Deviation [psi]**
K4	10800	200
K6	10900	

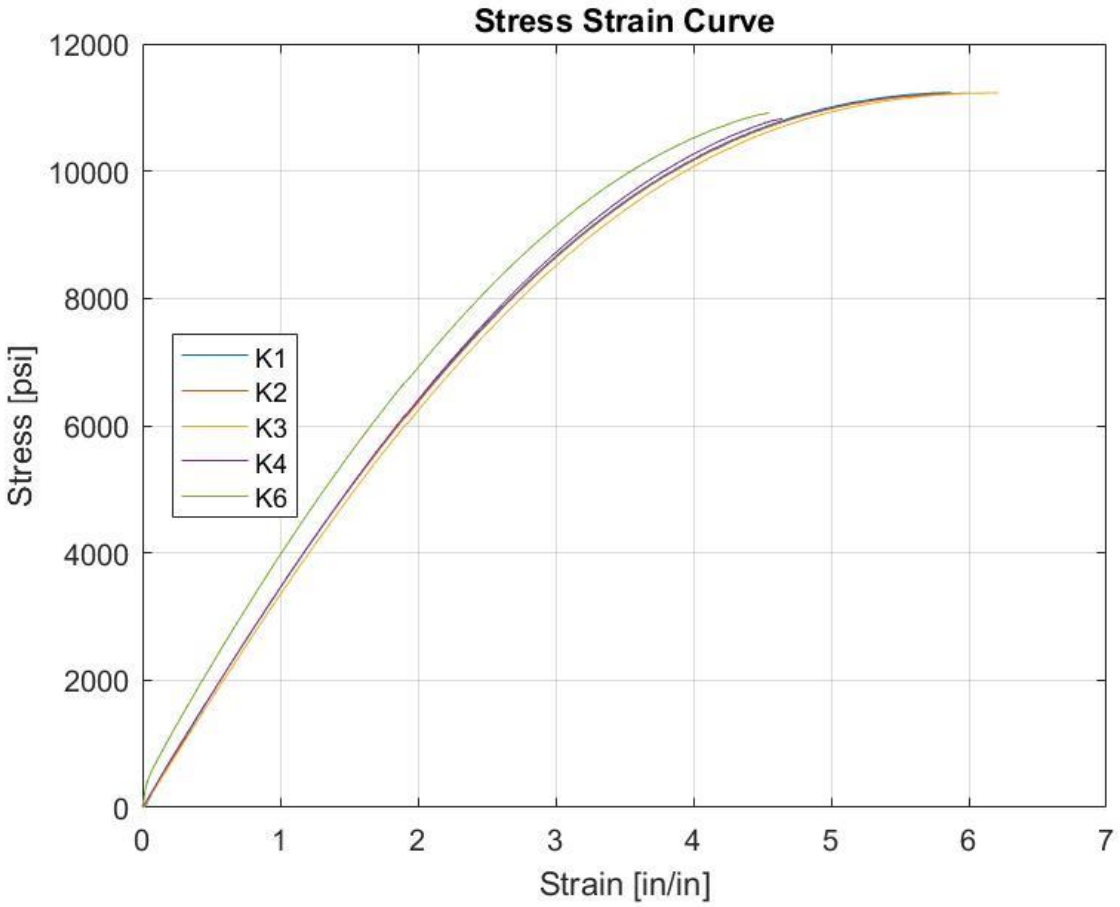

Figure E-5. Contour Thickness: 0.024 in. Stress-Strain Curve

Table E-6. Contour Thickness: 0.030 in. Raw Data

Contour Thickness: 0.030 in.		
Test Code	**Ultimate Tensile Stress [psi]**	**Average Ultimate Tensile Stress [psi]**
L1	11500	11600
L2	11500	
L3	11800	**Standard Deviation [psi]**
L4	11600	120
L5	11500	

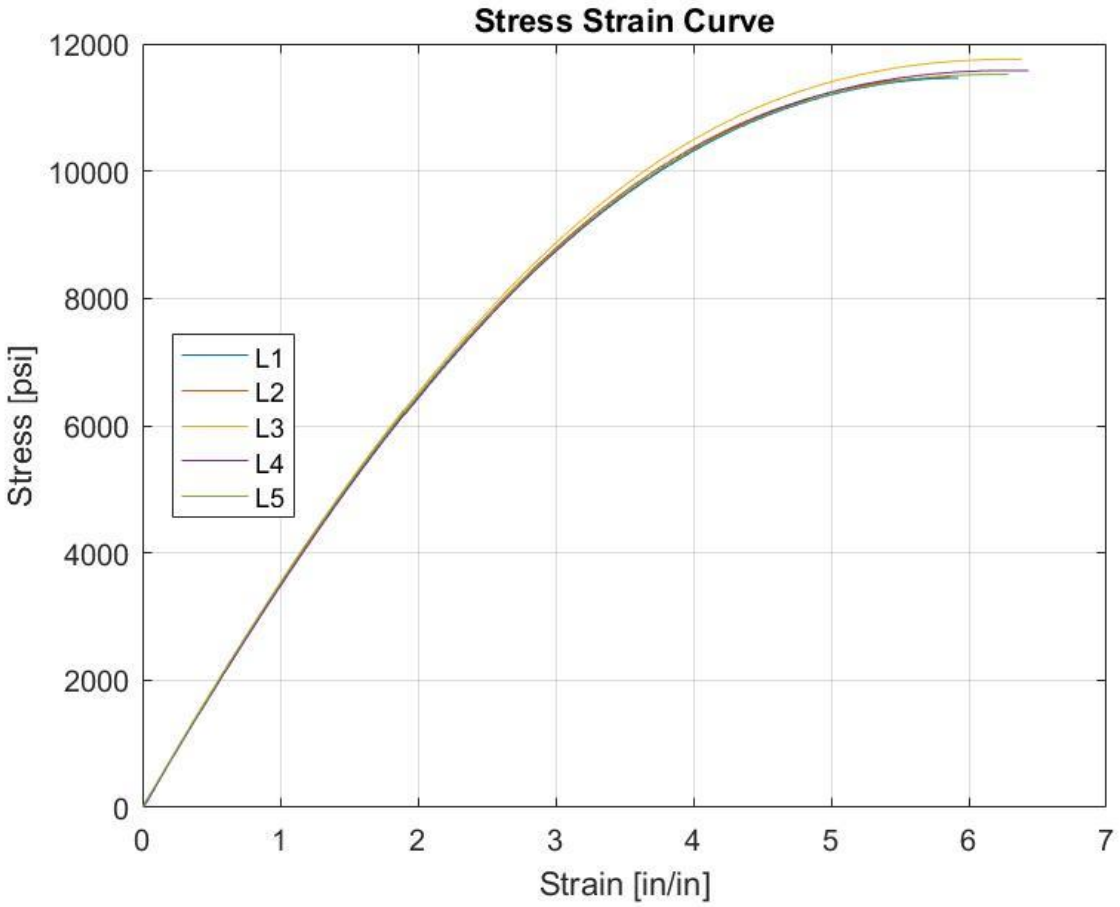

Figure E-6. Contour Thickness: 0.030 in. Stress-Strain Curve

Table E-7. Raster Thickness: 0.018 in. Raw Data

Raster Thickness: 0.018 in.		
Test Code	**Ultimate Tensile Stress [psi]**	**Average Ultimate Tensile Stress [psi]**
G1	9750	10200
G2	10500	
G3	10200	**Standard Deviation [psi]**
G4	10200	272
G5	10400	

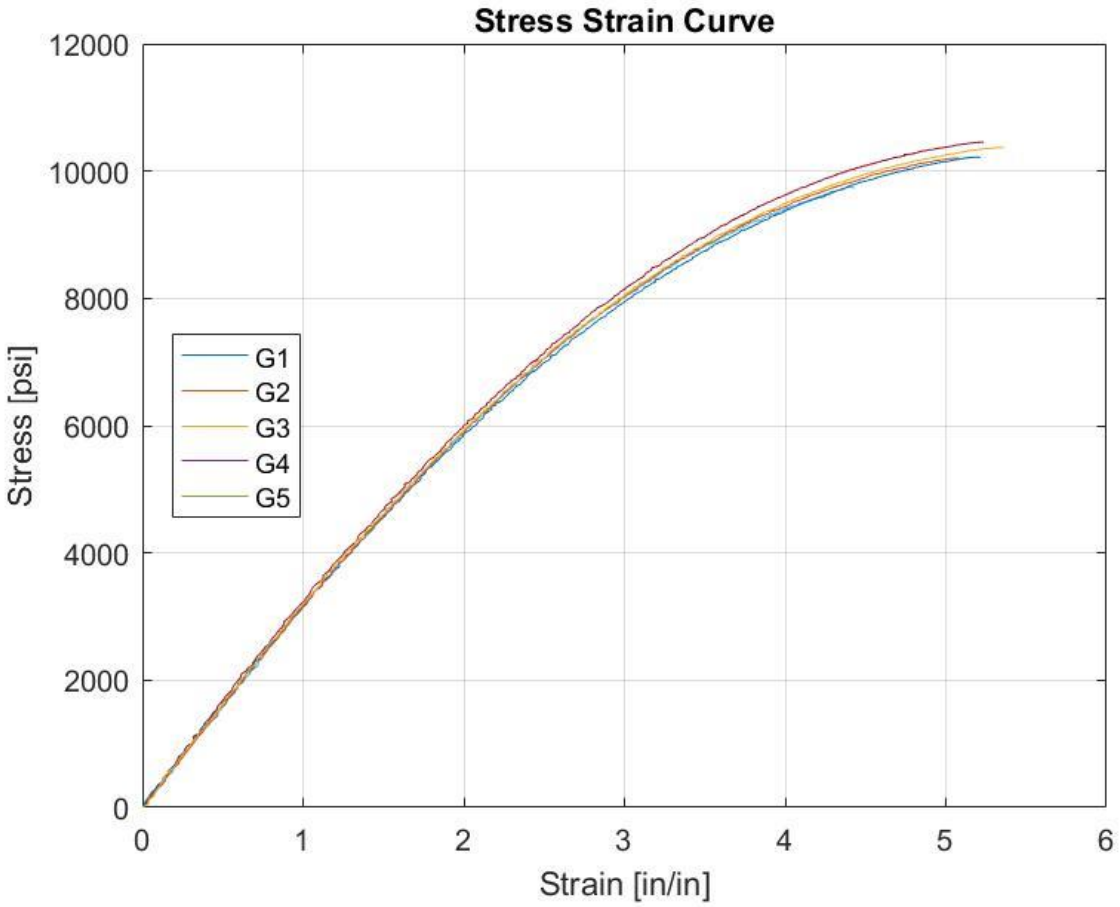

Figure E-7. Raster Thickness: 0.018 in. Stress-Strain Curve

Table E-8. Raster Thickness: 0.024 in. Raw Data

Raster Thickness: 0.024 in.		
Test Code	**Ultimate Tensile Stress [psi]**	**Average Ultimate Tensile Stress [psi]**
H1	10600	10500
H2	10600	
H3	10600	**Standard Deviation [psi]**
H4	10300	111
H5	10500	

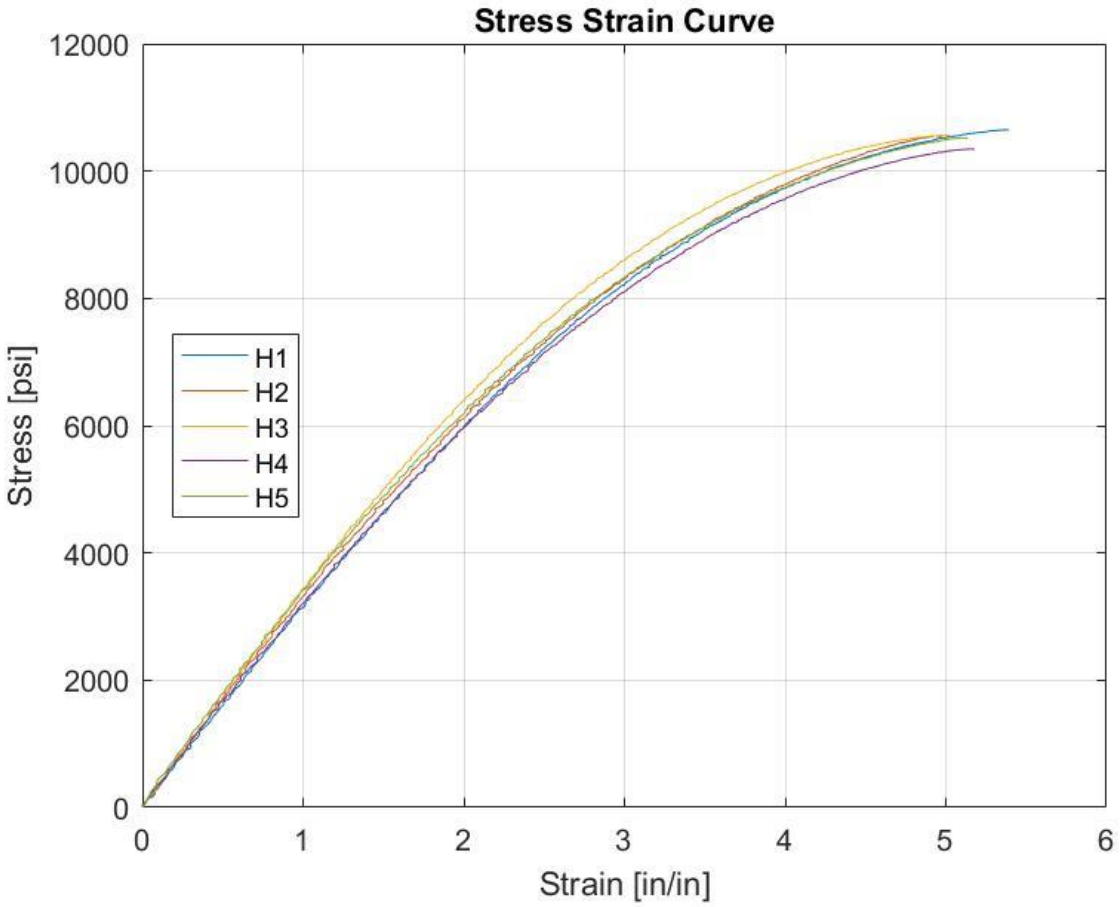

Figure E-8. Raster Thickness: 0.024 in. Stress-Strain Curve

Table E-9. Raster Thickness: 0.030 in. Raw Data

Raster Thickness: 0.030 in.		
Test Code	**Ultimate Tensile Stress [psi]**	**Average Ultimate Tensile Stress [psi]**
I1	11000	11000
I2	11000	
I3	11000	**Standard Deviation [psi]**
I4	11000	40.4
I6	11100	

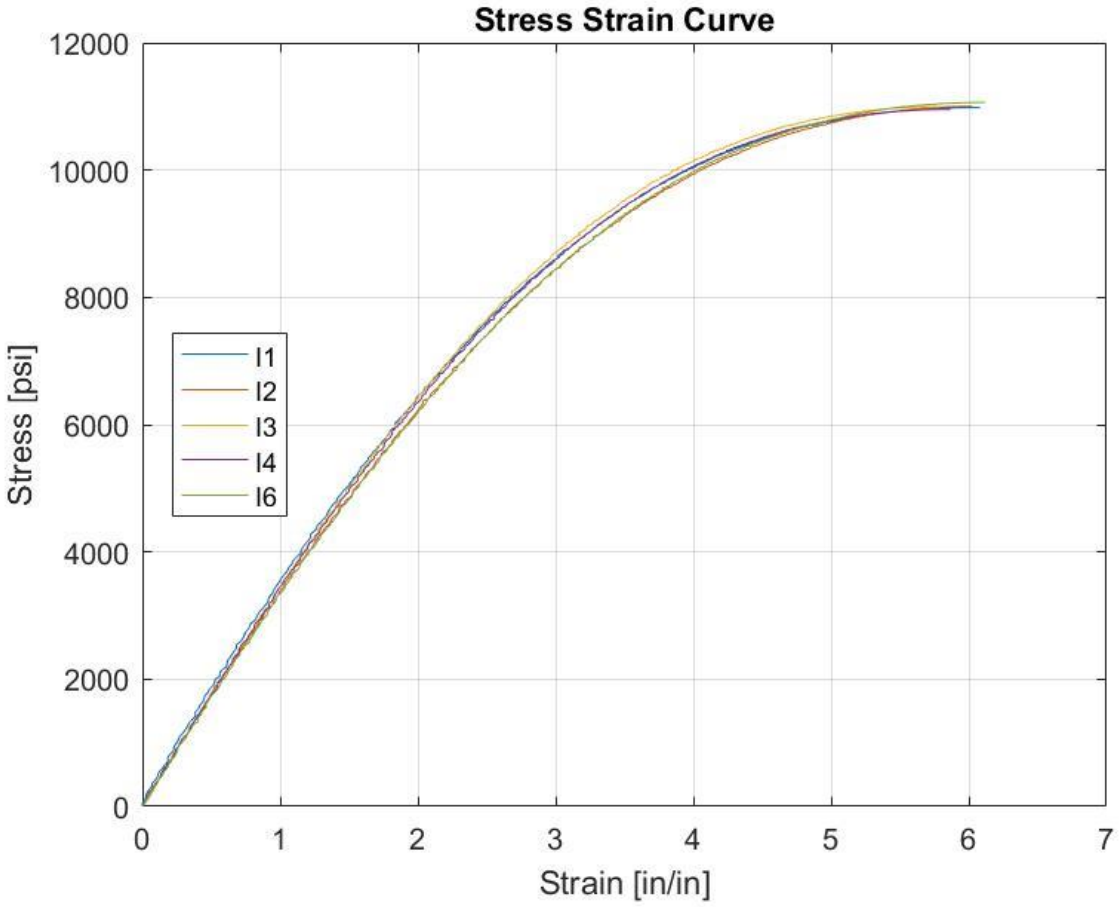

Figure E-9. Raster Thickness: 0.030 in. Stress-Strain Curve

Table E-10. Raster Angle 15º/75º Raw Data

Raster Angle: 15°/75°		
Test Code	**Ultimate Tensile Stress [psi]**	**Average Ultimate Tensile Stress [psi]**
E1	9390	9350
E2	9450	
E3	9740	**Standard Deviation [psi]**
E4	9170	272
E5	9030	

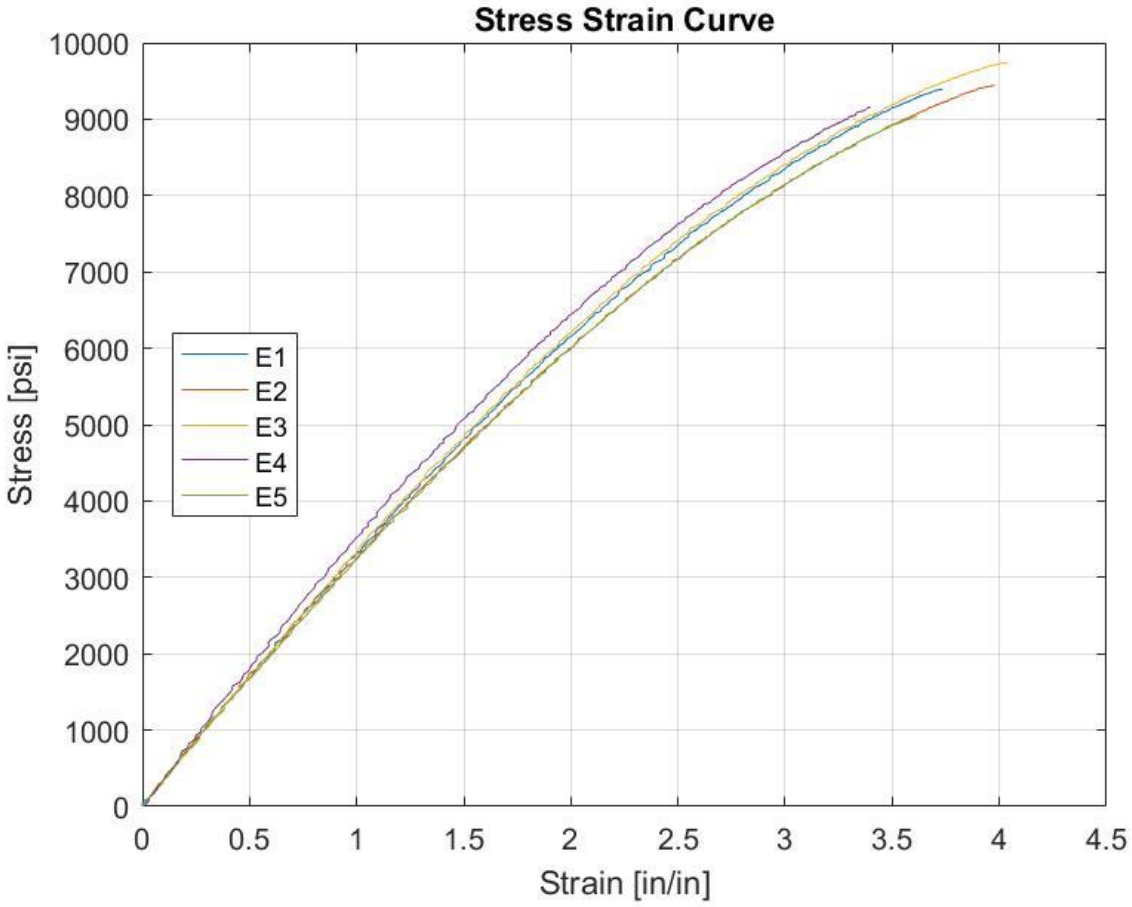

Figure E-10. Raster Angle 15º/75º Stress-Strain Curve

Table E-11. Raster Angle 30º/60º Raw Data

Raster Angle: 30°/60°		
Test Code	**Ultimate Tensile Stress [psi]**	**Average Ultimate Tensile Stress [psi]**
F1	9800	10300
F2	10400	
F3	10500	**Standard Deviation [psi]**
F4	10400	287
F5	10500	

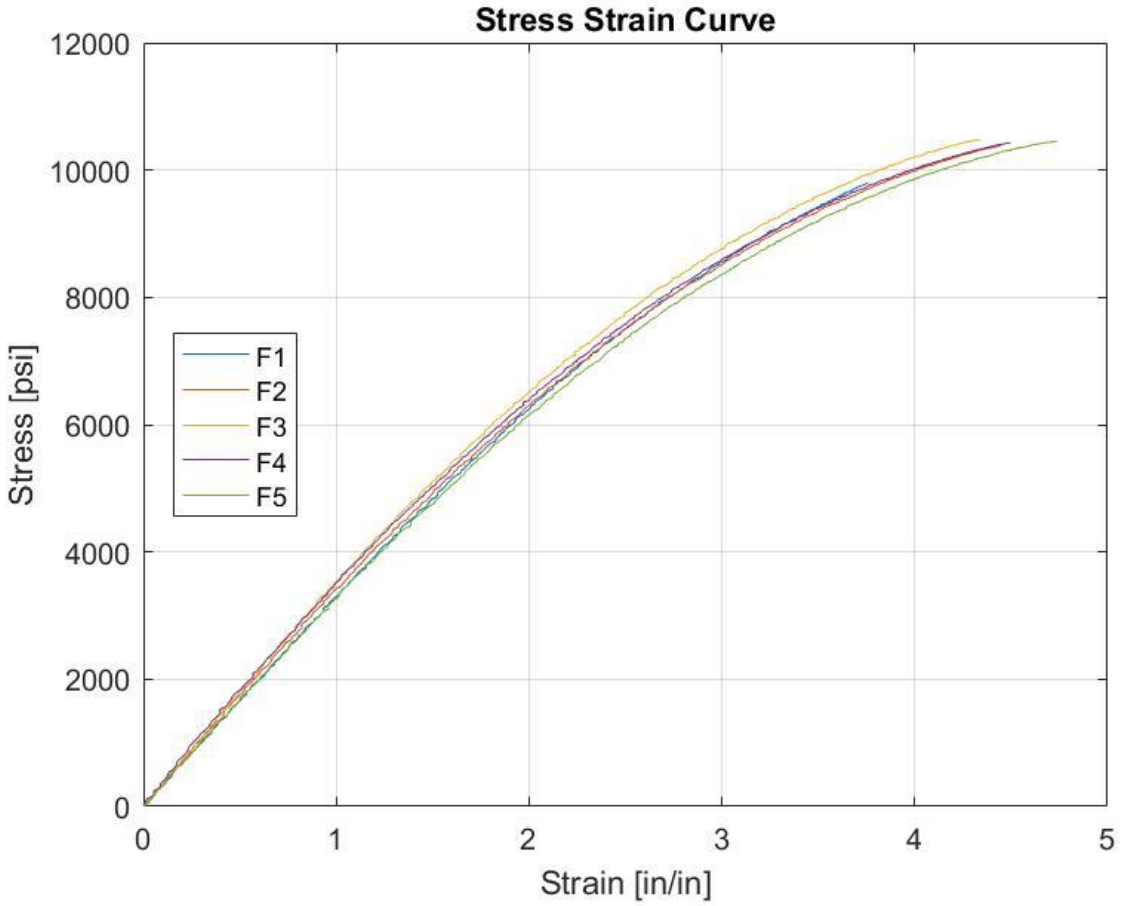

Figure E-11. Raster Angle 30º/60º Stress-Strain Curve

Table E-12. Number of Contours: 2 Raw Data

Number of Contours: 2		
Test Code	**Ultimate Tensile Stress [psi]**	**Average Ultimate Tensile Stress [psi]**
M1	11900	11800
M2	11900	
M3	12000	**Standard Deviation [psi]**
M4	12000	270
M5	11400	

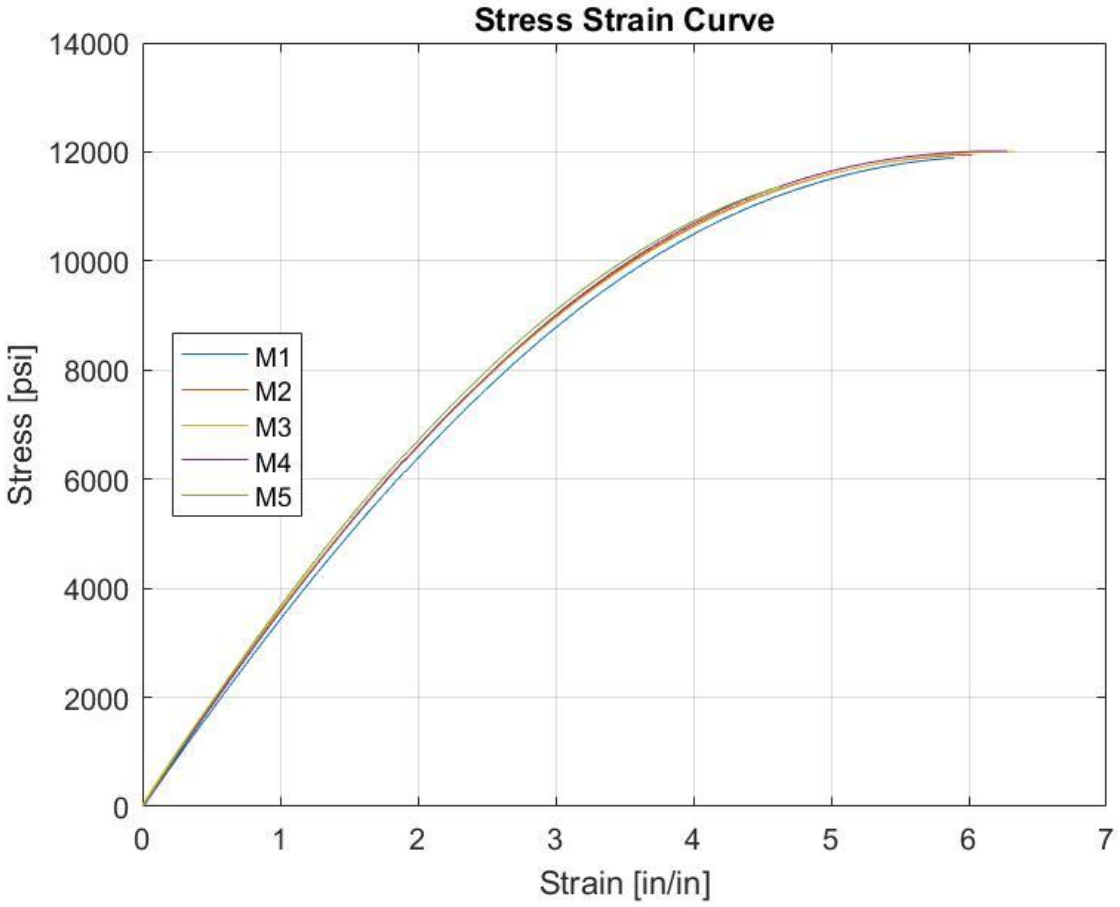

Figure E-12. Number of Contours: 2 Stress-Strain Curve

Table E-13. Number of Contours: 3 Raw Data

Number of Contours: 3		
Test Code	**Ultimate Tensile Stress [psi]**	**Average Ultimate Tensile Stress [psi]**
N1	12100	12100
N2	12000	
N3	11900	**Standard Deviation [psi]**
N4	12100	96.5
N5	12200	

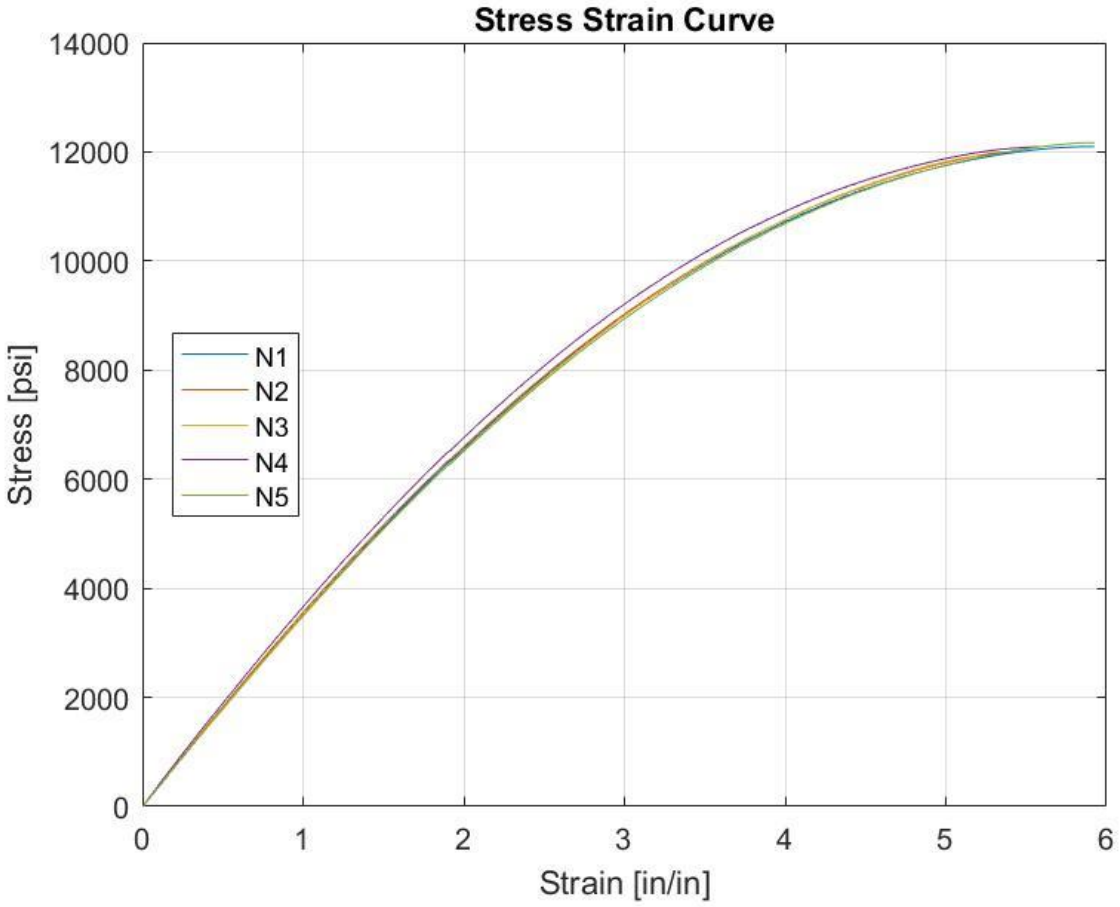

Figure E-13. Number of Contours: 3 Stress-Strain Curve

Table E-14. Contour Depth Raw Data

2 Contours & Contour Thickness: 0.030 in.		
Test Code	**Ultimate Tensile Stress [psi]**	**Average Ultimate Tensile Stress [psi]**
O1	12400	12300
O2	12100	
O3	12300	**Standard Deviation [psi]**
O4	12300	90.5
O5	12300	

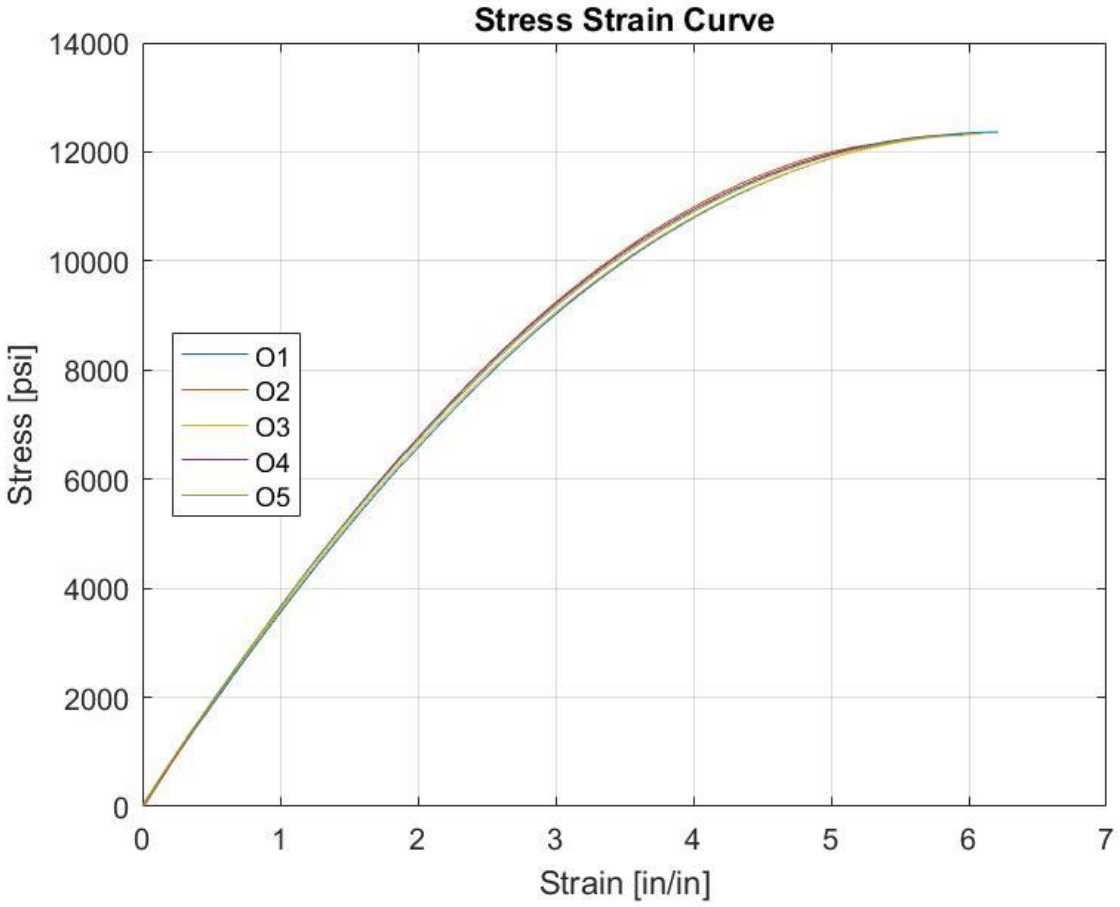

Figure E-14. Contour Depth Stress-Strain Curve

Table E-15. Rectangular Bar Raster Thickness: 0.024 in. 2 Raw Data

Rectangluar Bar | Raster Thickness: 0.024 in.		
Test Code	**Ultimate Tensile Stress [psi]**	**Average Ultimate Tensile Stress [psi]**
LL1	6360	5910
LL2	5890	
LL3	5940	**Standard Deviation [psi]**
LL4	5390	344
LL5	5950	

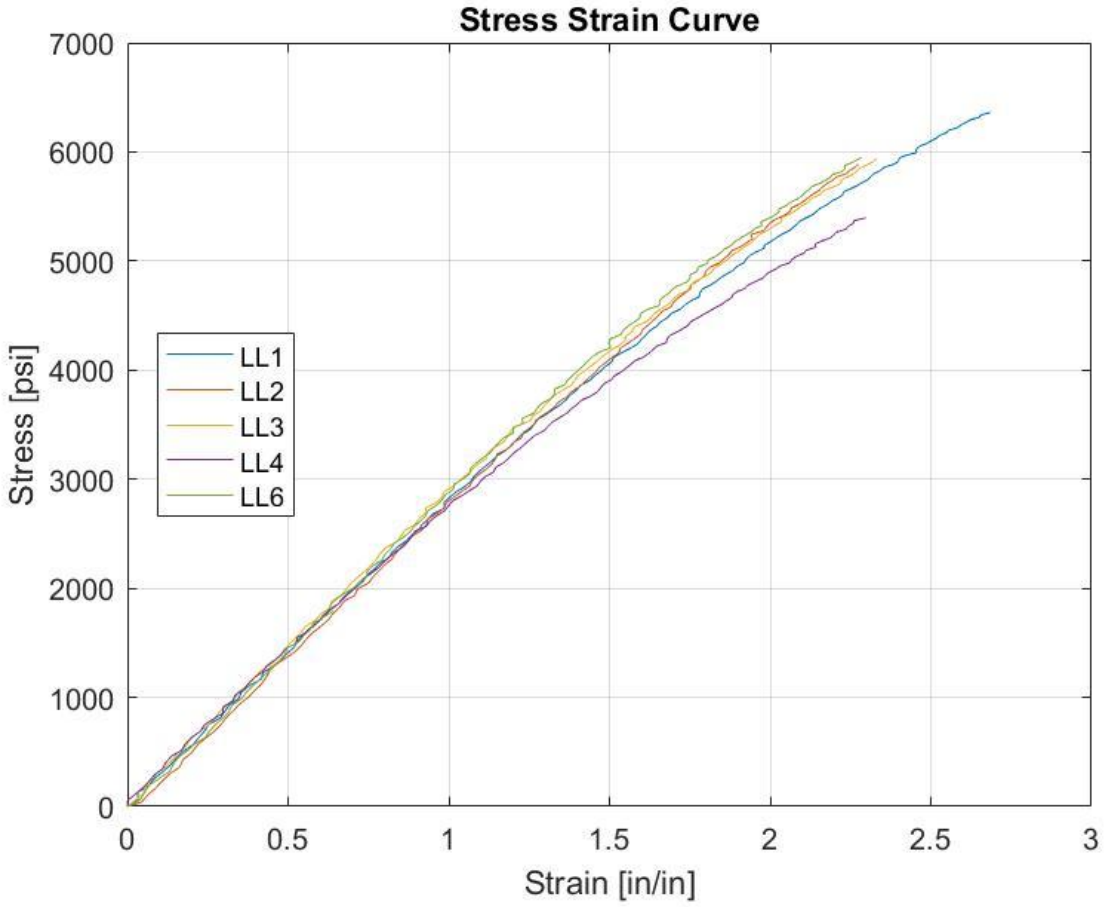

Figure E-15. Rectangular Bar Raster Thickness: 0.024 in. Stress-Strain Curve

Table E-16. Rectangular Bar Raster Thickness: 0.030 in. Raw Data

Rectangluar Bar | Raster Thickness: 0.030 in.		
Test Code	**Ultimate Tensile Stress [psi]**	**Average Ultimate Tensile Stress [psi]**
MM1	5250	5410
MM2	5440	
MM3	5170	**Standard Deviation [psi]**
MM4	5600	196
MM5	5590	

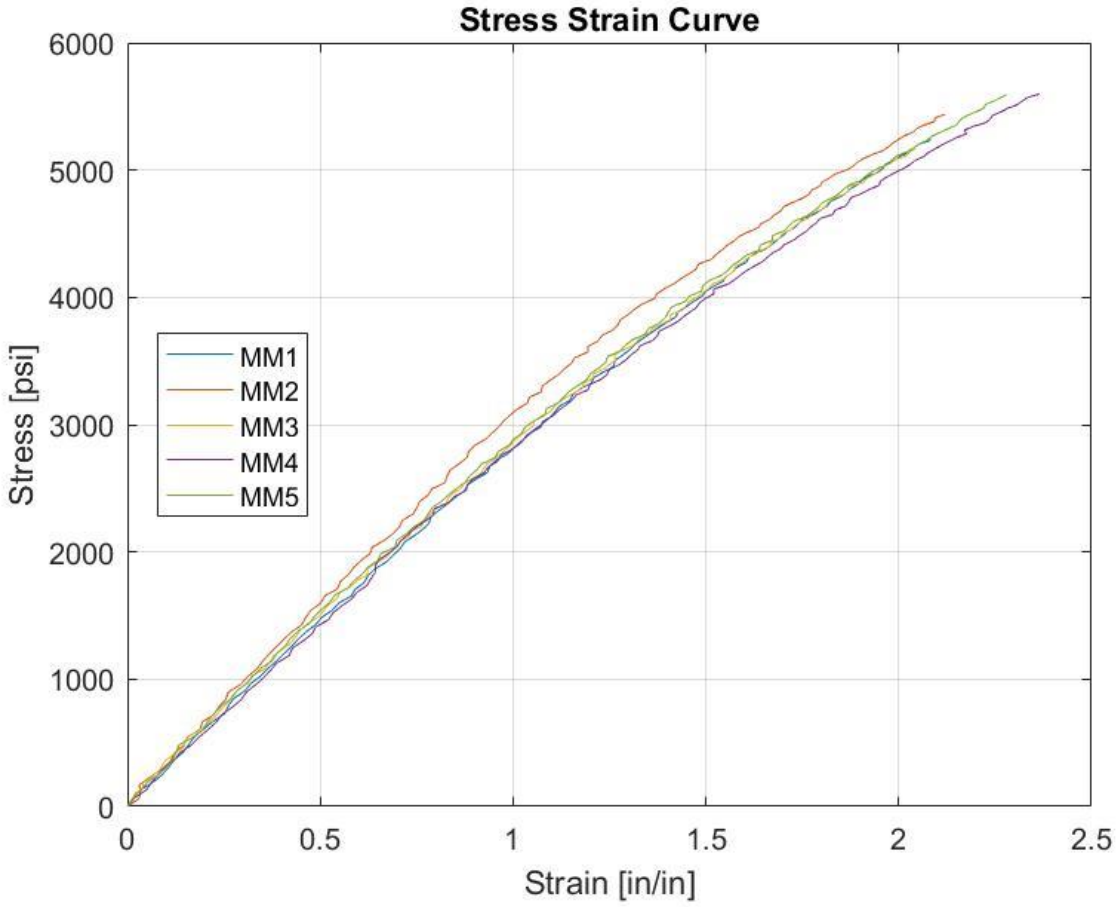

Figure E-16. Rectangular Bar Raster Thickness: 0.030 in. Stress-Strain Curve

Appendix F: Fatigue Raw Data

Table F-1. Tension-Tension Fatigue Tests Raw Data

Standard Tension-Tension Fatigue Raw Data			
Test Code	**Description**	**Stress [psi]**	**Cycles**
Q1	Tension-Tension Fatigue at 80% UTS	8400	330
Q2	Tension-Tension Fatigue at 80% UTS	8560	423
Q3	Tension-Tension Fatigue at 80% UTS	8590	401
R1	Tension-Tension Fatigue at 60% UTS	6080	1930
R2	Tension-Tension Fatigue at 60% UTS	6350	1990
R3	Tension-Tension Fatigue at 60% UTS	6220	1850
NN1	Tension-Tension Fatigue at 30% UTS	3030	24158
NN2	Tension-Tension Fatigue at 30% UTS	3030	27967
NN3	Tension-Tension Fatigue at 30% UTS	3030	22871
OO1	Tension-Tension Fatigue at 20% UTS	2020	92555
OO2	Tension-Tension Fatigue at 20% UTS	2020	99441
OO3	Tension-Tension Fatigue at 20% UTS	2020	83471
XX1	Tension-Tension Fatigue at 10% UTS	1010	1078363

Table F-2. Shorten Coupon Fatigue Life Verification with ASTM D638 Type I Geometry Raw Data

Shorten Coupon Verification Raw Data			
Test Code	**Description**	**Stress [psi]**	**Cycle**
N/A	Shorten Coupon Verification	3030	25828

Table F-3. Tension-Tension Build Parameter Variation Contour Thickness: 0.030 in. Raw Data

Contour Thickness: 0.030 in. Tension-Tension Fatigue Raw Data			
Test Code	**Description**	**Stress [psi]**	**Cycle**
Z1	Contour Thickness: 0.030 in. at 80% UTS	9600	843
Z2	Contour Thickness: 0.030 in. at 80% UTS	9456	832
Z3	Contour Thickness: 0.030 in. at 80% UTS	9536	749
BB1	Contour Thickness: 0.030 in. at 30% UTS	3030	30590
BB2	Contour Thickness: 0.030 in. at 30% UTS	3030	28961
BB3	Contour Thickness: 0.030 in. at 30% UTS	3030	26119
Y1.1	Contour Thickness: 0.030 in. at 20% UTS	2020	92077
Y2.1	Contour Thickness: 0.030 in. at 20% UTS	2020	79834
Y3.1	Contour Thickness: 0.030 in. at 20% UTS	2020	83703
AA1	Contour Thickness: 0.030 in. at 60% UTS	6445	2572
AA2	Contour Thickness: 0.030 in. at 60% UTS	6284	2481
AA3	Contour Thickness: 0.030 in. at 60% UTS	6128	3185

Table F-4 Tension-Tension Build Parameter Variation Raster Thickness: 0.030 in. Raw Data

Raster Thickness: 0.030 in. Tension-Tension Fatigue Raw Data			
Test Code	**Description**	**Stress [psi]**	**Cycle**
GG1	Raster Thickness: 0.030 in. at 30% UTS	3030	21381
GG2	Raster Thickness: 0.030 in. at 30% UTS	3030	21056
GG3	Raster Thickness: 0.030 in. at 30% UTS	3030	23123
HH1	Raster Thickness: 0.030 in. at 20% UTS	2020	73973
HH2	Raster Thickness: 0.030 in. at 20% UTS	2020	81929
HH3	Raster Thickness: 0.030 in. at 20% UTS	2020	98350

Appendix G: Example of Applying Research Learning to Optimized End-Use Part Manufacturing Based on Data Observation (StreamVane Manufacturing Best Practice)

StreamVane Manufacturing Best Practice

These guidelines were developed with the assumptions that the StreamVanes (SV) have an average vane thickness of 0.25 in. thickness, a constant chord, a leading edge, and a trailing edge. All recommendations are based on the data observation of the

1. The StreamVanes should be constructed with the following build parameters.

StreamVane Build Parameters	
Build Parameters	**Settings**
Contour Thickness	0.024 in.
Number of Contours	1 Contour
Raster Angle	45°/-45°
Raster Thickness	0.024 in.
Raster to Contour Air Gap	0.0 in.
Raster to Raster Air Gap	0.0 in.
Contour to Contour Air Gap	0.0 in.
Build Orientation	XYZ

a. Contour Thickness: 0.024 in.

The contour thickness should be set to 0.024 in. to maximize the mechanical properties, while allowing sufficient clearance for a raster fill. The 0.030 in. contour thickness would optimize the strength of the SV. However, the 0.030 in. contour thickness might not produce enough clearance for a raster fill at the trailing and

leading edge. The slightly smaller contour thickness will allow a greater portion of the leading/trailing edge to be filled with raster.

b. Number of Contours: 1

The number of contours should remain at one contour. Two contours may double the contour depth to a thickness where raster fill would not be used. This might be problematic around the joints because a 4-way joint will have a large void in the middle. That void may compromise the structural integrity of the StreamVane.

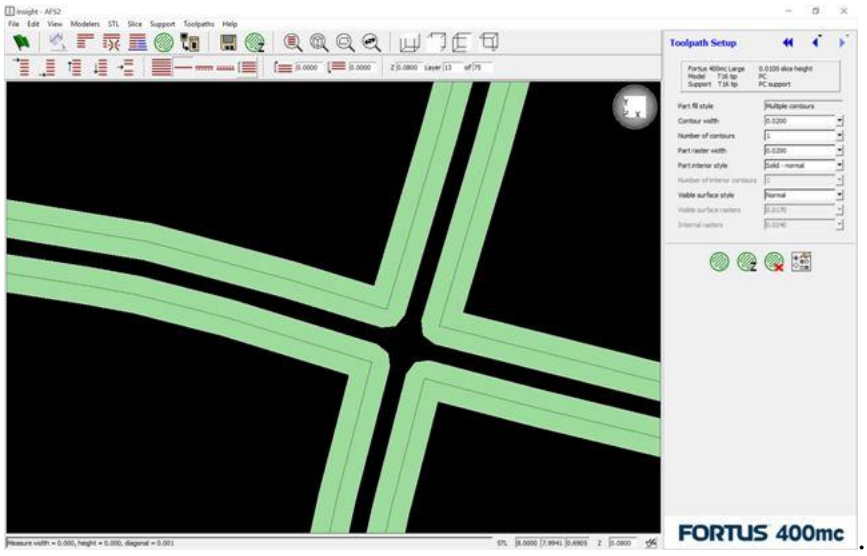

c. Raster Angle: 45º/-45º

The raster angle should remain at the default setting of 45º/-45º. The research data demonstrated the that the Raster Angle 30º/-60º produced the densest part, which correlated with the highest ultimate tensile strength. However, the void reduction through varying the raster angle is dependent on the geometry of the component. There is not a feasible way optimize the raster angle for the part geometry except for experimentally. Potentially, multiple 6 in. StreamVanes can be printed and weighed

to determine the optimized raster angle. However, the contour thickness and raster thickness would have to be scaled to match the full-size StreamVane. The effort to optimize the raster angle is not worth the strength gain at the current state.

d. Raster Thickness: 0.024 in.

The research data demonstrated that the coupon with the thickest raster have the lowest amount of void because it had the highest mass. However, the fatigue life decreases with a larger raster thickness. Additionally, the raster thickness needs to be less than the between contour thickness to support a raster fill. A part shall have raster fill to promote layer bonding and prevent delamination. A raster thickness of 0.024 in. is optimized for assumptions made in the beginning of the document.

e. Raster to Contour Air Gap: 0.00 in.

Based on the literature review and expertise from Stratasys, negative air gaps create a denser and stronger part. However, a negative air gap increases the chance that a nozzle will clog. A clogged nozzle may affect the quality of the print or cause the print to fail completely. The StreamVane should be manufactured using an air gap of 0.00 in to maximize the probability of a successful print. A failed print wastes significant resources. Therefore, build strategies should mitigate risks that are associated with failed prints.

f. Raster to Raster Air Gap: 0.00 in.

Based on the literature review and expertise from Stratasys, negative air gaps create a denser and stronger part. However, a negative air gap increases the chance that a

nozzle will clog. A clogged nozzle may affect the quality of the print or cause the print to fail completely. The StreamVane should be manufactured using an air gap of 0.00 in to maximize the probability of a successful print. A failed print wastes significant resources. Therefore, build strategies should mitigate risks that are associated with failed prints..

g. Contour to Contour Air Gap: 0.00 in.

Based on the literature review and expertise from Stratasys, negative air gaps create a denser and stronger part. However, a negative air gap increases the chance that a nozzle will clog. A clogged nozzle may affect the quality of the print or cause the print to fail completely. The StreamVane should be manufactured using an air gap of 0.00 in to maximize the probability of a successful print. A failed print wastes significant resources. Therefore, build strategies should mitigate risks that are associated with failed prints..

h. Build Orientation

The StreamVane shall be printed in XYZ Orientation (minimum z) to minimize the amount of support material needed. The support material affects the surface quality of the part. Additionally, the z-direction determines the build time of the part. A larger z-dimension will have a longer build time, which will significantly increase the price of the component.

2. The StreamVanes shall be constructed with the smallest layer height possible. (0.007 in. layer height for Fortus 900MC)

a. Minimum Layer Thickness

The minimum layer thickness will increase the resolution of the StreamVane. The smaller layer thickness will improve the surface finish, which is important for airfoils. Additionally, small layer thicknesses will minimized the stress concentration caused by layer stepping. The reduction in stress concentrations will improve the mechanical property of the StreamVane.

3. Any cantilever structures that have a thickness to height ratio of less than 0.0263 and a width to height ratio less than 0.1579 need to be redesigned so that the two ratios are larger than the two specified values. Another method to eliminate the cantilever is by encompassing the tall aspect ratio component with support material to change the thickness to height ratio and the width to height ratio.

    a. **Cantilever Structures**

    The research data suggested that if the ratios were not met, then the force of the nozzle motion would cause the structure to vibrate. The oscillating structure produced a part with a poor surface finish and some components completely failed.

Chapter 7 Reference

1. Sung-Hoon, A., Michael, M., Dan, O., Shad, R., and Paul, K. W. "Anisotropic material properties of fused deposition modeling ABS," *Rapid Prototyping Journal* Vol. 8, No. 4, 2002, pp. 248-257.
2. Gao, W., Zhang, Y., Ramanujan, D., Ramani, K., Chen, Y., Williams, C. B., Wang, C. C. L., Shin, Y. C., Zhang, S., and Zavattieri, P. D. "The status, challenges, and future of additive manufacturing in engineering," *Computer-Aided Design* Vol. 69, 2015, pp. 65-89.
3. Hossain, M. S., Ramos, J., Espalin, D., Perez, M., and Wicker, R. "Improving tensile mechanical properties of FDM-manufactured specimens via modifying build parameters," *International Solid Freeform Fabrication Symposium: An Additive Manufacturing Conference. Austin, TX*. Vol. 2013, 2013, pp. 380-392.
4. Bagsik, A., Schöppner, V., and Klemp, E. "FDM part quality manufactured with Ultem* 9085," *14th international scientific conference on polymeric materials*. Vol. 15, 2010, pp. 307-315.
5. Bagsik, A. S., V. "Mechanical Properties of Fused Deposition Modeling Parts Manufactured with ULTEM*9085," *ANTEC 2011*. 2011.
6. Lee, J., and Huang, A. "Fatigue analysis of FDM materials," *Rapid prototyping journal* Vol. 19, No. 4, 2013, pp. 291-299.
7. Spikowski, J. H., E.; Wang, S. "Fatigue Perfromance of Fused Deposition Modeling Style 3D Printed vs. Injection Molded ULTEM 9085," *Society of Plastics Engineers. (2015). ANTEC® 2015*. Orlando, Florida, USA, 2015.
8. Hoopes, K. M. "A new method for generating swirl inlet distortion for jet engine research." Virginia Tech, 2013.
9. redazione. "Keech Australia revolutionizes its design with 3D printing." Metalworking World Magazine, 2014.
10. "Standard Test Method for Tensile Properties of Plastics." ASTM International, 2014.
11. Durgun, I., and Ertan, R. "Experimental investigation of FDM process for improvement of mechanical properties and production cost," *Rapid Prototyping Journal* Vol. 20, No. 3, 2014, pp. 228-235.
12. Fischer, M., and Schöppner, V. "Fatigue Behavior of FDM Parts Manufactured with Ultem 9085," *JOM*, 2016, pp. 1-6.
13. "Standard Practice for Conditioning Plastics for Testing." ASTM International, 2013.
14. "Standard Test Method for Tensile Properties of Polymer Matrix Composite Materials." ASTM International, 2014.
15. Gillaugh, D., Copenhaver, W. W., Janczewski, T., Holycross, C., Sanders, D., and Nessler, C. "Aeromechanical Evaluation of an FDM Printed Thermoplastic StreamVane(TM)," *53rd AIAA/SAE/ASEE Joint Propulsion Conference*. American Institute of Aeronautics and Astronautics, 2017.
16. "Standard Test Method for Uniaxial Fatigue Properties of Plastics." ASTM International, 2017.
17. "Standard Terminology for Additive Manufacturing-Coordinate Systems and Test Methodologies." ASTM International, 2013.
18. Kay, R. "Effect of Raster Orientation on the Structural Properties of Components Fabricated by Fused Deposition Modeling." The Ohio State University, 2014.
19. Ning, F., Cong, W., Qiu, J., Wei, J., and Wang, S. "Additive manufacturing of carbon fiber reinforced thermoplastic composites using fused deposition modeling," *Composites Part B: Engineering* Vol. 80, 2015, pp. 369-378.